MASTERARBEIT | MASTER'S THESIS

Titel | Title

Investigating human TLX-LBD homodimerization and phenotypic consequences of TLX agonism in vitro employing a chemically diverse set of TLX modulators

verfasst von | submitted by

Isabelle Sophie Meijer BSc

angestrebter akademischer Grad | in partial fulfilment of the requirements for the degree of

Master of Science (MSc)

Wien | Vienna, 2024

Studienkennzahl lt. Studienblatt | Degree programme code as it appears on the student record sheet:	UA 066 606
Studienrichtung lt. Studienblatt | Degree programme as it appears on the student record sheet:	Masterstudium Drug Discovery and Development
Betreut von | Supervisor:	Dr. Daniel Merk

Acknowledgements

I would like to express my sincere gratitude to Prof. Dr Daniel Merk for providing me with the invaluable opportunity to be a part of his laboratory team at Ludwig Maximilian University of Munich during this summer. His guidance, unwavering dedication to his students, and his profound expertise have not only helped me deepen my understanding in the field, but also helped me to grow my academic confidence during my journey. His mentorship has left a lasting and inspiring impression on me.

Also, I extend my heartfelt thanks to Dr. Julian Marschner, my direct supervisor, for his trust and support throughout my master's internship. His openness to discussions and his willingness to explore ideas, combined with the time and effort he devoted, made him an exceptional mentor. Moreover, I deeply appreciate his keen eye and great attention to detail during the review and correction of my thesis, which substantially enhanced its quality.

I am deeply appreciative of Dr. Vasily Morozov and Úrsula López García for their expertise during the process of protein purification and the biochemical assays. Additionally, I want to thank Emily Hank and Tanja Stiller for providing the compounds used in this study and for their assistance during the experiments.

To all, I am profoundly grateful for the wonderful time we shared. The welcoming and supporting environment of this team has been truly special, leaving a great impact not only on my academic growth, but also my personal growth.

Statutory declaration

Hereby I declare that this master thesis was written by myself and that I did not use any other aids or references than those listed in chapter 9, none of which are unauthorized.

I assure that I have not previously submitted this thesis or its contents in any form for assessment as part of an examination in Austria or abroad.

All copies of this thesis submitted by myself (printed or electronic) are identical.

Date: …… Signature: ……

Outline

1. Zusammenfassung

Der Tailless homologe Rezeptor (TLX), ist ein orphan nukleärer Rezeptor, welcher eine Schlüsselrolle bei der Regulierung von Neurogenese, Zellproliferation und der Aufrechterhaltung neuronaler Stamm- und Vorläuferzellen spielt. Eine Dysregulation von TLX wurde mit Glioblastomen in Verbindung gebracht, bei denen eine Überexpression von TLX Tumorwachstum und -entwicklung fördert und in Tierversuchen die Überlebenszeit in Mäusen deutlich reduziert. Im Gegensatz dazu wurden niedrige Level von TLX mit kognitiven und psychiatrischen Störungen assoziiert. Trotz seiner Bedeutung sind die Mechanismen und die biologische Funktion von TLX nur unzureichend verstanden, und bislang wurden nur wenige TLX-Agonisten und inverse Agonisten beschrieben. Die Entwicklung potenter und spezifischer chemischer Wirkstoffe bietet nicht nur vielversprechendes therapeutisches Potential, sondern trägt auch dazu bei, das Verständnis der Rolle von TLX in Gesundheit und Krankheit zu erweitern.

In dieser Studie verwenden wir ein Set von 12 validierten TLX-Modulatoren, um die Auswirkungen auf TLX-Homodimerisierung sowie auf nachfolgende molekulare und phänotypische Effekte zu untersuchen. Dazu wird ein homogener Zeitaufgelöster FRET (HTRF) Versuch durchgeführt, um die Dynamik der TLX Homodimerisierung in einem zellfreien Kontext zu analysieren. Aufgereinigtes TLX-LBD wird, als FRET Donor Molekül verwendet, während das sGFP-TLX-LBD Fusionsprotein als FRET-Akzeptor dient. Die Dimerisierung wird sowohl unter apo Bedingungen als auch unter Anwesenheit der TLX-Liganden untersucht. Darüber hinaus untersuchen wir die nachgelagerten Effekte anhand von TLX-Modulation durch qPCR-Experimente. Veränderungen der mRNA-Expression von TLX und ausgewählten TLX-Zielgenen (PTEN, SIRT1 und TET3) werden in verschiedenen TLX exprimierenden Zelllinien, nämlich T98G Glioblastoma Zellen, retinale Pigmentepithel Zellen (ARPE19) und HEK293T Zellen, untersucht. Für die Phänotypisierung werden Zellwachstum und Viabilität in den Zelllinien ARPE19 und HEK293T orthogonal bewertet und mit der Lungenkrebs Zelllinie A549, die wenig bis kein TLX exprimiert, verglichen. Zusätzlich wird in T98G Zellen ein „Scratch-Wound“ Versuch durchgeführt, um das Migrationsverhalten der Zellen zu bewerten, wenn sie mit dem Set an TLX-Modulatoren behandelt werden.

Wir identifizierten Verbindung **7** als stabilisierend für die TLX-LBD-Homodimerisierung, und zwar als siebenfach im Vergleich zur apo Kontrolle ohne Liganden. Im Gegensatz dazu zeigten die übrigen Verbindungen keine signifikanten Effekte auf die Dimerisierung. Trotz der Stabilisierung wies Verbindung **7** in umfassenden in vitro Bewertungen keine herausragenden Unterschiede im Vergleich zu den anderen TLX-Modulatoren auf. Die Analyse der Zielgenexpression über mehrere Zelllinien hinweg offenbarte einen dosisabhängigen Effekt bei Behandlung der Zellen mit Verbindung **8** (1 und 10 µM), insbesondere auf die TLX-Expression selbst. Jedoch stimmten die Gesamtergebnisse nicht mit früher veröffentlichten Resultaten überein. Bei der Bewertung der Konfluenz und Zell Viabilität beobachteten wir einen deutlichen Unterschied zwischen den zwei Hauptchemotypen: Verbindungen **4** bis **8**, charakterisiert durch ein Chlorphenyl-(trifluoromethyl)phenyl)acetamid, und die Verbindungen **9** bis **12**, die ein Dimethoxy-

dihydro-isochinolin Gerüst aufweisen. Insgesamt waren die Verbindungen **4** bis **8** bis zu 10 µM gut verträglich, während die Verbindungen **9** bis **12** bereits bei deutlich niedrigeren Konzentrationen von 1 µM und darunter zytotoxische Effekte zeigten. Obwohl TLX-spezifische phänotypische Veränderungen in dieser Studie nicht bestätigt werden konnten, liefern diese Ergebnisse wertvolle Einblicke in die unterschiedlichen biologischen Effekte der beiden vertretenen Chemotypen. Diese Erkenntnisse könnten als Grundlage für zukünftige Struktur-/ Wirkung Beziehungsstudien (SAR) dienen und die zukünftig die gezielte Entwicklung von effektiven TLX-Modulatoren unterstützen.

2. Abstract

Tailless homologue receptor (TLX), is an orphan nuclear receptor and a key regulator during neurogenesis, proliferation, and maintenance of neuronal stem and progenitor cells. Dysregulation of TLX has been implicated in glioblastoma, where its overexpression drives tumor growth and progression, reducing survival in mouse models. Conversely, reduced TLX expression levels have been associated with behavioral changes as well as cognitive and psychiatric disorders. Despite its importance, the mechanisms and TLX's biological function remain poorly understood and to date only a few TLX modulators have been described. Developing potent and specific small molecules not only offers promising therapeutic potential but also advances our understanding of TLX's biological roles in health as well as disease.

In this study, we use a set of 12 validated TLX modulators to investigate the effects on TLX homodimerization and its downstream molecular and phenotypic effects. Therefore, a homogenous time-resolved FRET (HTRF) assay is performed to investigate TLX homodimerization dynamics in a cell-free context. Purified TLX-LBD is utilized as the FRET-donor while an sGFP-TLX-LBD fusion protein serves as the FRET-acceptor. Dimerization is analyzed under both apo conditions and in presence of the TLX modulators. Furthermore, we investigate downstream effects of TLX modulation by qPCR experiments. Changes in mRNA expression of TLX as well as selected TLX target genes (PTEN, SIRT1, and TET3) were assessed in multiple TLX expressing cell lines, namely T98G glioblastoma cells, retinal epithelial pigment (ARPE19) cells and HEK293T cells. For phenotypisation, cell confluence and viability are orthogonally assessed in ARPE19 and HEK293T cell lines compared to low to none TLX expressing lung cancer cell line A549. In addition, a scratch-wound assay is performed to assess cell migration in T98G upon treatment with the set of TLX modulators.

Here, we identified compound **7** to stabilize TLX-LBD homodimer formation by seven-fold compared to the apo control lacking ligands. In comparison, the remaining compounds exhibited no significant effects on dimerization. However, compound **7** displayed no unique behavior during broader *in vitro* assessment compared to other TLX modulators. Target gene expression analysis across multiple cell lines revealed a dose-dependent effect upon treatment with compound **8** (1 and 10 µM), particularly on TLX expression itself. However, the overall results did not align with previously published results. When assessing confluence and cell viability, we observed a distinct difference between the two main chemotypes: compounds **4** to **8**, characterized by a chlorophenyl-(trifluoromethyl) phenyl) acetamide, and the compounds **9** to **12**, which feature a dimethoxy-dihydro isoquinoline core. Overall, compounds **4** to **8** were well tolerated up to 10 µM, whereas compounds **9** to **12** exhibited cytotoxic effects at much lower concentrations as of 1 µM and below. While TLX specific phenotypic changes could not be confirmed in this study, these findings provided valuable insights into the differential biological effects of the two chemotypes. Such insights could inform further structure-activity relationship (SAR) studies and guide future efforts in the development of TLX modulators.

3. Introduction

3.1. Nuclear receptors

Confirmed by the human genome project the superfamily of nuclear receptors (NRs) consists of 48 members of evolutionary related, ligand-activated transcription factors (***Table 1***) involved in cellular homeostasis, differentiation and development [1, 2]. By binding to their respective DNA response elements, NRs can either activate or repress target gene expression, oftentimes acting as key regulators of metabolism, proliferation, or cell fate [3, 4]. In the late 1960s, researchers speculated about the presence of a specific receptor capable of binding estrogen and regulating sex hormones in women [5]. Over a decade later, the first NR clones of the glucocorticoid receptor (GR) and the estrogen receptor (ER) were generated. The full-length amino acid sequences provided first insights into the structure of nuclear receptors, laying the foundation for the discovery of additional NRs [1, 6].

The identification of NR sequences later shifted towards *in silico* methods due to the availability of large cDNA datasets and advanced bioinformatic tools [1]. These advancements spearheaded breakthroughs in pharmaceutical sciences by shedding light on multiple drugs that previously were found to be biologically active but lacked known targets. For example, derivatives of thiazolidinediones, antidiabetic agents that increase insulin sensitivity and promote adipocyte differentiation, were identified as selective and potent agonists of the peroxisome proliferator-activated receptor gamma (PPARγ) [7]. Since then, endogenous as well as synthetic ligands have been identified for many NR family members. However, some remain orphan receptors, as their endogenous ligands have not yet been identified.

Beside G-protein coupled receptors, ion channels and kinases, nuclear receptors belong to the small group of four major drug target families. As of 2017, 16% of FDA-approved drugs targeted NRs, generating billions of dollars in revenue annually [8, 9]. As transcription factors, NRs occupy a crucial position at the lower end of many cellular signaling pathways. Therefore, targeting NRs directly, increases specificity while reducing side effects [10]. Deciphering the structure, target genes, and their disease involvement may pave the way for the discovery of novel ligands, particularly for orphan receptors such as the tailless homologue receptor, TLX.

3.1.1. Classification of nuclear receptors

In general, the 48 members of the NR superfamily can be divided into seven subgroups (NR0 – NR6) based on shared sequence similarities, as listed in ***Table 1*** [11]. In addition to these evolutionary related subgroups, NRs can also be categorized based on their binding partner or ligands: classical retinoid X receptor (RXR) heterodimer receptors, steroid receptors, xenobiotic binding receptors, or orphan receptors [1].

First, NRs that form classical RXR heterodimers include the thyroid hormone receptor (TR), retinoic acid receptor (RAR), PPAR, liver X receptor (LXR), farnesoid X receptor (FXR) and the vitamin D receptor (VDR). These receptors typically share a larger ligand-binding pocket (LBP) and act as metabolic sensors by binding to molecules such as fatty acids, vitamins, cholesterol, oxysterols, bile acid or retinoic acids [1]. For example, PPARα, β/δ and γ are crucial regulators of energy metabolism by promoting fatty acid oxidation, fatty acid storage, and regulating adipocyte differentiation or glucose metabolism [12]. In addition to the classical RXR heterodimers, NRs also form homodimers or can act as monomers e.g., liver receptor homologous protein 1 (LRH-1), NGF-induced factor B (Nur77/NGFI-B) or steroidogenic factor 1 (SF-1) [13,14].

Second, classical steroid receptors include ER and estrogen related receptors (ERR) as well as GR, mineralocorticoid receptor (MR), progesterone receptor (PR) and the androgen receptor (AR) of the NR3 subgroup [1]. These receptors bind to adrenal and sex steroids and act as key regulators of numerous biological functions [3].

Third, pregnane X receptor (PXR) and constitutive androstane receptor (CAR) of the NR1I subgroup belong to xenobiotic binding receptors. By sensing harmful metabolic byproducts or environmental toxins, they induce biological functions that help eliminating them [15].

Lastly, for a large group of orphan NRs, no ligands have been identified so far. For the so called 'adopted' orphan receptors, endogenous ligands have only recently been described [16, 17]. For instance, the retinoic acid receptor related orphan receptor (ROR) can be considered an adopted receptor, as endogenous as well as synthetic ligands have been reported binding to ROR with great affinity [18, 19, 20]. More recently discovered NR-like receptors lack a classical DNA-binding domain (DBD) and include only two receptors: DSS-AHC critical region on the chromosome gene 1 (DAX1) and the short heterodimeric partner (SHP) [1].

Table 1: *Nuclear receptor superfamily. Adapted from Germain et al. [11] & Gronemeyer at al. [21]*

Name	Abbreviation	Nomenclature	Exemplary ligands
Thyroid hormone receptor	TRα TRβ	NR1A1 NR1A2	Thyroid hormone
Retinoic acid receptor	RARα - γ	NR1B1 – B3	Retinoic acid
Peroxisome proliferator-activated receptor	PPARα - γ	NR1C1 – C3	Fatty acids, leukotriene B4, fibrates, prostaglandin J2
Reverse erbA	Rev-erbα Rev-erbβ	NR1D1 NR1D1	Orphan receptor
RAR- related orphan receptor	RORα - γ	NR1F1 - 3	Cholesterol, cholesteryl sulphate, retinoic acid
Liver X receptor	LXRα LXRβ	NR1H3 NR1H2	Oxysterols, T0901317, GW3965
Farnesoid X receptor	FXRα FXRβ	NR1H4 NR1H5	Bile acids, fexaramine lanosterol
Vitamin D receptor	VDR	NR1I1	1, 25-dihydroxy vitamin D_3, litocholic acid

Pregnane X receptor	PXR	NR1I2	Pregnenolone 16α-carbonitrile (PCN), xenobiotics
Constitutive androstane receptor	CAR	NR1I3	Phenobarbital, xenobiotics
Human nuclear factor 4	HNF4α HNF4γ	NR2A1 NR2A2	Orphan receptor
Retinoid X receptor	RXRα - γ	NR2B1 – B3	Retinoic acid
Testis receptor	TR2 TR4	NR2C1 NR2C2	Orphan receptor
Tailless	TLX	NR2E2	Orphan receptor
Photoreceptor-specific NR	PNR	NR2E3	Orphan receptor
Chicken ovalbumin upstream promoter transcription factor	COUP-TF I COUP-TF II	NR2F1 NR2F2	Orphan receptor
ErbA2-related gene 2	EAR2	NR2F6	Orphan receptor
Estrogen receptor	ERα ERβ	NR3A1 NR3A2	Estradiol-17β, tamoxifen, raloxifene
Estrogen receptor-related receptor	ERRα ERRβ ERRγ	NR3B1 NR3B2 NR3B3	Orphan receptor Diethylstilbestrol (DES), 4-OH tamoxifen
Glucocorticoid receptor	GR	NR3C1	Cortisol, dexamethasone, RU486
Mineralocorticoid receptor	MR	NR3C2	Aldosterone, spirolactone
Progesterone receptor	PR	NR3C3	Progesterone, medroxyprogesterone acetate, RU486
Androgen receptor	AR	NR3C4	Testosterone, flutamide
NGF-induced factor B	Nur77	NR4A1	Orphan receptor
Nuclear receptor related 1	NURR1	NR4A2	Orphan receptor
Neuron-derived orphan receptor 1	NOR1	NR4A3	Orphan receptor
Steroidogenic factor 1	SF1	NR5A1	Orphan receptor
Liver receptor homologous protein 1	LRH1	NR5A2	Orphan receptor
Germ cell nuclear factor	GCNF	NR6A1	Orphan receptor
DSS-AHC critical region on the chromosome, gene 1	DAX1	NR0B1	Orphan receptor
Short heterodimeric partner	SHP	NR0B2	Orphan receptor

3.1.2. Structure

Based on sequence similarities and function, nuclear receptors share six protein regions (regions A to F). Among NRs, the DBD (region D), is highly conserved whereas the ligand-binding domain (LBD, region E) is only moderately conserved. The N-terminal A/B region is less conserved and not present in all NRs (e.g., HNF4γ or SHP). The hinge region D connects to the C-terminal region (E) as shown in ***Figure 1A and B***.

The isoform-specific N-terminal region A/B contains the activation function-1 (AF-1) domain, which is responsible for ligand independent, constitutive activation of the receptor. Within the NR superfamily, this highly variable region differs in length as well as sequence and shows less evolutionary conservation compared to other regions [22]. Furthermore, the generation of mRNA splice variants by alternative splicing or the use of alternative promoters add to the protein diversity of NRs [22, 23]. For example, PR α and

β differ in length, as PRβ's N-terminal region contains an additional AF-3 domain, which makes it transcriptionally more active over PRα [24].

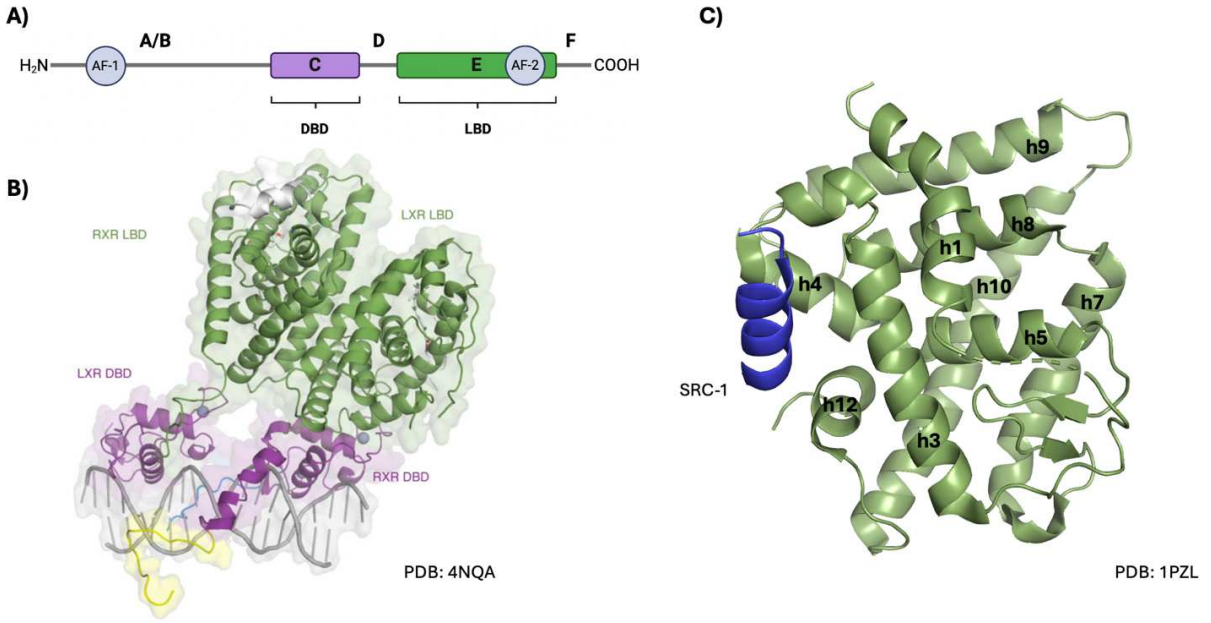

Figure 1:*Structural overview of nuclear receptors.* ***A****) Schematic depiction of the six NR regions from N' to C' terminus. Activation function 1 (AF-1) and 2 (AF-2) are highlighted in grey. DNA binding domain (DBD), region C is depicted in purple and the ligand binding domain (LBD), region E is shown in green. This image was created using BioRender.com.* ***B****) Representative heterodimer structure of LXR and RXR (PBD: 4NQA) taken from Weikum et al. [13]. According to the color scheme from (A) the LBD is shown in green and the DBD in purple. The N' terminal A/B region is highlighted in light blue and the hinge region in yellow.* ***C****) Representative depiction of an LBD (green) bound to a co-regulator (steroid receptor co-activator 1, SRC-1) highlighted in blue (PDB: 1PZL). Alpha helices are numbered from N' terminal (h1) to C' terminal (h12). Image was created in PyMol Molecular graphics system Version 2.5.8.*

In RARs, the A/B region contains phosphorylation sites that can be targeted by kinases for posttranslational modifications. For example, phosphorylation can reduce the transcriptional activity of PPARγ. Notably, the A/B region is involved in co-regulator interactions, binding with other transcription factors, or in some cases, it interacts with the C-terminus of the receptor itself.

Structural analysis demonstrated that region C, containing the DBD, consists of a common core of 66 amino acid residues with two zinc finger (ZF) motifs that bind to a DNA hormone response element (HRE) comprised of a six-base-pair repeat [11]. Each zinc finger consists of four cysteine residues coordinated with a zinc ion. Amino acid residues of helix 1 (h1) within the 'P box' of the first ZF specifically bind to the DNA response element, and h1 also binds the major groove of the DNA. The second ZF motive, within the 'D box', found in helix 2 (h2), allows homo- or heterodimerization of the nuclear receptor. A C-terminal extension of the DBD either supports dimerization by enabling additional protein-protein interactions or stabilizes binding to the HRE by engaging with the minor groove of the DNA [25].

The DBD and the LBD are linked by a hinge region (D), which, like the N-terminal domain, is weakly conserved and functions mainly as a linker, allowing flexible rotation of the DBD. In many NRs, this

region also harbors the nuclear localization signal. Here, post-translational modifications can affect co-regulator interactions and, consequently, the function of the NR. For example, the hinge region of ER contains acetylation, sumoylation, and ubiquitination sites that are involved in co-regulator recruitment or regulating its degradation, thereby its life-span [26].

However, the most relevant protein region for drug discovery and development is the C-terminal LBD. It is responsible not only for ligand binding but also for NR dimerization and contains the ligand-dependent activation function-2 (AF-2), a key regulatory element that enables co-regulator interactions [11]. Through crystal structures of liganded NRs, a common structure of the LBP was elucidated. Overall, the LBD is composed of three anti-parallel layers of 12 α-helices (h1-12) and a β-turn (s1-2), forming an 'α-helical sandwich'. The first layer is comprised of h1-h3, followed by the second, central layer of h4 and h5, the β-turn, and h8 and h9. The third layer contains h6, h7 and h10. Superpositioning of crystal structures showed that structural variability is highest at the base layer of the LBD, where the LBP is located. The pocket is mainly covered by hydrophobic residues, and only a few polar residues engage in hydrogen bonds critical for target-ligand interaction and positioning withing the pocket. Described as 'mouse-trap-model', agonist binding to the LBP induces conformational changes such that h12 covers the pocket [27]. Together with h3 and h4, it forms the AF-2 surface, enabling co-activators to bind via their nuclear receptor binding signature motive. Due to an alternative positioning of h12 in a ligand-free apo-state or upon antagonist binding, co-repressors are recruited, leading to transcriptional repression. The C-terminal region F is not present in all NRs and its function still needs to be fully elucidated [11, 13, 25,].

3.1.3. Molecular interactions of nuclear receptors with DNA and NR mechanism of action

Nuclear receptors interact with their respective DNA hormone response elements (HREs) via the DBD in different ways, which can be categorized into four types. Type 1 receptors, steroid receptors, are bound to chaperones within the cytoplasm. Upon ligand binding, the receptor dissociates from the complex and translocates into the nucleus, where it binds to its respective response element as a homodimer. The HRE consists of a palindromic repeat of two inverted consensus half-sites, 5' AGGACA 3', linked by a short sequence, typically 3 base pairs long [13, 22, 28, 29]. Types 2 to 4, the non-steroid receptors, are present in the nucleus and usually transition from a repressed state into an active state upon ligand binding. Type 2 receptors form heterodimers with RXR and are constitutively bound to their respective HRE in complex with co-repressors. Their HRE sequence consists of two direct repeats, palindromes or inverted palindromes of 5' AGGTCA 3', linked by a variable spacer of 1 to 5 base pairs. Upon ligand binding, co-repressors are released while co-activators are recruited, inducing target gene expression. Like type 2 receptors, type 3 receptors reside in the nucleus bound to their HRE in a repressive state, but as homodimers. Ligand activation leads to an exchange of co-factors and activation of gene expression. Type 4, monomeric NRs, bind to HRE half sites, 5' AGGTCA 3', extended with a 5' prime sequence of 3 base pairs, either 5'-AAA-3' or 5'-ACT-3' [13, 28]

3.1.4. Molecular interactions between nuclear receptors

In their unbound state, NRs typically exist as monomers in solution. However, upon binding to their respective HREs most NRs form homo- or heterodimers [13]. This cooperative binding increases their affinity for DNA and facilitates the formation of multimeric complexes. Dimerization not only stabilizes DNA binding but also enhances specificity by enabling the recognition of two adjacent hexanucleotide sequences connected by a defined spacer. Furthermore, RXR heterodimers can recognize two distinct sequences, allowing for a broader range of potential genes depending on their binding partner [30].

Notably, only the DBD directly interacts with the DNA. However, dimerization can occur via the LBD as well as the DBD. Surface residues of the DBD are involved in weak interactions with DBD of the dimerization partners. The most common dimerization interfaces within the LBD involve helices 7 and 9-11, as well as loops 8 and 9. These structural features enable the formation of stable dimer complexes [13, 30].

3.1.5. Molecular interactions of nuclear receptors and their respective ligands

To date, synthetic and endogenous ligands have been identified for approximately half of the NRs. Endogenous ligands typically include hydrophobic molecules such as steroid hormones, vitamins or fatty acids. The specificity and selection of ligands are determined by the size and shape of the LBP, which varies between different NRs and within their subgroups [31, 32]. For example, the LBPs of steroid receptors generally measures between 400 and 500 $Å^3$, whereas PPARs possesses a considerably larger LBP up to 1300 $Å^3$, more than double the size [33]. Despite the lipophilic nature of the LBP, a network of hydrogen bonds ensures the correct positioning of the ligand within the pocket. For instance, the LBP of steroid receptors features an arginine residue on helix 5 and a glutamine residue on helix 3, which stabilize ring A of the steroid backbone. However, the positioning of rings C and D varies according to the LBP of each specific NR [31, 32].

3.1.6. Molecular interactions of nuclear receptors and co-regulators

The transcription of genes is a highly intricate process involving numerous factors beyond the binding of NRs to DNA. In general, DNA is organized into chromatin, which can be classified as either loosely packed euchromatin or tightly packed heterochromatin. Euchromatin regions are considered transcriptionally active because their open structure allows transcription factors and the transcriptional machinery to access DNA. In contrast, condensed heterochromatin generally restricts gene transcription [34]. Within open euchromatin regions, NRs initially bind to their specific HREs. Ligand binding activates the

receptor, triggering conformational changes that stabilize the LBD and facilitate their functional activation. In these open euchromatin regions, nuclear receptors bind to their DNA response element and are activated upon ligand binding, inducing conformational changes that stabilize the LBD. Subsequently, co-regulators are recruited, which play crucial roles in chromatin remodeling, interaction with additional TFs, and recruitment of the transcriptional machinery necessary for initiating gene expression [11, 35].

Co-regulators are categorized as activators (CoA) and repressors (CoR), which either enhance or inhibit the expression of target genes. To date, more than 200 co-regulators have been identified [36]. In 1995, the first co-regulator, steroid receptor co-activator 1 (SRC-1), a member of the p160 protein family, was discovered to bind the human PR [36, 37]. SRC-1 exemplifies common features of co-activators: it binds via multiple short hydrophobic α-helices to the ligand-bound receptor, exhibits histone acetyltransferase (HAT) activity, and recruits secondary co-regulatory factors to facilitate heterochromatin decondensation and gene transcription [1].

The AF-1 and AF-2 regions located in the N-terminal domain and the LBD of NRs mediate the interaction with co-regulators. While the unstructured nature of the A/B region in the N-terminal domain limits our understanding of AF-1 interactions, co-crystallization studies have provided substantial insights into AF-2 interactions [13]. CoAs typically bind via a short, conserved 'LXXLL' motif (where X represents any amino acid) to hydrophobic residues on the AF-2 surface. This interaction is stabilized by a charge-clamp mechanism involving a lysine residue on h3 and a glutamate residue on h12. In contrast, CoRs, which contain conserved motifs like (L/I)XX(I/V)I or LXXX(I/L)XXX(I/L), termed the 'CoRNR box', also bind to the AF-2 but lack stabilization by the helix 12 [11, 38]. Structural analysis of antagonist-bound receptors revealed that h12 rotates to cover the CoA binding surface, thus promoting a repressed state. Also in the absence of a ligand, CoRs typically bind to NRs, such as TR or RAR, to maintain a constitutive repressive transcriptional state [22, 39]. Co-repressors of unliganded NRs include for example silencing mediator for RAR and TR (SMRT) or NR corepressor (N-CoR) whereas repressors of liganded NRs comprise for example receptor interacting protein 140 (RIP140) or ligand-dependent co-repressor (LCoR) [40]. Upon ligand binding, conformational changes occur leading to the dissociation of CoRs and the recruitment of CoAs, facilitating the activation of gene transcription [22, 41]. In general, HATs promote a euchromatin state by acetylating lysine residues of histones, loosening chromatin and allowing access to additional transcription factors as well as the transcriptional machinery. In contrast, chromatin remodelers like histone deacetylases (HDAC) remove acetyl groups, tightening chromatin structure and rendering DNA inaccessible to transcription. Histone methyl transferases (HMTs) and histone demethylases (HDMs) regulate the methylation state of specific lysine or arginine residues. The impact of methylation on transcriptional activity depends on the location of the modified residue rather than the methylation itself [21].

3.2. TLX – tailless homolog receptor

In the mid-1990s, the tailless homologue receptor (TLX, NR2E1) was identified as a homologue of the *drosophila melanogaster* tailless (*tll*) gene. TLX is highly conserved across invertebrates and vertebrates and plays a crucial role in cell fate determination in the brain and retina during development and adulthood [42]. The overall amino acid sequence similarity between human and fly TLX is approximately 60%. Notably, greater similarity is observed in the DBD, with an 81%match, compared to the LBD, which shows 41% similarity. Among mammals, the sequence identity of TLX is 99%, while it is slightly lower for birds (97%) and fish (91%) [43, 44, 45].

TLX belongs to the NR subfamily 2 (NR2), which also includes members such as the hepatocyte nuclear factor 4 (HNF4), RXR, testicular receptor (TR), chicken ovalbumin upstream promoter transcription factor transcription factor (COUP-TF), photoreceptor cell specific nuclear receptor (PNR) and V-ErbA-Related protein 2 (EAR2) receptors. As summarized in ***Table 1***, most of the NR2 subfamily members are orphan receptors or have only recently been classified as adopted receptors [11].

3.2.1. Isoforms

Two human TLX transcript variants, or isoforms, have been identified. Isoform A (hTLX, accession number NP_001273031.1) consists of 422 amino acid residues and Isoform B (hTLX, accession number NP_003260.1) is composed of 385 amino acid residues, encoded by nine exons. Both isoforms share identical DBDs and LBDs but differ in their N-terminal A/B regions. This variation arises due to alternative splicing of the N-terminal exon 1, which results in isoform B being 37 amino acid residues shorter than isoform A [46, 47]. Currently, there are no reported functional differences between both isoforms beyond their distinct N-terminal lengths. Research has primarily focused on the shorter isoform B, largely because its primary sequence exhibits a higher degree of similarity to TLX orthologs [48].

3.2.2. Structure

The TLX receptor shares common features among NRs as illustrated in ***Figure 2A***. Analysis of the human TLX isoform B (accession number NP_003260.1) identified the DBD, spanning from residue 8 to 99, which includes two conserved zinc finger motifs. The LBD (residues 154-369) follows the hinge region and contains the AF-2 (residues 341-385) essential for ligand-dependent activation. Both isoforms lack a substantial A/B region, including the ligand-independent AF-1 domain [46]. As a type 4 NR TLX is considered to bind DNA as a monomer to the 5'-AAGTCA-3' half-site [49].

However, Zhi et al. revealed that TLX can homodimerize via interaction sites located in h10 of the LBD. A crystal structure of apo TLX-LBD (residue 182 to 385), tagged to a maltose-binding protein (MBP),

was resolved at 3.5 Å (PDB: 4XAJ, R: 0.273, R_{free}: 0.314). ***Figures 2B*** and ***2C*** show the dimer binding to the CoR atrophin 1 via helices 3 and 12. Key atrophin 1 residues (A1819, L1820, L1823, and Y1826), form the common CoR 'ALXXLXXY' motif, interacting with TLX residues T373 and L376 in helix 3 as well as E187, A190, F194 and F363 in h12. These interactions are primarily hydrophobic, complemented by a hydrogen bond between atrophin residues A1819/L1820 and TLX's E187 [45]. As h12 covers the LBD region that typically binds CoAs, this conformation forms an autorepressed pocket, facilitating the interaction with CoRs such as atrophin 1, HDACs, or LSD-, thereby promoting the repressive state of TLX [45, 48].

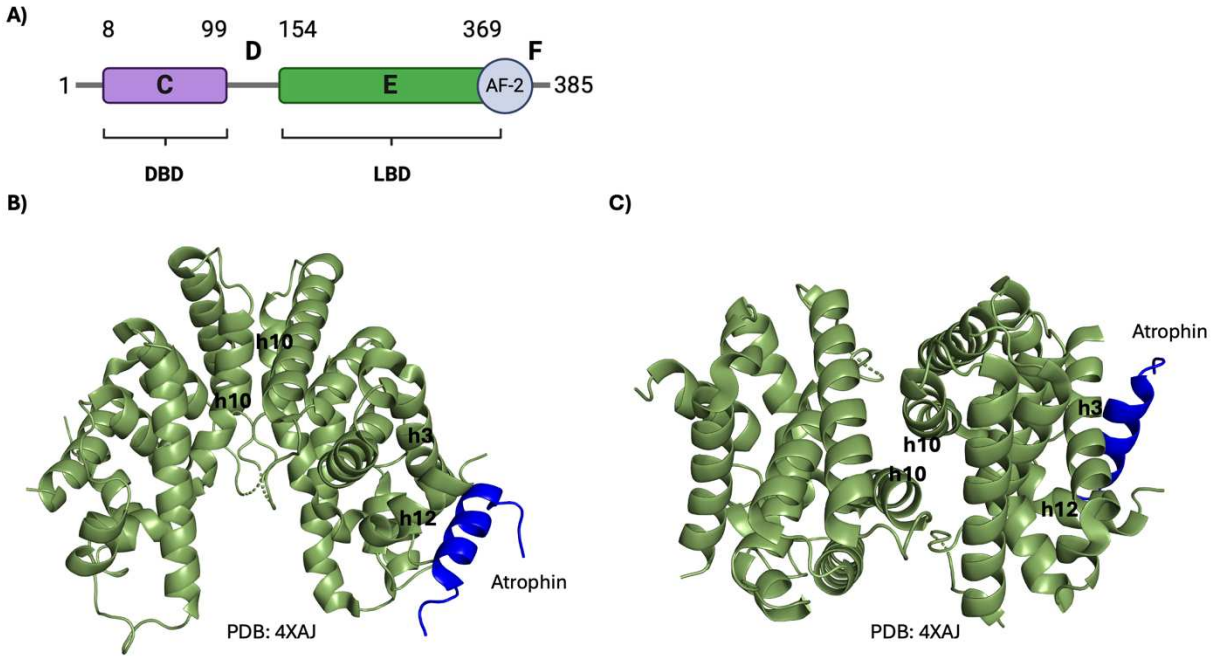

Figure 2: *Structural organization of hTLX.* ***A****) Schematic overview of hTLX isoform B (NP_003260.1) regions. Region C spanning from amino acid residue 8 to 99 in purple represents the DNA binding domain (DBD). In green, region E depicts the ligand binding domain (LBD) from residue 154 to 269 as of NP_003260. This image was created using BioRender.com.* ***B****) Frontal view of cartoon depiction of a hTLX-LBD dimer (green) co-crystallized with atrophin 1 (blue)* ***C****) Top view on the hTLX-LBD dimer. Dimerization helices h10 are labeled each as well as h3 and h12 involved in atrophin binding. Both images (B and C) were created using PyMol Molecular graphics system Version 2.5.8. (PDB: 4XAJ)*

3.2.3. TLX expression and biological function

During embryogenesis, TLX plays a pivotal role in the development and maintenance of neural progenitor cells (NPCs) within the central nervous system (CNS) [48]. Early in development, TLX is highly expressed in the ventricular zone (VZ), the primary proliferative zone of NPCs in the CNS [50]. As embryogenesis progresses, additional proliferative zones, such as the intermediate zone (IZ) and the subventricular zone (SVZ), emerge above the VZ, where TLX continues to regulate cell division and maintain neural stem cell (NSC) populations [51]. TLX knock out (KO) studies in mice revealed that the absence of TLX leads to a reduction of NPCs in the cortex's IZ, resulting in smaller posterior brain hemispheres and

underdeveloped structures in the limbic system and rhinencephalon. These changes are associated with impaired embryonic brain growth, although prenatal viability remains unaffected [50].

In the adult brain TLX is predominantly expressed in the nuclei of NSCs and NPCs , where it plays a critical role in promoting proliferation of undifferentiated stem cells [48]. Stem cells are defined as undifferentiated cells able to self-renew and proliferate. Their fate depends on their anatomical location as well as the surrounding microenvironment, known as the stem cell niche [52]. NSCs can differentiate into neurons, motor neurons, or glial cells [53]. During adult neurogenesis, TLX is expressed in germinal centers located in the subventricular zone (SVZ) of the lateral ventricles and the subgranular layer of the hippocampal dentate gyrus [52, 54, 51]. Loss of TLX in adult mice showed a change in behavior as they were hyperexcitable, aggressive and female mice showed signs of maternal neglected. In addition, mutant mice failed during water maze tests revealing diminished spatial learning abilities [55] The observed behavioral changes correlate with the structural and functional impairments in the limbic system, which is associated with memory, spatial orientation, empathy, perception and behavior [55, 56]

Beyond the brain, TLX is expressed during early development in the neural retina, the optic stalk, and adjacent areas of the diencephalon. In later embryogenesis, it is also found in the ganglion and retina [49,]. TLX KO mice exhibit progressive retinal degeneration, accompanied with a reduced thickness of the optic nerve resulting in visual impairments and, eventually, blindness. TLX in retinal progenitor cells (RPCs) fulfills similar functions to its role in the brain, regulating cell proliferation and differentiation [57].

3.2.4. Transcriptional repression by TLX

Although TLX can function as both a transcriptional repressor and activator, it primarily acts as a transcriptional repressor. Its activating function is thought to arise indirectly, often by suppressing a constitutively repressive state [58]. Like other orphan receptors, TLX binds to its DNA response element 5'-AAGTCA-3', located in the promoter region upstream of the TATA box [59]. To date, only a few TLX target genes have been identified.

In multiple model organisms TLX has been found to repress the expression of the transcription factor paired box 2 (PAX2), which plays an important role during embryogenesis including retinal development and vision [49, 60]. Gene profiling analysis showed significant downregulation of Wnt7α expression in TLX KO samples. TLX activates Wnt7α expression by binding to two adjacent HREs 5'-AAGTCA-3' within the Wnt7α promoter, separated by six base pairs. The Wnt/β-catenin signaling pathway is considered an essential regulatory element stimulating proliferation and the expansion of NSCs and NPCs [54, 61]. In human glioblastoma stem cells, ten eleven translocation 3 (TET3), a DNA hydrolase, has been identified as a target gene of TLX. In TLX knockdown experiments the downregulation of TLX inhibits tumor proliferation and prolonged survival in mice [62]. Lysin specific demethylase 1 (LSD1) and histone deacetylase 5 (HDAC5) are transcriptional co-regulators that modulate chromatin structure by removing methyl

groups and acetyl moieties from histones, respectively [63, 64]. Chromatin immunoprecipitation (ChIP) analysis demonstrated that these chromatin modifying enzymes are recruited to TLX-bound promoter regions of cyclin dependent kinase inhibitor 1 (CDKN1A/p21) and phosphatase and tensin homolog (PTEN). Downregulation of LSD1 and HDAC5 leads to a decrease of NSC proliferation [65, 66]. Tumor suppressor gene PTEN negatively regulates NSCs proliferation by controlling the cell cycle [67, 68]. Similar eye phenotypes and vision impairments were observed in sirtuin 1 (SIRT1) KO mice, resembling those seen in TLX KO models [49, 69]. It is suggested that TLX binds to a TLX-activating element (5'-TCACGTGACGG-3') within the SIRT1 promoter to induce expression. Since this binding sequence differs from known HREs, it is proposed that TLX may bind indirectly through additional co-factors to activate SIRT1 expression. The study concludes that TLX's effect (activating or repressing) depends on specific DNA binding sites [69]. In NPCs, under hypoxic conditions, TLX regulates proliferation via the octamer-binding transcription factor 3/4 (Oct-3/4) promoter, maintaining a proliferative state. TLX knockdown in these conditions results in differentiation and loss of pluripotency [70]. Furthermore, TLX's function appears to depend on the nature of the DNA binding site; for example, inserting the TLX HRE repeat into the p21 promoter reduces its expression, whereas inserting a monomeric HRE into the Wnt7α promoter activates gene expression [54]. TLX is generally considered to bind HRE half-sites as a monomer, yet the homodimer crystal structure of TLX and the opposing effects of different HREs raise the question of whether TLX binds as a monomer or dimer, and whether additional co-regulators guide TLX effector functions [59, 49].

3.2.5. Molecular interactions with co-regulators

Transcriptional functions of NRs, including TLX, are regulated by the recruitment of either CoAs or CoRs. Despite its importance, little is known about the TLX interaction partners and the mechanism of regulation. Analysis of neuronal stem cell lysate by immunoprecipitation experiments have identified histone deacetylases (HDAC3 and HDAC5) as direct binding partners of TLX. Deacetylation of histone proteins tightens DNA-interactions, leading to a condensed heterochromatin structure. Here, transcription factors and the RNA polymerase are unable to bind as they can only open, accessible euchromatin [66, 71]. Studies identified two HDAC5 interaction domains within TLX: residues 359 – 385 and 340 – 359. Both domains contain the conserved binding motif IXXLL (whereas X can be any amino acid residue). Recruitment of HDACs to TLX promotes the repression of target genes, thereby enabling NSC proliferation [66].

Another important histone modifying enzyme, LSD1, is expressed in undifferentiated NSCs [65]. LSD1 plays a key role in histone methylation, which marks regions of active or repressed transcription. For instance, trimethylation of lysine 4 on histone 3 (H3K4me3) is only associated with transcriptionally active regions, whereas trimethylation of lysine 27 on histone 3 (H3K27me3) marks transcriptionally repressed regions [63, 65].

Furthermore, in a yeast-two hybrid system TLX was identified to bind the co-repressor atrophin 1 (ATN1). In mice, ATN1 is expressed in retinal progenitor cells (RPCs) aiding the repression of TLX target genes and therefore cell differentiation [57, 72].

3.2.6. The role of TLX in disorders of the nervous system and brain cancer

As TLX plays a key role during NSC proliferation and self-renewal, its dysregulation during development and adulthood can be associated to neural and mental disorders. Changes in size and cellular composition of the limbic system have been associated with pathological behaviors observed in TLX KO mice [50, 55]. Interestingly, both restoring TLX expression and overexpressing TLX were able to rescue and even enhance NSC proliferation, as well as improve memory and learning abilities, underscoring the potential of TLX as a therapeutic target [73]. Limbic structures, such as the amygdala, orbitofrontal cortex and the hippocampus are involved in emotion, reward value, memory and learning [74]. Dysfunctions or lesions in these regions are associated with psychiatric disorders, such as schizophrenia, and neurodegenerative diseases, such as Alzheimer's disease [55, 73, 75].

Genome-wide linkage and association studies (GWAS) have revealed a connection between several genetic loci and hereditary bipolar disorder (BD), highlighting its polygenic nature [76]. Notably, a strong association has been determined to the long arm of chromosome 6 (6q21), where the TLX gene is located [75]. BD is a severe mood disorder affecting activity and energy levels of patients with fluctuating periods of mania and depression [77]. Additionally, changes in micro-RNA (miRNA) levels that regulate TLX expression have been associated to BD as well as schizophrenia, further strengthening the association between TLX dysregulation and psychiatric disorders [75].

Glioblastoma multiforme (GBM) is among most aggressive and fast-progressing brain tumors with a median survival time of just 15 months. In multiple glioma and glioma stem cells TLX overexpression has been linked to tumor initiation and progression, particularly in the context of p53 deletion [78, 79]. Studies in mouse models overexpressing TLX have suggested that TLX upregulation in NSCs and NPCs can promote differentiation and migration out of the stem cell niche, bypassing age-related senescence and promoting tumorigenesis. An analysis of 41 glioblastoma patient samples revealed elevated or high-copy number TLX expression in approximately 25% of the cases [67]. Additionally, TLX overexpression, combined with loss of PTEN, p21, or both, has been implicated in glioblastoma progression [80]. These findings suggest that while TLX is critical for normal NSC function, its dysregulation can have devastating oncogenic effects.

Given its dual roles, TLX represents a compelling therapeutic target. In psychiatric and neurodegenerative disorders, TLX agonists could promote NSC proliferation and neurogenesis, aiding in memory, learning and emotional regulation. Conversely, in glioblastoma, suppression of TLX's constitutive repressive state through inverse agonists could inhibit tumor progression and enhance survival [81]. Further

research is needed to elucidate TLX's complex functions and to develop targeted therapies for these conditions.

3.3. Potential TLX modulators and one endogenous ligand

As TLX is believed to be constitutively active its repressive state, two mechanisms of actions can be exploited to modulate its activity. Agonists bind TLX, enhancing its repressive function by recruiting CoRs or blocking of CoA interactions. On the other hand, inverse agonists reduce TLX activity by disrupting its repressive state, thereby facilitating the expression of target genes (***Figure 2B***).

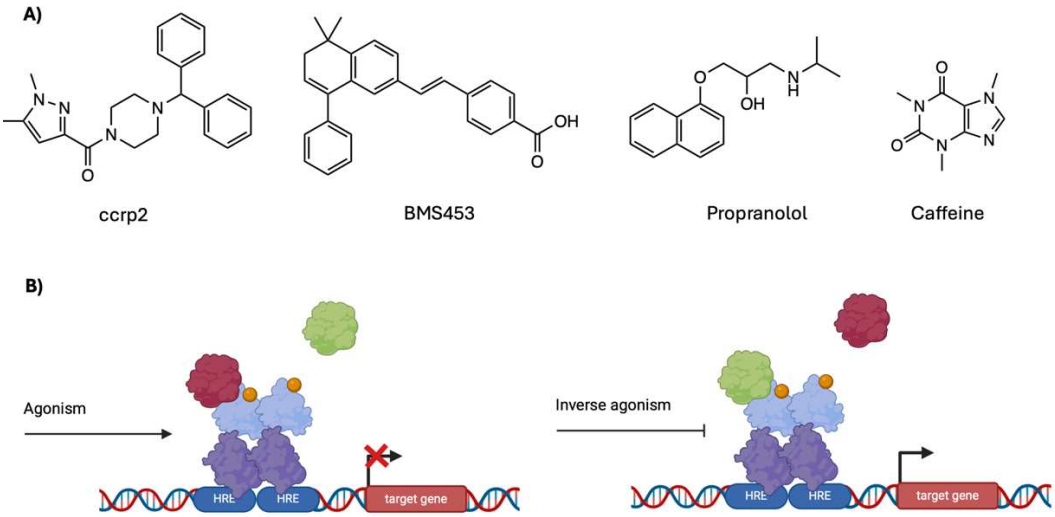

Figure 3: *Recently published TLX modulators and their mode of action.* ***A****) Structures of recently published TLX agonists ccrp2, BMS453, propranolol and inverse agonist caffeine.* ***B****) Illustrated mode of action of TLX agonists and inverse agonists. Here, a TLX homodimer is depicted in light blue (LBD) and purple (DBD) bound to a ligand (orange). Co-activator is shown in green and co-repressor is represented in red. Here, a TLX-DBD homodimer is bound to its hormone response elements (HREs). This figure was created in BioRender.com and adapted from Griffett et al., 2020* [81]*.*

In 2014, Benod *et al.* were the first to identify three potential TLX agonists using differential scanning fluorometry (DSF) to assess shifts in protein thermostability, screening an inhouse library of around 20,000 compounds. Using a Octet Red384 system, which employs an optical sensor to determine binding kinetics between the immobilized target protein and the hit molecules, three compounds were identified: ccrp1, ccrp2 and ccrp3. These compounds bind directly to human TLX-LBD with high nanomolar (650 nM) to low micromolar (27 µM) affinity. The activity of these compounds was further validated in a cell-based Gal4-luciferase assay, demonstrating enhancement of TLX repressor function [42]. Interestingly, two of the hits, famprofazone (ccrp1), a nonsteroidal anti-inflammatory agent, and dydrogesterone (ccrp3), a synthetic pregestational hormone, are already approved drugs [82, 83]. The hit compound ccrp2 derived from the Maybridge HitFinder Screening Library.

However, subsequent studies by Griffett and colleagues were failed to replicate these findings. The compounds ccrp1-3 were inactive in both, cell based and biochemical assays. Instead, they identified natural and synthetic retinoids as potential TLX modulators. In their Gal4-luciferase based screening assay, synthetic retinoic acid BMS453 was identified as a potent TLX agonist (IC_{50}: 159 nM), which was verified by three additional binding experiments. In parallel, natural retinoid ligands, such as all-trans retinaldehyde (ATRAL), were identified as effective TLX inverse agonist (EC_{50}: 1.72 µM). Its enantiomers 9-cis, 11-cis and 13-cis retinaldehyde also modulated TLX activity, though less effectively. The effects of BMS453 and ATRAL on TLX target gene transcription supported these findings, with BMS453 enhancing TLX repressor function, while ATRAL decreased TLX repressor activity, leading to increased target gene expression [81].

In addition to the TLX modulators, oleic acid (18:1ω9), a monounsaturated fatty acid, has been proposed as an endogenous ligand of TLX that promotes proliferation and differentiation of NSCs and NPCs [84]. Moreover, Faudone *et al.* identified propranolol as a TLX agonist capable of reducing cell proliferation and migration in the glioblastoma cell line T98G. In their study, a library of 480 drug fragments (Prestwick Chemical Libraries ®) was screened in a Gal4-luciferase reporter gene assay, yielding several initial hits [85, 86]. Substructure analysis identified two FDA-approved drugs: propranolol and tadalafil, whereas propranolol exhibited superior efficacy. Furthermore, rational fragment fusion of the most promising hit led to the development of the potent lead molecule GFS105, an orthogonally validated TLX agonist [87]. This molecule served as a lead for further TLX agonist design and as a tool to better understand TLX modulation and its therapeutic potential [87]. Additionally, xanthine derivates, including caffeine, were also investigated as TLX modulators. Some of these derivatives were found to reduce the repressive effects of TLX on its target genes, with receptor-ligand interaction validated through isothermal titration calorimetry (ITC) and homogeneous time-resolved FRET (HTRF) assays [88, 89].

Table 2: *List of published TLX modulators.*

Name	IUPAC or common name	Mode of action	Reference
Ccrp1	Famprofazone	Agonist	Benod *et al.*[42]
Ccrp2	1-(1,5-dimethylpyrazole-3-carbonyl)-4-(diphenylmethyl)piperazine	Agonist	Benod *et al.*[42]
Ccrp3	Dydrogesterone	Agonist	Benod *et al.*[42]
BMS453	(E)-4-(2-(5,5-dimethyl-8-phenyl-5,6-dihydronaphthalen-2-yl)vinyl)benzoic acid	Agonist	Griffett *et al.* [81]
ATRAL	All-trans retinaldehyde	Inverse agonist	Griffett *et al.* [81]
Oleic acid	(9*Z*)-Octadec-9-enoic acid	Endogenous agonist	Kandel *et al.* [84]
Propranolol	1-naphtalen-1-yloxy-3-(propan-2-ylamino)propan-2-ol	Agonist	Faudone *et al.* [85]
Caffeine	1,3,7-trimethyl-3,7-dihydro-1*H*-purine-2,6-dione	Inverse agonist	Faudone *et al.* [88]
GFS105	2-butoxy-N-(3-(4-methyl-1H-imidazol-1-yl)-5-(trifluoromethyl)phenyl)quinoline-4-carboxamide	Agonist	Faudone *et al.* [87]

3.4. Chemogenomics

Since the Human Genome Project, which was completed at the beginning of this century, approximately 20,000 protein-coding genes have been identified [90, 91]. However, FDA-approved drugs or experimental small molecules have been described for only about 600 to 700 of these target encoding genes [8, 92]. The interdisciplinary field of chemogenomics combines the knowledge of pharmacology, chemistry, and biology aiming to bridge the gap between known disease-related genes and drugged targets [93]. Prioritizing disease-relevant phenotypic aspects during the screening process can help minimize poor outcomes during the later stages of drug development. Inefficiency remains a common reason for the failure of drug candidates [94].

Chemogenomics leverages high-throughput screenings (HTSs) of diverse compound libraries against families of functionally related proteins aiming to identify or validate drug targets or small molecules responsible for phenotypic changes [93, 95]. These chemogenomic libraries include a broad spectrum of molecules that are chemically, pharmacologically and structurally diverse and should be considered as a set. In addition, compounds should exhibit drug-like properties and annotated biological activity [94]. In contrast, chemical probes, selective small molecules, are used for functional studies or target validation (***figure 4***). High quality chemical probes exhibit high specificity and potency and therefore provide a precise tool for investigating the target's biological function, e.g., deciphering cellular signaling pathways [96].

Screening of chemogenomic libraries aims to identify new druggable targets, e.g., when screening underexploited target groups or "undruggable" targets like orphan receptors. Assessing changes in phenotypic outcomes allows target validation as well as deciphering its biological function. Rather a byproduct than a goal of chemogenomics is for example also the identification of novel hit molecules or the repurposing of already approved drugs [95]. Nevertheless, it is almost an impossible task to perform large scale screenings in both directions due to the immense diversity of chemical molecules and biological targets. Therefore, it is more feasible to screen a curated library of compounds against specific target families within a biological system, followed by testing identified compounds on genetic variants or other targets of the same family [94, 97]. In general, chemogenomics can be divided into forward and reverse approaches, similar to forward and reverse genetics. Forward chemogenomics aims to identify a target based on changes in a defined phenotype whereas the purpose of reverse chemogenomics is to describe a phenotype based on compound-target interaction (***figure 4C***) [98].

In this study, a diverse set of validated TLX agonists was tested in vitro to explore phenotypic outcomes. These compounds originated from an initial drug fragment screening, and the most promising hits were advanced through structure-activity relationship (SAR) studies conducted by PhD students EH and TS [99]. Given the limited understanding of phenotypic changes associated with TLX modulation, employing a chemogenomic strategy offers dual benefits: it not only aids in further lead optimization but it can also provide a robust screening system for validation purposes.

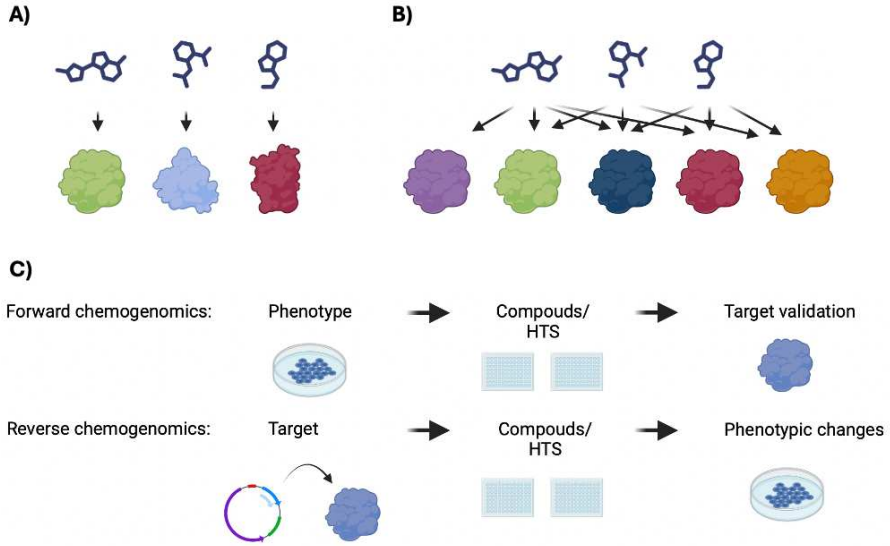

Figure 4: *Basic overview of chemogenomics.* ***A****) Chemical probes used to investigate a specific target.* ***B****) A Chemogenomic library that is screened against multiple targets, e.g. a target family represented here in different colors.* ***C****) Simple overview of the principles of forward and reverse chemogenomics. HTS: high throughput screening. This figure was created in BioRender.com and figure A and B were adapted from Merk and Chaikuad, 2023* [95]*.*

3.5. Chemogenomic set of chemically diverse TLX modulators

The compound set used in this study comprises 12 molecules, including the FDA-approved drug propranolol (**1**). These compounds, detailed in ***Table 3***, represent four distinct molecular scaffolds: **1**, caffeine (**2**), compound **3** to **8**, and compounds **9** to **12**. **1**, a non-selective β-adrenergic antagonist indicated to treat heart conditions, anxiety or migraines, was only recently identified as a TLX agonist [85, 100]. Similarly, **2**, previously characterized as a TLX inverse agonist, was included into the selection [88]. An inactive derivative of the lead compound **4**, compound **3**, was used as a negative control throughout the experiments. The selection of TLX agonists also included lead compounds **4** and **9.** They served as scaffolds for rational optimization which led to the development of compounds **5** to **8** as well as **10** to **12**.

Table 3: *Summary of TLX modulators selected for this study. First the compound number is indicated in the table below, as well as the structure, mode of action (MoA), potency (EC_{50}) derived from hybrid reporter gene assays using a human TLX-LBD construct. Binding affinity was evaluated by isothermal titration calorimetry (ITC). The data was kindly provided by Dr. GF, EH and TS.*

Compound	Structure	MW (g/mol)	MoA	EC_{50} (hTLX)	K_d (hTLX)
1	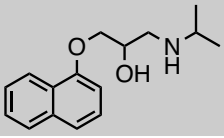	259.35	Agonist	32±4 µM	
2	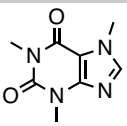	191.19	Inverse agonist	9±2 µM	3.2 ± 1.8 µM

3	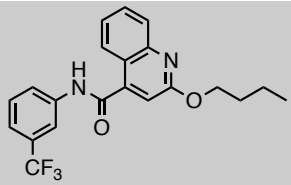	388.39	Inactive	Inactive	-
4	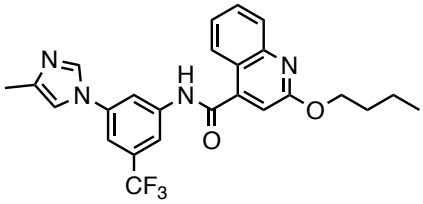	468.48	Agonist	0.25±0.15 μM	1.6 ± 0.5 μM
5	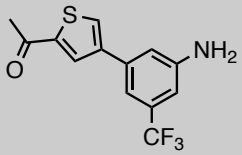	285.28	Agonist	1.5 ± 0.5 μM (0.19±0.06)	-
6	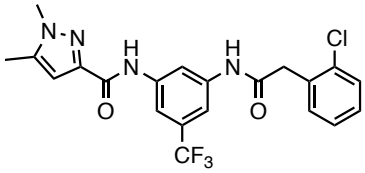	450.85	Agonist	0.1±0.03 μM (0.23±0.04)	0.16 μM
7	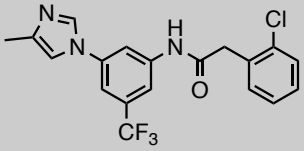	393.79	Agonist	0.20±0.05 μM (0.14±0.04)	0.36 μM
8	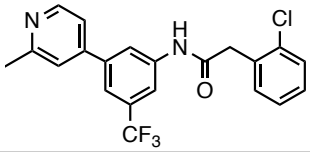	404.82	Agonist	0.14 ± 0.04 μM (0.1±0.05)	0.06 μM
9	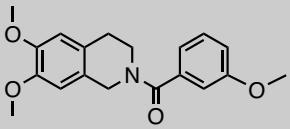	327.15	Agonist	6.5±1.0 μM (8.2±0.5)	3.4 μM
10	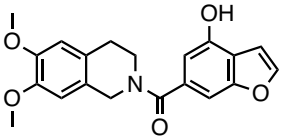	353.37	Agonist	0.7±0.1 μM (0.35±0.05)	0.23 μM
11	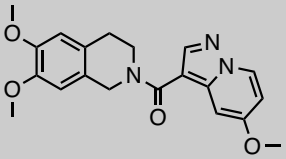	367.41	Agonist	0.5±0.1 μM (0.26±0.04)	0.05 μM
12	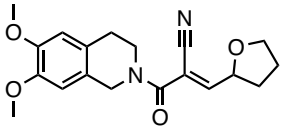	342.40	Agonist	0.5±0.1 μM (0.29±0.07)	0.12 μM

Figure 5A depicts the development process that led to the generation of compounds **5** to **8**. The initial hit comprises a benzene ring with an aniline group at position 1, a methyl-imidazole at position 3, and a trifluoromethyl at position 5. This compound, in combination with ccrp2, was used to generate a

pharmacophore model, which identified three essential elements: a hydrogen bond doner, an acceptor and an aromatic core. Fused derivatives were synthesized based on this model, leading to a potent TLX agonist **4** (EC_{50}: 0.25±0.15 µM) with a great affinity to the TLX-LBD (K_d: 1.6 ± 0.5 µM) [87]. SAR studies during lead optimization produced an inactive compound **3**, lacking the methyl-imidazole moiety, along with compounds **5** to **8**. The trifluoromethylphenyl group made up the core and remained present in all the derivatives. Modifications were primarily made to the heterocycle at position 3, while the amide linkage remained consistent across all compounds. Compounds **6** to **8** feature a trifluoromethyl benzene core. All derivatives exhibited superior efficacy and affinity for TLX compared to their precursor, as detailed in ***Table 3***. In parallel, a second hit, xanthine (initial hit B), was also selected as a starting point for further drug development (***Figure 5B***). Structurally similar to **2**, xanthine lacks two methyl groups. SAR-based lead discovery from the xanthine core led to the identification of several compounds, which were then optimized to generate lead compound 9. The core of compounds **9** to **12** is a dimethoxy-dihydro isoquinoline, linked via an amide bond to varying moieties.

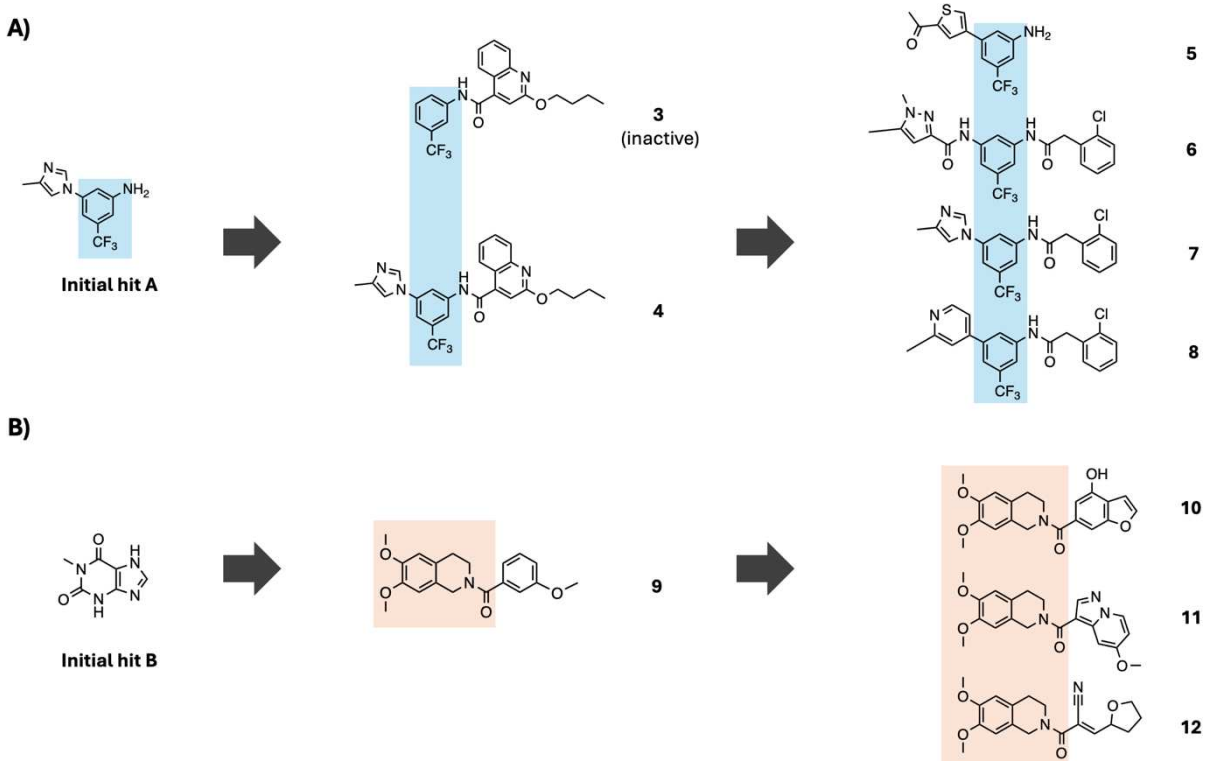

Figure 5: *Hit to lead optimization based on initial hits A and B.* ***A****) Lead optimization of initial hit A, resulted in potent TLX agonists* ***5*** *to* ***8****.* ***B)*** Hit to lead optimization based on initial hit B/ xanthine resulted in compounds **10** – **12** based on compound **9**.

4. Objective

Despite its key role during neurogenesis and differentiation of NSCs and NPCs, TLX's biological function remains poorly characterized and only few modulators have been identified to date. Gaining more insights into TLX's functions will help to further develop TLX agonists in order to improve cognitive abilities and inverse agonists to tackle glioblastoma.

In this study, we aim to investigate the phenotypic and biochemical effects upon TLX modulation using a set of 12 compounds within a chemogenomic framework. Previous studies have shown that TLX can exist as both monomers and dimers. Given that the protein dimerization often impacts stability and function, we hypothesize that TLX modulation could affect TLX dimerization or dimer stability, leading to changes in its biological activity. To test this hypothesis, we express and purify human TLX-LBD and will use HTRF assays to quantify TLX homodimerization.

Additionally, we will evaluate downstream molecular effects (gene expression) by qPCR and phenotypic changes (proliferation, migration and metabolic activity) in selected TLX expressing cell lines by monitoring confluence and performing WST-8 and HOECHST33342 staining assays. By integrating these approaches, we aim to provide novel insights into the mechanisms of TLX and its role in cellular processes.

5. Materials

5.1. TLX modulators

TLX-modulators were provided by Prof. DM, EH and TS. Reference compounds propranolol and caffeine were purchased form Sigma-Aldrich (Merck, Darmstadt, Germany) or Carl Roth GmbH (Karlsruhe, Germany). All compounds were dissolved in dimethlysulfoxide (DMSO) and stored as aliquots of 1 mM or 100 mM stocks at -80°C.

Table 4: *Test compounds and solvent.*

Product	CAS Nr.	Catalogue Nr.	Supplier
Caffeine	58-08-2	N815	Roth
DMSO	67-68-5	1029500	Sigma-Aldrich
Propranolol	318-98-9	P0884	Sigma-Aldrich

5.2. Biochemical assays

Table 5: *Protein expression and purification – chemicals and technical supply.*

Product	CAS Nr.	Catalogue Nr.	Supplier
Agar-Agar	9002-18-0	6494.2	Roth
Amicon® 10K MWCO		UFC9010	Millipore
Amicon® 30K MWCO		UFC9030	Millipore
Ampicillin	69-52-3	0339-EU-25G	VWR Life Science
Adenosine triphosphate (ATP)	34369-07-8	102800100	Thermo Scientific
Beta-mercaptoethanol		M6250-100ML	Sigma-Aldrich
Chloramphenicol	56-75-7	C0378-100G	Sigma-Aldrich
cOmplete, EDTA-free	30827-99-7	11873580001	Roche
Quick Coomassie Stain		#GEN-QC-Stain	Proteinark
D-(+)-biotin	58-85-5	A14207.06	Thermo Scientific
D-(+)-Glucose monohydrate	14431-43-7	24371.297	VWR Chemicals
DNase I	9003-98-9	11284932001	Roche
Dithiothreitol (DTT)	3483-12-3		Roth
Glycerol	56-81-5	1053.1000	ORG-Laborchemie
2-[4-(2-hydroxyethyl)piperazin-1-yl]ethanesulfonic acid (HEPES)	7365-45-9		Sigma-Aldrich
HiLoad 16/600 Superdex75		28989333	Cytiva
HisTrap™ FF 5mL		17525501	Cytiva
IMAC Sepharose™ 6 Fast Flow		GE17-0921-07	GE Healthcare
Imidazole	288-32-4	56750-1KG	Sigma-Aldrich
Isopropyl β- d-1-thiogalactopyranoside (IPTG)	367-93-1	I6758-10G	Sigma-Aldrich
K_2HPO_4	10028-24-7		AppliChem
Kanamycine		T832.3	Roth
KH_2PO_4	7778-77-0		Grüssnig
Lysozyme	12650-88-3	#HY-B2237/CS-7671	MedChemExpres
$MgCl_2$	7791-18-6	120171000U	Grüssnig

$MgSO_4$	7487-88-9		Grüssnig
NaCl	7547-14-5	27810.295	VWR Chemicals
$NaH_2PO_4xH_2O$		12299	Grüssing
$NiSO_4$	10101-97-0	121991000U	Grüssnig
Poly(ethyleneimine) (PEI)	9002-98-6	03880-500ML	Sigma-Aldrich
SERVAGel™TG Prime™		43273.01	SERVA
Single use filter 0.20 µm		7699822	LabSolute
Single use filter unit		7699822	T.H. Geyer
SnakeSkin™ Dialysis		68035	ThermoScientific
Spectinomycin	22189-32-8	S4014-5G	Sigma-Aldrich
Tris(2-carboxyethyl)phosphin (TCEP)	51805-45-9	C4706-50G	Sigma-Aldrich
Tabacco etch virus (TEV) protease		Batch 6, UL (1.558 mg/mL) 03.11.2023 Batch 5, VM (3 mg/mL) 06.2024	
TRIS	77-86-1	5429.2	Roth
Trypton/Pepton	91079-40-2	6681.3	Roth
Yeast extract	8013-01-2		Sigma-Aldrich

Table 6: *HTRF assay reagents.*

Product	CAS Nr.	Catalogue Nr.	Supplier
384-well microplate		784075	Greiner
Adhesive aluminum foil		AB0626	ThermoScientific
3-[(3-Cholamidopro-pyl)dimethylammonio]-1-propansulfonat (CHAPS)		1479.3	Roth
KF	7789-23-3	201350250	Acros organics
HTRF streptavidine Tb-cryptate		610SATLB	Revvity

5.3. In vitro assays

Retinal pigment epithelial cell line ARPE-19 (CRL-2302™) and glioblastoma T98G cells (CRL-1690™) were purchased from American Type Culture Collection (ATCC). Lung cancer cell line A549 (ACC 107) and HEK293T cells (ACC 635) were purchased from the German collection of microorganisms and cell cultures GmbH (DSMZ).

Table 7: *Cell culture* materials *and assay reagents.*

Product	CAS Nr.	Catalogue Nr.	Supplier
12-well plates		665180	Greiner
12-well plates		126101	Thermo Fisher
96-well plates		655180	Greiner
96-well plates		83.3924	Sarstedt
Cell counting kit-8 (CCK-8)		HY-K0301	MedChemExpress
Cell culture dishes		83.093	Sarstedt
Charcoal Stripped (CS)-FCS		A3382101	Gibco
Collagen G		L7213	Sigma-Aldrich
Counting Chamber		0640030	Paul Marienfeld
Countig Chamber coverslips		351000	Paul Marienfeld
DMEM/F12		11320033	Gibco

Dulbecco's Modified Eagle Medium (DMEM) high glucose		D5796	Sigma-Aldrich
Fetal Calf Serum (FCS)		F7524	Sigma-Aldrich
HOECHST33342	23491-52-3	ab228551	Abcam
KCl	7447-40-7	191494	AppliChem
KH_2PO_4	7778-77-0	141509	AppliChem
Penicillin/Streptomycin		P4333	Sigma-Aldrich
Sodium pyruvate		S8636	Sigma-Aldrich
Trypsin/Ethylenediaminetetraacetic acid (EDTA) solution		T4174	Sigma-Aldrich
T-75 flasks		C7231	Sigma-Aldrich

Table 8: *Quantification of TLX target gene expression.*

Product	**Catalogue Nr.**	**Supplier**
10x Taq buffer	B55	Thermo Scientific
5x buffer	15307696	Fisher Scientific
Acrylamide	7906.3	Roth
BioStab PCR Optimizer II	LC120	BiTop
Bovine serum albumin	B14	Fisher Scientific
Cell scraper	**C6106**	Greiner
dNTPs 25mM	R0182	Fisher Scientific
DTT	15307696	Fisher Scientific
E.Z.N.A. ® total RNA kit I	R6834-02	Omega Bio-Tek
Hexanucleotides	11277081001	Merck
MgCl2 25mM	R0971	Fisher Scientific
NucleoBond® Xtra Maxi Kit	REF 740414.50	Macherey-Nagel
RNasin	N2515	Promega
Superscript	15307696	Fisher Scientific
SYBR green I	S9430	Sigma-Aldrich
Taq Polymerase	M0273X	New England Biolabs
96-well PCR plate	EP0030133307	Eppendorf SE

Table 9: *Technical equipment.*

Product	**Model**	**Supplier**
ÄKTA pure™	ÄKTA pure™25	Cytiva
Heatblock	Thermal Shake *lite*	VWR
Incubator	Heracell 150i	Thermo Fischer
Microscope	AE31E	Motic
Microscope Camera	Moticam 1080	Motic
Multiplate reader	Spark® Cyto	Tecan Group
Multiplate reader	Spark®	Tecan Group
NanoDrop	NanoDrop One^C	ThermoScientific
PeqLab PerfectBlue™	PeqLab PerfectBlue™ Twin L	VWR
PerfectBlue™ power supply	Universal	VWR
qPCR machine	qTower^3 G	Analytik Jena
Sonicator	Vibra Cell™ VCX 500	Sonics
Tabletop centrifuge	GT4 centrifuge	Fisherbrand
Thermo cycler	XT^{96}	VWR
Ultracentrifuge	Avanti J-26S XP	Beckman Coultier
Ultrapure water system	MiliQ® EQ 7000	Merck Millipore

6. Methods

6.1. Biochemical characterization

Plasmids were kindly provided by Dr. JH or purchased from Takara Bio Inc. (pGro7 encoding for GroEL/ES, catalogue nr.: 3340, Kyoto, Japan) and stored at -80°C until further use (***Table 10***). Streptavidine for the streptavidine pull-down assay was kindly provided by Dr. VM.

Table 10: *Overview of plasmids expressed in E. coli for subsequent protein purification. All plasmids are codon-optimized and were kindly provided by Dr. JH. TLX(NR2E1)-LBD spanned from amino acid residue 150 to the end derived from isoform 1. MBP: maltose binding protein. sGFP: superfolder green fluorescent protein. PolyN describes a sequence of a poly asparagine sequence and His-tag an array of 8-10 histidine residues necessary for purification. Tabacco etch virus (TEV) site describes the cleavage site 'ENLYFQ' of the TEV protease. Avitag indicates Avitag fusion proteins.*

Plasmid name	MBP	PolyN	His-tag	TEV site	Avitag	TLX-LBD	Plasmid backbone
Avitag-TLX-LBD	yes	yes	yes	yes	yes		pMal
sGFP-TLX-LBD			yes	yes		NR2E1	pET29BH4
sGFP			yes	yes		NR2E1	pET29BH4
BirA			yes				pET21a
GroEL/ES							pG-KJE6

6.1.1. Plasmid expansion

For plasmid transformation, 400 µL of competent *E. coli TSS* was added to 20 ng of plasmid DNA (pDNA) and incubated on ice for 30 min. At 42°C heat shock was performed for 2 min; cells were rested on ice for 5 min before 2.6 mL of Luria broth (LB) medium was added to the mix. The bacteria were then incubated for 1 h at 37°C, shaking at 145 rpm. 50 or 150 µL of the bacteria suspension were plated on LB agar selection plates containing the respective antibiotic and incubated at 37°C for 14 – 16 h. Six colonies were picked to inoculate 5 mL of LB medium containing the respective antibiotic concentration (***Table 11***). The preculture was cultivated for 6 h at 37°C and 180 rpm shaking, before transferred into a larger 400 mL LB medium flasks supplemented with the respective antibiotic and incubated for 14 – 16 h at 37°C and 180 rpm shaking. Subsequently, the cell suspension was centrifuged for 15 min at 5000 g and 4°C. The pellet was collected, and plasmid purification was performed following the manufacturer's protocol (NucleoBond® Xtra Maxi Kit by Macherey-Nagel, Düren, Germany). For quality control all plasmids were sequenced by Oxford Nanopore Technology (ONT) Sequencing (Eurofins Genomics, Luxembourg city, Luxembourg).

Table 11: *List of plasmids and their respective antibiotic resistance gene. Additionally, the appropriate antibiotic concentration that needs to be added to the cultivation medium is indicated as well as the bacterial E. coli strain later used for protein expression.*

Plasmid name	Antibiotic resistance	Concentration	Bacterial strain (*E. coli*)
Avitag-TLX-LBD	Ampicillin	100 µg/mL	*Rosetta*™
sGFP-TLX-LBD	Kanamycin	35 µg/mL	*BL21*
sGFP	Kanamycin	35 µg/mL	*Rosetta*™
BirA	Spectinomycin	50 µg/mL	*Rosetta*™
GroEL/ES	Chloramphenicol	25 µg/mL	-

6.1.2. Protein expression

To obtain bacteria expressing Avitag-TLX-LBD, sGFP-TLX, sGFP, and BirA (see ***Table 11***) the respective plasmids were transformed into competent *E. coli* bacteria cells. Avitag-TLX-LBD, sGFP-TLX, and BirA were transformed into competent *E. coli Rosetta*™ cells, a BL21 derivative host strain that supplies rare codons to improve eukaryotic protein expression. Superfolder GFP (sGFP) was transformed into 50 µL competent *E. coli BL21* cells, kindly provided by Dr. VM. Both sGFP and the sGFP-TLX fusion protein encoding plasmids were co-transformed with pGro7 (Takara, Kyoto, Japan) in a 1:1 ratio to co-express the GroEL/ES chaperone system, enhancing proper protein folding. A total amount of 50 ng sGFP and GroEL/ES (pDNA) were added to 50 µL of competent *E. coli BL21* cells and incubated on ice for 30 min, followed by heat-shocking for 45 seconds at 42°C. The cells were placed on ice for 5 min, and 0.5 mL of LB medium was added. The same procedure was performed for sGFP-TLX-LBD, Avitag-TLX-LBD, and BirA, except that 400 µL of competent *E. coli Rosetta*™ cells were used, and 100 ng of pDNA was added, followed by 1 mL of LB medium after the heat shock.

After transformation, *E. coli* cells were incubated at 37°C for 1h while shaking at 145 rpm. The cell suspension was then plated onto LB/agar plates containing either 100 µg/mL ampicillin (MBP-Avi-TLX) or 35 µg/mL kanamycin plus 25 µg/mL chloramphenicol (for sGFP and sGFP-TLX-LBD co-expressed with GroEL/ES), or 50 µg/mL spectinomycin (BirA). Plates were incubated for 16 – 18 h at 37°C. Seven to ten colonies were picked to inoculate 50 mL of LB medium with the corresponding antibiotic. Precultures were grown at 37°C for 16 h – 18 h, shaking at 200 rpm. Bacteria cultivated in LB medium supplemented with ampicillin were centrifuged at 5000 g for 5 min to remove beta-lactamases and re-suspended in 10 mL of supplemented Terrific Broth (TB) medium before being transferred to the larger main culture flasks. The bacteria suspension was evenly distributed to five large flasks (880 mL) of supplemented TB medium containing the respective antibiotics, as well as a final concentration of 17 mM KH_2PO_4 and 72 mM K_2HPO_4 and incubated at 37°C and 180 rpm shaking. Upon reaching the optical density of 0.7 at λ= 600 nm (OD_{600}), temperature and shaking were reduced to 18°C and 120 rpm, respectively. To induce the expression of the chaperone GroEL/ES co-expressed in sGFP and sGFP-TLX-LBD, L-(+)-arabinose was added to each flask at a final concentration of 1 g/L. When the OD_{600} reached 1.0, isopropyl-β-D-1-thiogalactopyranosid (IPTG) was added at a final concentration of 0.5 mM

to initiate protein production. The expression cultures were incubated at 18°C and 120 rpm shaking for 18 h.

Cells were harvested by centrifugation at 5000 g for 15 min at 4°C, and the cell pellets were either stored at -80°C or processed immediately. Pellets derived from 4L of expression culture were resuspended by vortexing in 200 mL lysis buffer A (400mM NaCl, 20 mM NaP_i pH 7.8 and 10% (w/v) glycerol) supplemented to a final concentration of 20 mM β-mercaptoethanol, 5 mM imidazole, 4x cOmplete EDTA-free protease inhibitor cocktail (Roche AG, Basel, Switzerland), 0.1 mg/mL DNase I (Roche AG, Basel, Switzerland), 0.7 mg/mL lysozyme (MedChem Express, Princeton, NJ, USA), 10 mM $MgSO_4$ and 10 mM ATP (Thermo Fisher Scientific, Darmstadt, Germany). The suspension was sonicated at an 40% amplitude (Ampl35%) with 2-minute pulses followed by 7 min pause, repeated three times (Sonics, Newtown, CT, USA) to promote cell lysis. After sonication, polyethyleneimine (PEI) was added to the lysate at a final concentration of 0.2% to precipitate nucleic acids. To remove cell debris, the lysate was centrifuged at 5000 g for 15 min at 4°C, and the supernatant was transferred for ultracentrifugation at 40,000 g for 30 min at 4°C. The supernatant containing the protein was then collected and filtered using 0.2 µm polytetrafluorethylene (PTFE) single use filter (T.H. Geyer, Renningen, Germany) before proceeding with protein purification.

6.1.3. Protein purification of Avitag-TLX-LBD

Immobilized metal affinity chromatography (IMAC) was performed by loading the sample onto a buffer A (400 mM NaCl, 20 mM NaH_2PO_4 pH 7.8, 10% (m/v) glycerol and 1 mM TCEP) equilibrated nickel (Ni^{2+}) column (HisTrap™ FF 5 mL, Cytiva, Washington D.C., USA) able to bind the negatively charged histidine residues of the His-tagged protein. The flow through was collected and the column washed with 15 column volumes (CVs) of the respective binding buffer A (400 mM NaCl, 20 mM NaH_2PO_4 pH 7.8, 10% (m/v) glycerol and 1 mM TCEP). The protein was eluted by applying 5 CVs elution buffer A supplemented with stepwise increasing imidazole content from 30 mM, 100 mM to 300 mM. Sample fractions containing the protein of interest were identified by sodium dodecyl sulfate–polyacrylamide gel electrophoresis (SDS-PAGE) and subsequently pooled.

To reduce imidazole content, the sample was transferred into a 3.5K MWCO snakeskin membrane bag for dialysis and stirred overnight at 4°C in 2L of buffer A. In a separate step, to avoid protein precipitation, the sample was transferred into a FALCON tube and TEV protease, kindly provided by UL, was added in an approximately 1:10 ratio to incubate overnight at 4°C on slight rotation. To separate TEV protease, MBP-tag, uncleaved protein, and successfully cleaved protein a reverse IMAC was performed using the same conditions as for the first IMAC. However, here the flow through and not the wash out was collected, as cleaved protein would bind considerably less to the Ni^{2+} column. For overnight biotinylation the protein sample was first concentrated in an 10K MWCO AMICON tube (Millipore, Burlington, MA,

USA) to a volume of 30 mL and a final concentration of 0.5 mM biotin (Thermo Fisher Scientific, Darmstadt, Germany), 0.5 mM ATP, 5 mM $MgCl_2$ and BirA in a 1:10 molar ratio.

To increase separation efficiency of cleaved and uncleaved product a second reverse IMAC was performed using a gravity affinity chromatography column containing 10 mL IMAC Sepharose™ 6 Fast Flow beads (GE Healthcare, Chicago, IL, USA) charged with 4 CV 0.1 M $NiSO_4$. Ni^{2+} charged sepharose beads were equilibrated in 2 CVs binding buffer A, then transferred into the sample. The mix was incubated for 45 min on slow rotation to ensure thorough mixing before transferred back into the column where the beads were allowed to settle before washing with 2 CVs of binding buffer A while collecting the flow through. Elution of remaining protein was performed using each 2 CVs of 50 mM, 100 mM and 300 mM imidazole supplemented elution buffer A. Protein content was estimated by measuring absorption at λ= 280 nm (NaonDrop, Thermo Fisher Scientific, Darmstadt, Germany) in reference to imidazole supplemented buffer A corresponding the to the elution steps. Fractions containing protein of interest were identified by SDS-PAGE, collected and carefully concentrated by centrifuging at 3000 g at 4°C in 5 to 1 min steps using a 10K MWCO AMICON (Millipore, Burlington, MA, USA).

Samples were applied to size exclusion chromatography using HiLoad 16/600 Superdex75 column (Cytiva, Washington D.C., USA) equilibrated in HTFR buffer (25 mM HEPES pH 7.5, 10% (w/v) glycerol and 5 mM DTT). Eluted protein was collected and carefully concentrated before a second size exclusion chromatography (HiLoad 16/600 Superdex75 column, Cytiva, Washington D.C., USA) was run using the same conditions. Sample validation was completed by SDS-PAGE and streptavidine pull down assay. Therefore, excess streptavidine was added to a protein sample in a 10:1 molar ratio and incubated for 1h at 4°C. Subsequently, the sample was split in two whereas one of the samples then was denatured at 95°C for 10 min. Efficiency of biotinylation was then evaluated by SDS-PAGE.

6.1.4. Protein purification of BirA

Protein expression of BirA followed the procedure described above. However, after harvesting the cells were resuspended in 100 mL Tris based lysis buffer (400 mM NaCl, 25 mM Tris pH 7.8, 20 mM β-mercaptoethanol and 10% (w/v) glycerol) supplemented to a final concentration of 25 mM imidazole, 2 mM $MgSO_4$, 0.1 mg/mL DNase I (Roche AG, Basel, Switzerland), 2x cOmplete EDTA-free protease inhibitor cocktail (Roche AG, Basel, Switzerland) and 0.1 mg/mL lysozyme (MedChem Express, Princeton, NJ, USA). The cells were thoroughly vortexed and lysed by sonication as described above. Thereafter, ATP (Thermo Fisher Scientific) was added to the cell suspension to a final concentration of 1mM and incubated for 30 min on ice, before precipitation of nucleic acids. After ultracentrifugation the supernatant was collected and filtered as described above.

IMAC was performed by loading the sample onto a buffer equilibrated Ni^{2+} column (HisTrap™ FF 5 mL, Cytiva, Washington D.C., USA) binding to negatively charged His-tagged protein. The flow through was

collected and the column washed with 15 CVs of the respective binding buffer A (400 mM NaCl, 25 mM Tris pH 7.8, 20 mM β-mercaptoethanol and 10% (w/v) glycerol). The protein was eluted by applying 5 CVs elution buffer A (400 mM NaCl, 25 mM Tris pH 7.8, 20 mM β-mercaptoethanol and 10% (w/v) glycerol) supplemented with stepwise increasing imidazole content from 35 mM, 50 mM, to 500 mM. Fractions containing the protein of interest were identified by SDS-PAGE and then pooled.

To reduce imidazole content, the sample was transferred into a 3.5K MWCO snakeskin membrane bag for dialysis and stirred overnight at 4°C in 2L of binding buffer A. Next, the protein solution was concentrated by centrifuging at 3500 g at 4°C using an 10K MWCO AMICON tube (Millipore, Burlington, MA, USA) and loaded onto a size exclusion chromatography (SEC) column using HiLoad 16/600 Superdex75 column (Cytiva, Washington D.C., USA) equilibrated in SEC buffer (400 mM NaCl, 25 mM Tris pH 7.8, 0.5 mM TCEP and 10% (w/v) glycerol). Sample validation was completed by SDS-PAGE and NanoDrop (Thermo Fisher Scientific, Darmstadt, Germany).

6.1.5. Protein purification of sGFP and sGFP-TLX-LBD

Protein expression of sGFP and sGFP-TLX-LBD followed the procedure described above, and protein purification was carried out using the same protocol for both proteins. After ultracentrifugation the sample was loaded onto a gravity affinity chromatography column containing 10 mL IMAC Sepharose™ 6 Fast Flow beads (GE Healthcare, Chicago, IL, USA) charged with 4 CV 0.1 M $NiSO_4$. Sepharose beads were equilibrated in 2 CVs binding buffer A (400 mM NaCl, 20 mM NaH_2PO_4 pH 7.8, 10% (m/v) glycerol and 1 mM TCEP) supplemented to a final concentration of 25 mM imidazole. Buffer equilibrated beads were transfer into the protein sample. The mix was incubated for 30 min on rotation before transferred back into the column where beads settled down before being washed with 5 CVs of binding buffer A while collecting the flow through for a second sample application to increase protein yield. Elution was performed using each 2 CVs of 50 mM, 100 mM, and 10 CVs of 300 mM imidazole supplemented elution buffer A. Protein content was estimated by measuring absorption at λ= 280 nm (NaonDrop, Thermo Fisher Scientific, Darmstadt, Germany) in reference to imidazole supplemented buffer A corresponding the to the elution steps. The collected protein fractions were validated by SDS-PAGE, collected and carefully concentrated by centrifuging at 3000 g at 4°C in 3 to 1 min steps using an 10K MWCO AMICON (Millipore, Burlington, MA, USA).

To reduce imidazole content, the sample was transferred into a 3.5K MWCO snakeskin membrane bag for dialysis, stirred for 6 h at 4°C in 2L of buffer A. To avoid protein precipitation at the membrane the sample was transferred into a FALCON tube for TEV protease cleavage. Therefore, TEV protease kindly provided by VM was added in a 1:10 ratio. The enzyme was added in two steps as precipitation was monitored for 4 h before the rest was added and the sample further incubated overnight at 4°C on rotation. Efficiency of TEV cleavage and fractions of eluted protein were validated by SDS-PAGE.

To separate cleaved and uncleaved protein, reverse IMAC was performed using a gravity affinity chromatography column containing 10 mL IMAC Sepharose™ 6 Fast Flow beads (GE Healthcare, Chicago, IL, USA) charged with 4 CV 0.1 M $NiSO_4$. The sepharose beads were equilibrated in 2 CVs binding buffer A, then transferred into the sample. The mix was incubated for 30 min on rotation before transferred back into the column, where the beads were allowed to settle. The column was washed with 4 CVs of binding buffer A while collecting the flow through. Uncleaved protein was eluted using 300 mM imidazole in elution buffer A. Protein content was estimated by measuring absorbance at λ= 280 nm (NaonDrop, Thermo Fisher Scientific, Darmstadt, Germany).

Prior to SEC using a HiLoad 16/600 Superdex75 column (Cytiva, Washington D.C., USA), the sample was filtered as described above. The eluted protein fractions were validated by SDS-PAGE and NanoDrop (Thermo Fisher Scientific, Darmstadt, Germany).

6.1.6. SDS-PAGE

For sample validation and evaluation of protein purification efficiency, SDS-PAGE was performed at multiple stages throughout the protein purification process. Samples were prepared by adding 4x Laemmli buffer (3% SDS, 10% glycerin, 5% β-mercaptoethanol, 62.5 mM Tris pH 6.8 and 0.1% bromphenolblue in ddH_2O), followed by denaturation at 95°C for 10 min using a Thermal Shake *lite* (VWR, Radnor, PA, USA). A volume of 10 -20 µL of each sample was loaded per well onto the gel containing an acrylamide gradient of 4 to 12% (SERVA, Heidelberg, Germany) to separate proteins in the range of 30 – 300 kDa. Gel electrophoresis was performed using a 1:10 diluted running buffer (1% SDS, 1.92 M glycine, 250 mM Tris pH 6.8 in ddH_2O) at 200V for 60 min using PerfectBlue™ power supply (VWR, Radnor, PA, USA).

6.1.7. HTRF assay

TLX-LBD homodimer formation and the effects of TLX modulators on dimerization was assessed using an HTRF assay. Biotinylated Avitag-TLX-LBD in complex with streptavidin-linked terbium cryptate (Tb-SA, Revvity, Waltham, MA, USA) served as the Förster resonance energy transfer (FRET) donor. The concentrations of Avitag-TLX-LBD and Tb-SA were kept constant at 0.5 nM and 1 nM, respectively. To achieve the clearest HTRF-signal, the FRET-acceptor concentration of sGFP-TLX-LBD was established by testing varying concentrations, as seen in ***Table 12***.

In assay 1 to 3, the maximum concentration of sGFP-TLX-LBD, as well as the dilution factors used to titrate down the FRET-acceptor, differed across the three experiments. Free sGFP was added accordingly to maintain the maximum concentration of either at 8 µM, 2 µM or 1 µM, depending on the experiments. The assay solutions were prepared in HTRF buffer supplemented with 1 mM KF, 1% (w/v)

CHAPS, 5% (w/v) glycerol and 1% DMSO (due to the addition of the test compounds or 1% DMSO alone as an apo control). TLX modulators **3**, **6**, **7**, **8**, **10**, **11** and **12** were included at final concentrations of 30 µM.

Table 12: *Overview of HTRF assay conditions.*

Assay	Avitag-TLX-LBD [nM]	Tb-SA [nM]	sGFP-TLX-LBD [µM]	sGFP [µM]	Compound [µM]	Dilution factor
1	0.5	1	1.95 – 8	8	30	0.5
2	0.5	1	0.0006 – 2	2	30	0.5
3	0.5	1	0.00047 – 1	1	30	0.6
4	0.5	1	0.1	0.1	0.19 – 250	0.6

To evaluate dose-dependent effects of the selected compound **7** on homodimerization, the FRET-donor conditions were kept constant, as described above. The FRET-acceptor concentration sGFP-TLX-LBD was kept constant at 100 nM, so no additional sGFP was added to the reaction mix. Compound **7,** dissolved in HTRF assay solution, was sonicated for approximately 4 min at 40 kHz and 35°C to ensure proper dissolution of the compound.

The final sample volume was set to 20 µL per well using a HiBase polysterene 384-well microplate (Greiner, Alphen aan den Rijn, NL). The plate was covered with adhesive aluminum foil to prevent evaporation and to protect from light exposure. Prior to HTRF signal measurement the samples were equilibrated at room temperature for 2 h. Fluorescence intensity (FI) was assessed using a TECAN Spark plate reader (TECAN Spark, Männedorf, Switzerland) at λ_{Em}= 520±10 nm (FRET-donor) and λ_{Em}= 620±10 nm (FRET-acceptor) after excitation of the FRET-donor at λ_{Ex}=320±20 nm. All measurements were performed in a filter-based setting employing 75 flashes, an integration time of 200 µs and a lag time of 100 µs at an optimal gain. The excitation bandwidth was set to 20 nm and the emission bandwidth to 10 nm and the Z-position was set to the well emitting the highest HTRF FI. The HTRF signal was calculated by dividing the measured donor fluorescence (FI at λ=520 nm) by the acceptor fluorescence (FI at λ=620 nm) multiplied by 10,000.

6.2. In vitro assays

6.2.1. Cell lines

Cell lines T98G, A549 and HEK293T cells were cultivated in T75 flasks in high glucoses DMEM supplemented with 10% fetal cow serum (FCS), penicillin (100 U/mL), streptomycin (100 µg/mL) and 1mM sodium pyruvate. ARPE19 cells were cultivated in DMEM/F12 (1:1) medium supplemented with 10% FCS, penicillin (100 U/ml) and streptomycin (100 µg/mL). All cell lines were incubated at 37°C and 5% (v/v) CO_2 and passaged at a confluence around 50- 75% twice a week up to a maximum of 20 (ARPE19)

or 30 (T98G, A549, HEK293T) passages. For passaging the medium was removed and cells were washed with 8 mL warm PBS before incubated in 4 mL trypsin/EDTA solution at 37°C and 5% (v/v) CO_2 for 2 min (HEK293T) or 5 min (T98G, ARPE19 and A549). To collect detached cells 8 mL of the respective growth medium was added to the cells which were then centrifuged at 300 g at room temperature for 5 min. After the supernatant was discarded cells were resuspended in fresh growth medium and added to a new T-75 flask (Sigma-Aldrich, St. Louis, MO, USA) containing 12 mL of fresh growth medium. Prior to seeding cell density was determined using counting chambers (Paul Marienfeld GmBH & Co. KG, Lauda-Königshofen, Germany).

6.2.2. Quantitative real-time polymerase chain reaction (qPCR)

To quantify TLX ligand derived effects on gene expression in ARPE19, HEK293T and T98G cell lines, 2.5 x 10^5 cells were seeded per well into a 12-well plate and incubated for 24 h at 37°C and 5% (v/v) CO_2. FCS concentration was reduced to 0.1% at least 24 h prior to treatment. Compounds were incubated for 8 h (HEK293T) or 16 h (ARPE-19 and T98G) before cells were washed in PBS, dried and stored at -80°C for subsequent RNA isolation. Experiments were performed in six biological independent replicates (n=6). For RNA isolation, cells were lysed and purified according to the manufacturer's protocol using E.Z.N.A. ® total RNA kit I (Omega Bio-Tek, Norcross, GA, USA), RNA quantity and purity were assessed by UV/VIS spectrophotometer (NanoDrop™, Thermo Fisher Scientific, Darmstadt, Germany) measurement at λ= 260 nm and λ= 280 nm. Prior to qPCR RNA was diluted in ddH_2O and linearized at 65° for 10 min and incubated on ice for 1 min.

Depending on the yield either 1 or 2 µg of RNA were used for cDNA synthesis using 100 U SuperScript® IV reverse transcriptase (Thermo Fisher Scientific, Darmstadt, Germany), 20 U recombinant RNasin® Ribonuclease inhibitor (Promega Corporation, Madison, WI, USA), 5x First Strand buffer, 0.1 M dithiothreitol (DTT, Thermo Fisher Scientific, Darmstadt, Germany), 3.75 ng linear acrylamide, 625 ng hexanucleotides (Merck, Darmstadt, Germany), 11.25 nmol deoxyribonucleoside triphosphate mix (dNTP, Thermo Fisher Scientific, Darmstadt, Germany) mix comprised of 2.8 nmol ATP, TTP, CTP and GTP, respectively. The final volume of the reaction mix was 22.45 µL. Reverse transcription was performed in two cycles set at 50°C for 10 min and 80°C for 10 min using Thermal Cycler XT^{96} (VWR, Radnor, PA, USA), respectively.

Next, qPCR samples were prepared in 96-well PCR plates (Eppendorf SE, Hamburg, Germany). Therefore, 8.64 µL of diluted cDNA sample (1:42) was added per well in addition to 6 pmol of the respective forward and reverse primer, 0.8 U of Taq DNA Polymerase (New England Biolabs, Ipswich, MA, USA), 40 ppm SYBR® Green I (Sigma Aldrich, Burlington, MA, USA) 15 nmol dNTP, 60 nmol $MgCl_2$ (Thermo Fisher Scientific, Darmstadt, Germany), 4 µg bovine serum albumin (Thermo Fisher Scientific, Darmstadt, Germany), 2 µL Taq buffer lacking detergents (Thermo Fisher Scientific, Darmstadt, Germany), 4µL BioStab PCR optimizer II (BiTop, Witten, Germany) and ddH_2O to a final reaction volume of 20 µL.

Quantitative real time PCR was performed using a qTower^3 G (Analytic Jena, Jena, Germany) set to 40 cycles of cDNA denaturation at 95°C for 10 sec, followed by primer annealing at the respective temperature listed in ***Table 13*** for 15 sec and elongation at 68°C for 20 sec. Human glyceraldehyde-3-phosphate dehydrogenase (hGAPDH) served as a house keeping gene and expression of human tailless like receptor (hTLX), human sirtuin1 (hSIRT1), human phosphatase and tensin homolog (hPTEN) and human tet methylcytosine dioxygenase (hTET3) were first normalized to hGAPDH (Δct) and in a second step each individual biological repeat was normalized to its vehicle control ($\Delta\Delta$ct).

Table 13: *Primer sequences used for qPCR of TLX target gene expression. All primers were purchased from Eurofins Genomics, Luxembourg city, Luxembourg.*

Gene	Forward primer	Reverse primer	Annealing temperature (°C)
hGAPDH	AGGTCGGAGTCAACGGATTT	TTCCCGTTCTCAGCCTTGAC	58,6
hTLX	CTAAGAGTGTGCCAGCCTTC	TGTTAGCATCAACCGGAATGG	57,2
hSIRT1	GGAGCAGATTAGTAAGCGGCTTG	GTTACTGCCACAGGAACTAGAGG	61,4
hPTEN	TGAGTTCCCTCAGCCGTTACC	GAGGTTTCCTCTGGTCCTGGT	64,1
hTET3	CCACAAGGACCAGCATAACCTC	CTCGCTACCAAACTCATCCGTG	62,5

6.2.3. Assessment of cell proliferation

To determine growth properties of ARPE19, T98G, A549 and HEK293T upon treatment with TLX modulators, 2.5x10^3 cells per well were seeded into 96-well plates (Greiner Bio-one, Kremsmünster, Austria) in growth medium supplemented with 10% FCS. Plates seeded with T98G and HEK293T cells were coated with 10 μg/mL collagen G diluted in phosphate buffered saline (PBS, 137 mM NaCl, 2.7 mM KCl, 10 mM Na_2HPO_4 and 1.8 mM KH_2PO_4 and ddH_2O, pH= 7.4) for 30 min at 37°C prior to seeding to improve cell adhesion. After 24 h, medium was removed, and the compounds were added to the cells in growth medium and 0.1% DMSO or 0.1% DMSO alone for maximum of 48 h. A range of seven concentrations was tested per compound. Compounds **1** and **2** were incubated at 0.3, 1, 3, 10, 30, 50 and 100 µM, compound 3 was incubated at 0.1, 1, 3, 10, 30, and 50 µM. Compounds **4** – **12** were incubated using at concentrations of 0.01, 0.1, 1, 3, 10, and 30 µM. Confluence was measured at t=0 h and continued in a 24 h interval using Spark Cyto plate reader (TECAN Spark, Männedorf, Switzerland). Confluence was expressed as a percentage of the total surface area and was normalized to 0.1% DMSO treated cells, with the data set as reference at t=0 h.

6.2.4. Cell viability assessment

Cell viability was assessed after 48 h compound stimulation in 0.1% DMSO or 0.1% DMSO alone as described in the previous chapter 3. To this end, the medium was aspirated and 100 μl/ well of a 1:10

diluted WST-8 tetrazolium salt solution ((2-(2-methoxy-4-nitrophenyl)-3-(4-nitrophenyl)-5-(2,4-disulfophenyl)-2H-tetrazolium, MedChemExpress, Princeton, NJ, USA) was added. Cells were incubated at 37°C and 5% (v/v) CO_2 for 2 h and colorimetric assessment of the reduced formazan dye was conducted at λ=450 nm using a Spark Cyto plate reader (TECAN Spark, Männedorf, Switzerland).

6.2.5. Quantification of cells by nucleic acid staining

For quantification of ARPE19, T98G, A549 and HEK293T cell number cells were incubated with 50 µL/well of the appropriate complete medium supplemented with HOECHST33342 dye (4µM final concentration, Abcam, Cambridge, UK) for 30 min at 37°C and 5% (v/v) CO_2. Fluorescence imaging was performed using Spark Cyto plate reader (TECAN Spark, Männedorf, Switzerland) by excitation at λ_{Ex}= 381 – 400 nm and detecting emission at λ_{Em}= 414 – 450 nm. Cell number was deduced by counting the number of HOECHST33342 stained nuclei using a previously set-up algorithm from TECAN (Image Analyzer™, TECAN Spark, Männedorf, Switzerland). The algorithm was set to a sensitivity of 70%, counting all objects the size of 8 – 30 µm in width and length.

6.2.6. Migration assay

Effects on migration were tested by seeding 1.8 x 10^5 T98G cells per well into 12-well plates, followed by overnight incubation. When cells reached confluence of at least 90%, serum concentration was reduced to 0.1% for at least 24 h prior to treatment. Cross-shaped scratches were introduced using 1 mL pipette tips. To remove cell debris, cells were washed with PBS before treatment with either 0.1% DMSO or compound supplemented medium. Cell migration was tracked via brightfield microscopy at time points 0 h, 3 h, 6 h, 21 h, and 48 h after treatment. The experiment was performed in three independent biological replicates (n=3), and analysis was carried out using ImageJ version 2.14.0/1.54f. The repopulated surface area at different time points was set in reference to t = 0 h.

6.3. Statistical analysis and curve fitting

Data analysis was performed in Microsoft Excel Version 16.87 (Microsoft, Redmond, WA, USA) and GraphPad Prism version 10.3.0 (Dotmatics, Boston, MA, USA). The number of independent biological repeats (n) is specified in each figure legend, and data is represented as mean ± standard deviation (SD), normalized to the reference as indicated. All graphs were created using GraphPad Prism version 10.3.0. Statistical analysis was completed also using GraphPad Prism version 10.3.0. The data were referenced to their respective DMSO control, and after confirming normal distribution and homoskedasticity ANOVA was used to investigate treatment effects (non-significant (n.s.) ≥ 0.1, * < 0.05, ** < 0.01,

*** < 0.001 and **** < 0.0001). HTRF signal data analysis was performed using GraphPad Prism version 10.3.0 by using non-linear regression with four parameter curve fit. Prior to dose-response analysis, X-values (concentrations) were transformed to their respective decadic logarithm.

7. Results

7.1. Biochemical characterization of TLX modulators

To elucidate TLX homodimerization properties and the effects of TLX modulators on interaction of two TLX-LBDs, a FRET-based HTRF assay was set up. Superfolder GFP fused to the TLX-LBD (sGFP-TLX-LBD) was selected as a FRET-acceptor and a biotinylated Avitag-TLX-LBD construct was chosen as FRET-donor in complex with a commercially available streptavidine tagged terbium cryptate. ***Figure 6*** shows the general workflow of protein expression and purification performed for Avi-TLX-LBD, sGFP and sGFP-TLX. The respective plasmids were transformed into *E. coli* and single colonies were selected for large scale protein expression. Cells were lysed enzymatically and by sonication as well as purified by ion metal affinity chromatography (IMAC) and size exclusion chromatography. In parallel, the process was constantly monitored by SDS-PAGE. In the end quantity and quality of the respective protein were validated by SDS-PAGE and NanoDrop.

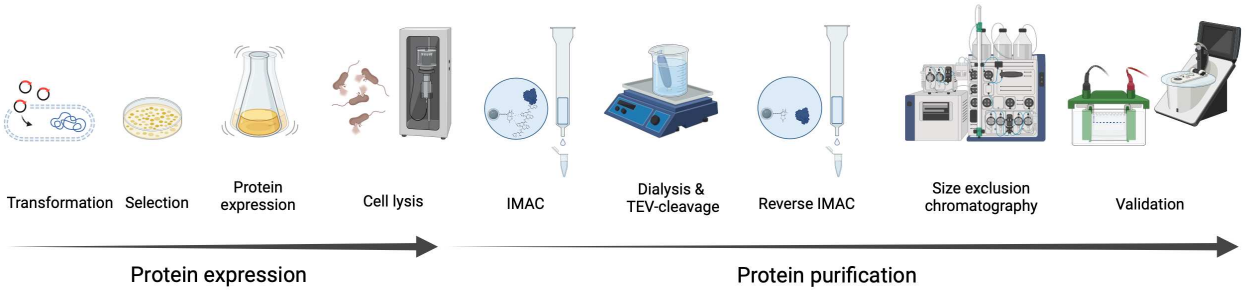

Figure 6: *Schematic overview of protein expression and purification workflow. This figure was created using BioRender.com.*

7.1.1. Purification of soluble FRET-donor Avitag-TLX-LBD

As described above, the Avitag-TLX-LBD construct was expressed in *E. coli* Rosetta™, initially yielding a low number of colonies. When co-expressed with bacterial biotin ligase BirA under selective pressure from three antibiotics (kanamycin, streptavidine and chloramphenicol), no colonies were obtained. By performing separate biotinylation and reducing the selective pressure to kanamycin alone, colonies were successfully grown and used to inoculate the preculture and main cultures. Protein expression was induced at OD_{600} of 1 with IPTG and cultivated for 18 h, yielding approximately 50 g bacterial pellet per 5 L of culture.

At this stage the protein of interest Avitag-TLX-LBD (73.5 kDa) carried a N-terminal histidine (His-) tag as well as a large MBP tag to enhance solubility. The molecular weight of the His and MBP-tag alone was calculated to be 45.3 kDa and the final protein of interest Avitag-TLX-LBD was calculated to be 28.2 kDa. To isolate the protein of interest avitag-TLX-LBD (73.5 kDa), IMAC was performed using a Ni^{2+}

charged column. Therefore, the sample was added to the column and the negatively charged histidine residues of the protein should bind to the positively charged Ni^{2+} resin of the column. Low concentration of imidazole in the buffer improves purity of the sample as it prevents unspecific binding to the resin. In the manner of a ligand-exchange chromatography, upon increasing the imidazole content, it supersedes the His-tagged protein due to its greater affinity, eluting the protein of interest. A considerable amount of unbound protein was observed in the flow through (SDS-PAGE, ***Figure 7A***, lane 2). Thick bands at 73.5 kDa in lanes 5-7 (***Figure 7A***) represented sample fractions of the eluted protein of interest, along with some impurities. Protein eluted at 100 to 300 mM imidazole was pooled based on the highest absorbance at λ= 280 nm (SDS-PAGE, ***Figure 7A***, lane 6), yielding 20.47 mg/mL of protein. The column's capacity (5 mL) appeared saturated, leading to some unbound protein in the flow-through. Dialysis overnight reduced the imidazole content from around 300 mM to approximately 10 mM.

To remove the MBP and His-tags, TEV protease digestion was performed overnight. TEV protease cleaved at the ENLYFQG sequence between the glutamine (Q) and glycine (G) residues, liberating the Avitag-TLX-LBD (28.2 kDa). The resulting 10.5 mg/mL of cleaved protein was biotinylated overnight with BirA, increasing its calculated molecular weight from 28.2 kDa to 28.4 kDa. A reverse IMAC (HisTrap™ FF 5 mL, Cytiva, Washington D.C., USA) was then used to separate cleaved from uncleaved protein. As the cleaved protein now lacked the His-tag, it did not bind the Ni^{2+} resin and appeared in the flow through. Due to the column's capacity being exceeded, the process was repeated using a gravity column with Ni^{2+} charged sepharose beads, doubling the column volume to 10 mL.

In the SDS-PAGE results (***Figure 7B***), the flow-through of the reverse IMAC/ gravity column (lane 2) still contained uncleaved protein (73.5 kDa), and cleaved protein (28.4 kDa). The proportion of uncleaved protein decreased in subsequent collected fractions of the protein sample of the flow through (***Figure 7B***, lanes 3 - 7). Eluted protein of fraction 3, with a volume of 23 mL and the highest absorbance (λ_{280}= 2.52), was selected for further purification using size-exclusion chromatography (SEC).

Attempts to concentrate the protein in buffer A caused rapid precipitation, leading to sample loss. To prevent further losses, other fractions containing cleaved protein as observed in SDS-PAGE were not utilized. SEC was employed to separate molecules based on size, with larger molecules eluting faster and appearing earlier on the chromatogram (UV-VIS at λ_{280}) compared to smaller molecules. Here, the aim was to remove the remaining uncleaved protein and MBP-tag to improve sample purity. Multiple rounds of SEC were performed to process the entire sample. A representative chromatogram is shown in ***Figure 7D,*** with the corresponding SDS-PAGE analysis as depicted in ***Figure 7C***.

The chromatogram revealed that uncleaved protein and MBP tag eluted first (***Figure 7D***, lane 1, protein fraction B8), peaking at a retention volume of about 45 mL. The second peak (***Figure 7D***, lane 2, protein fraction C2) contained the protein of interest, biotinylated Avitag-TLX-LBD (28.4 kDa), at a retention volume of 55.12 mL. The final fraction, eluted at 120 mL, showed no visible band in the SDS-PAGE, indicating negligible protein content. All fractions containing protein of interest were pooled and concentrated.

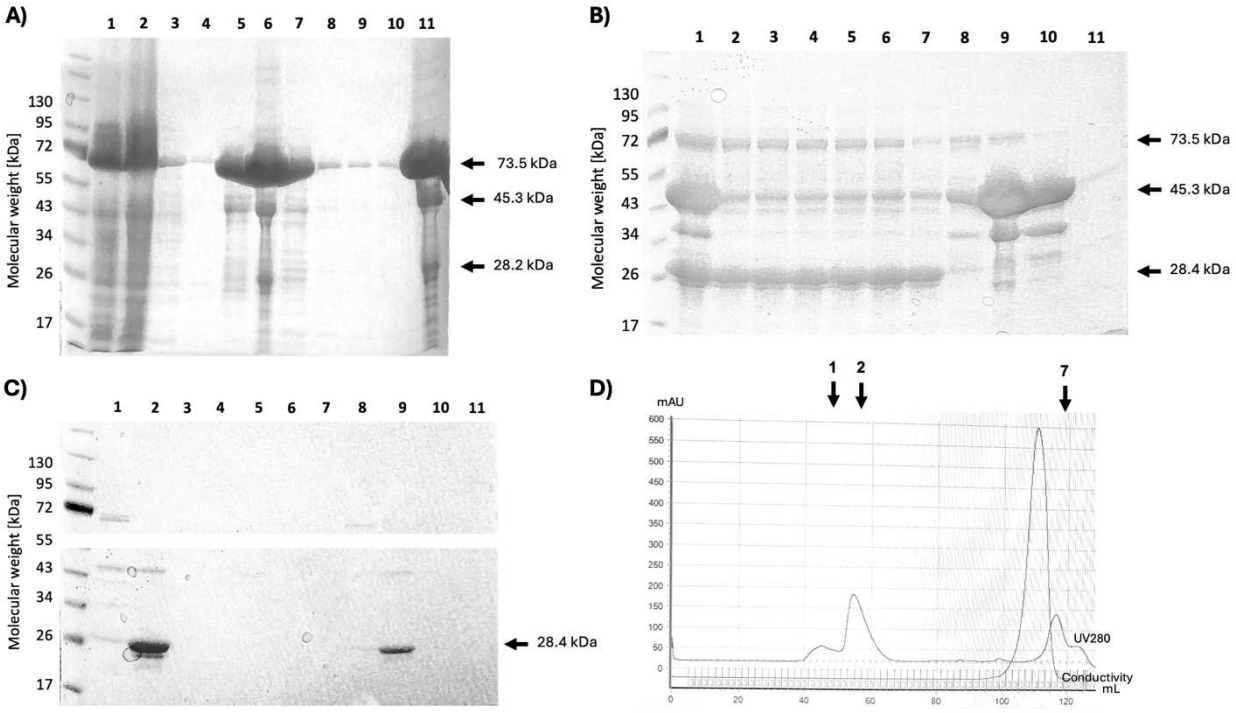

Figure 7: *Purification of Avitag-TLX-LBD.* ***A****) SDS-PAGE after IMAC and overnight dialysis. Lane 1: sample after ultracentrifugation, lane 2: flow through, lane 3: wash, lane 4: protein fraction 4 eluted at 30 mM imidazole, lane 5: protein fraction 7 eluted at 100 mM imidazole, lane 6: pooled protein fractions 8 to 11 eluted at 100 mM imidazole, lane 7: protein fraction 12 eluted at 100 mM imidazole, lane 8 to 10: protein eluted at 300 mM imidazole, lane 11: sample after dialysis.* ***B****) SDS-PAGE after reverse IMAC by gravity column. Lane 1: protein sample after biotinylation, lanes 2 to 7: collected flow-through fractions containing the Avitag-TLX-LBD protein, lanes 8 to 10: protein eluted at 100 mM imidazole, lane 11: protein eluted at 300 mM imidazole.* ***C****) SDS-PAGE after SEC in lane 1: eluted protein at a retention volume of about 45 mL, lane 2: eluted protein at a retention volume of 55.12 mL, lanes 3 to 11: eluted protein samples between a retention volume of 55 mL and 120 mL.* ***D****) Chromatogram from 1st round of SEC. Arrows and numbers are indicated respective to the numbers appointed to the lanes of the respective SDS-PAGE in C).*

To evaluate biotinylation efficiency, a streptavidin (STV) pull-down assay was performed, followed by SDS-PAGE analysis. Avitag-TLX-LBD samples were incubated with excess STV, and the resulting complexes were split into two groups: one boiled at 95°C for 10 min and the other one left in a native, unboiled state. In ***Figure 8A,*** unboiled streptavidine (lane 3), primarily appears as a tetramer (66 kDa), with a faint additional band at 90-95 kDa, potentially indicating a higher-order structure or aggregation. Boiled STV (lane 5) predominantly appeared as monomer (16.5 kDa), with the additional band at 90-95 kDa disappearing, as expected due to protein denaturation at high temperatures.

In lane 4 (***Figure 8***, unboiled STV + biotin + protein), the band at 90-95 kDa was significantly thicker compared to lane 3, suggesting the presence of bound Avitag-TLX-LBD. An Avitag-TLX-LBD monomer bound to an STV tetramer would have the calculated molecular weight of 94.4 kDa, while a dimer bound to an STV dimer would weigh 89.9 kDa. Although whether Avitag-TLX-LBD was bound as a monomer or dimer could not be conclusively determined. However, comparison of the Avitag-TLX-LBD (28.4 kDa) in an unboiled and boiled sample setting, it showed that most of the protein is present in a bound state, as the band is much thinner in lane 4.

To achieve an even higher purity a second round SEC was performed (***Figure 8B***). Biotinylated Avitag-TLX-LBD eluted at 54.9 mL, as seen in lane 1 representing the peak protein-fraction on the SDS-PAGE (***Figure 8A***). The shape of the peak indicated a monomer-dimer equilibrium. During SEC the protein was eluted in HTRF buffer, improving solubility compared buffer A, and the sample was successfully concentrated. The final volume was reduced gradually by careful concentration at low rotation and short time intervals. The sample was then shock-frozen in liquid nitrogen at a final concentration of 90.3 µM.

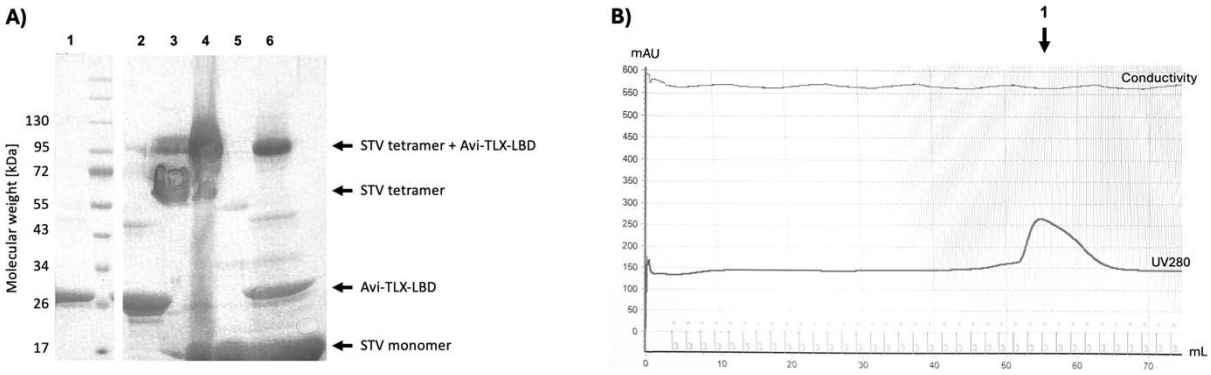

Figure 8: *Purification of Avitag-TLX-LBD and monitoring quality sample.* ***A****) SDS-PAGE after 2nd SEC run and streptavidine (STV) pull-down assay to assess biotinylation efficiency. Lane 1: Eluted protein fraction after the 2nd SEC run (chromatogram depicted in* ***B****) at a retention volume of 54.9 mL, lane 2: Sample after 1st SEC run used for streptavidine pull-down assay, lane 3: unboiled STV alone, lane 4: unboiled STV + biotinylated avitag-TLX-LBD, lane 5: boiled STV alone, lane 6: boiled STV + biotinylated avitag-TLX-LBD.* ***B****) Chromatogram after 2nd SEC run. The arrow indicates the lane number on the respective SDS-PAGE shown on the left.*

7.1.2. Purification of soluble sGFP and FRET-acceptor sGFP-TLX-LBD

Histidine tagged sGFP and the fusion protein sGFP-TLX-LBD were successfully expressed in *E. coli*, yielding high amounts of monomeric protein. The constructs were transformed successfully and colonies that were picked yielded large bacterial cell pellets, visibly neon green due to the expressed protein.

For the purification of sGFP, 36 g of bacterial cell pellet derived from 3 L expression medium was processed. Following cell lysis and ultracentrifugation, the sample was loaded onto a Ni^{2+} charged sepharose bead gravity for IMAC. The larger column volume (10 mL) improved binding efficiency, as no protein band at the expected construct size of 30.3 kDa was detectable in the flow through (***figure 9A,*** lane 2). The eluted protein fractions were collected and validated by SDS-PAGE before being pooled. The total yield at this point was 234.9 mg of protein. Dialysis and His-tag cleavage were performed in separate steps to avoid protein precipitation at the dialysis membrane, as conducted before with avitag-TLX-LBD. After cleavage the size of the construct was calculated to be 27.2 kDa. SDS-PAGE analysis revealed a poor TEV-protease efficiency (***Figure 9A***, lane 7), so the incubation time was increased to 30h in total to achieve a better yield. For reverse IMAC, the sample was applied to the column twice to achieve optimal separation of cleaved sGFP and uncleaved His-sGFP (***Figure 9B***, lane 2). During

avitag-TLX-LBD purification, concentrating the protein proved to be a risky step due to protein precipitation. To prevent losing the whole sample, it was split into two and concentrated separately. One sample was then concentrated further to test the limits of volume reduction. ***Figure 9B***, lane 3 shows the lower concentrated sample 1 (1.8 mg/mL) in a 1:20 dilution and lane 4 shows the higher concentrated sample 2 (3.6 mg/mL) in a 1:20 dilution. Both samples were then loaded separately onto the SEC. Lanes 5 to 9 of ***Figure 9B*** depict the SDS-PAGE analysis of the protein fractions collected after the first SEC. In total three runs of SEC were performed to process the whole sample. Right from the first SDS-PAGE analysis, a second band was detected slightly larger than sGFP which raised the question if a second reading frame of truncated sGFP is expressed as well. The same issue appeared for the expression of sGFP-TLX-LBD as well as the expression performed by a fellow student of sGFP-Nurr1-LBD. Later samples were further analyzed as described in the next chapter.

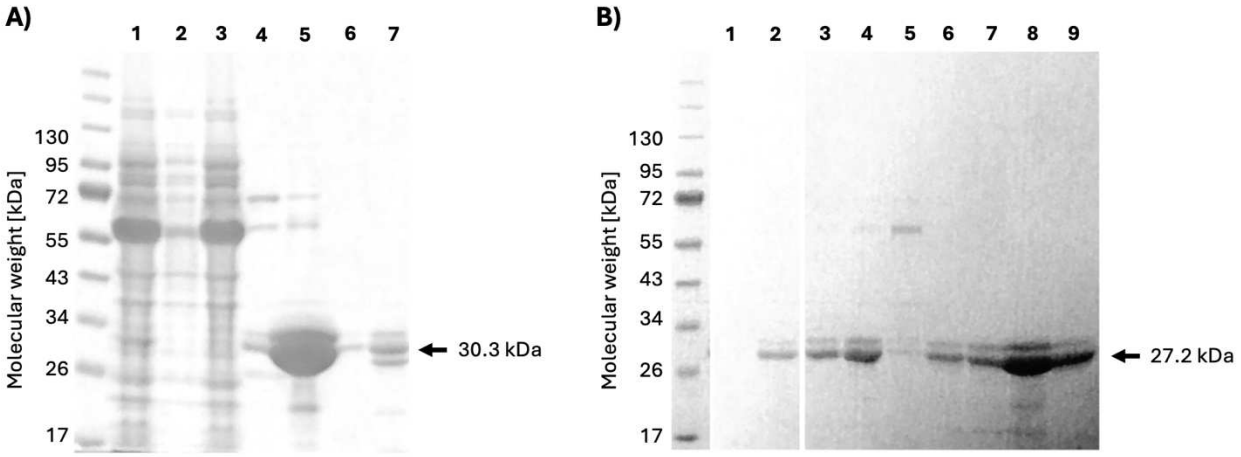

Figure 9: *SDS-PAGEs monitoring sGFP purification.* ***A****) SDS-PAGE after IMAC and TEV-cleavage. Lane 1: after ultracentrifugation, lane 2: flow through, lane 3: wash, lane 4: fraction 8 eluted at 50 mM imidazole, lane 5: fraction 10 eluted at 100 mM imidazole, lane 6: protein fraction 19 eluted at 300 mM imidazole, lane 7: protein sample after dialysis and 4 h of TEV protease incubation (1:20 dilution in ddH2O).* ***B****) SDS-PAGE after reverse IMAC and SEC. Lane 1: wash, lane 2: flow through, lane 3: concentrated sample 1 after rev. IMAC (1:20 dilution in ddH_2O), lane 4: concentrated sample 2 after rev. IMAC (1:20 dilution in ddH_2O), lanes 5 to 9: eluted protein samples after SEC at the protein peak measured at λ=280 nm. The size of His-tagged sGFP is 30.3 kDa and after cleavage the size is 27.2 kDa.*

In contrast to sGFP, the sGFP-TLX-LBD construct was expressed in *E. coli* strain BL21, otherwise protein expression was processed the same way. The yield was in equivalent to sGFP and 3 pellets of 3 L expression medium were used for purification. A Ni^{2+} affinity chromatography was performed to capture His-tagged protein. Eluted sample fractions containing highest protein content were pooled, namely fractions 3 (λ_{280}= 2.55) to 13 (λ_{280}= 1.13) before dialysis and subsequent incubation with a TEV-protease for 31 h in total. To monitor purification, an SDS-PAGE was performed (***Figure 10***) showing that not only the protein of interest sGFP-TLX-LBD at 57.7 kDa was eluted but also a larger protein of around 70 kDa as well as a construct of around 30 kDa. The size and bands visible in the gel are in accordance with the bands visible during sGFP purification as described above. During dialysis protein precipitation at the membrane was observed. Therefore, the sample was filtered and transferred into a tube to avoid further precipitation accumulating at the membrane. TEV-protease was added, and the sample was

monitored for precipitation. No further protein aggregation occurred and after 7 h more TEV-protease was added to the sample for another 24 h. Lane 10 and 11 of ***Figure 10*** show that after the prolonged TEV-cleavage the efficiency was still poor and only about half of the protein was successfully cleaved. As the yield was sufficient for the amounts necessary in future experiments, we proceeded to perform reverse IMAC and multiple rounds of SEC.

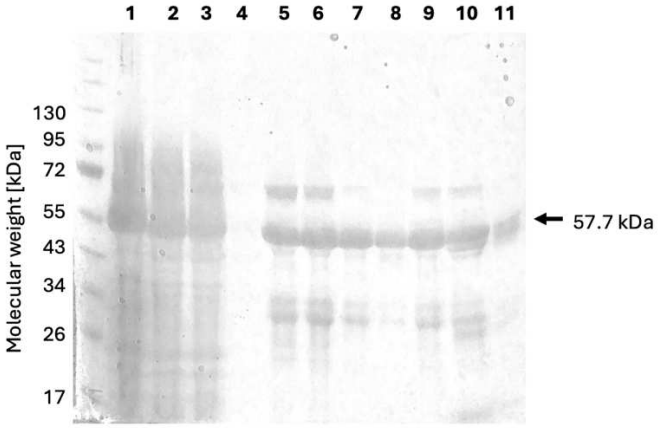

Figure 10: *SDS-PAGEs monitoring sGFP-TLX-LBD purification* until *after the first IMAC purification step.* ***A****) Lane 1: cell suspension after cell lysis, lane 2:* sample *after ultracentrifugation, lane 3: flow through, lane 4: wash, lane 5: IMAC, eluted protein fraction 3 at 100 mM imidazole, lane 6: protein fraction 4 at 100 mM imidazole, lane 7: fraction 8 at 100 mM imidazole, lane 8: fraction 12 at 100 mM* imidazole*, lane 9: pooled fractions 3 to 13 - sample* eluted at 100 mM imidazole*, lane 10: sample incubated with TEV-protease for 7 h and lane 11: sample incubated with TEV-protease for 31 h (1:10 dilution in ddH_2O).*

SDS-PAGE after the first size exclusion chromatography (***Figure 11A***) shows that the sample loaded onto the gel filtration column still contained uncleaved sGFP-TLX-LBD (57.7 kDa) as seen in the flow through of the reverse IMAC (lane 1) as well as in the tested fraction after the SEC (***Figure 11B***). The remaining sample that has not yet been processed by SEC, was therefore applied to a second round of reverse IMAC to get rid of uncleaved protein. The amount of uncleaved His-sGFP-TLX-LBD could be reduced, however not completely removed. When concentrating the protein before the next SEC, protein precipitation occurred which didn't allow to further reduce the sample volume. Instead, multiple rounds of consecutive SECs were performed to process the whole sample. Afterwards, the fractions were pooled, and the sample was carefully concentrated without any precipitation. The solubility of the protein was improved once diluted in HTRF buffer. The sample was loaded onto a second round of SEC (***Figure 11D,*** lane 1) to achieve greater purity. After analyzing the eluted fractions in an SDS-PAGE (***Figure 11C***) one fraction of clean sGFP-TLX-LBD and one fraction of semi-clean sGFP-TLX-LBD was collected and carefully concentrated. The clean sGFP-TLX-LBD protein did not precipitate, was stored at 53.2 µM and was used for subsequent HTRF experiments.

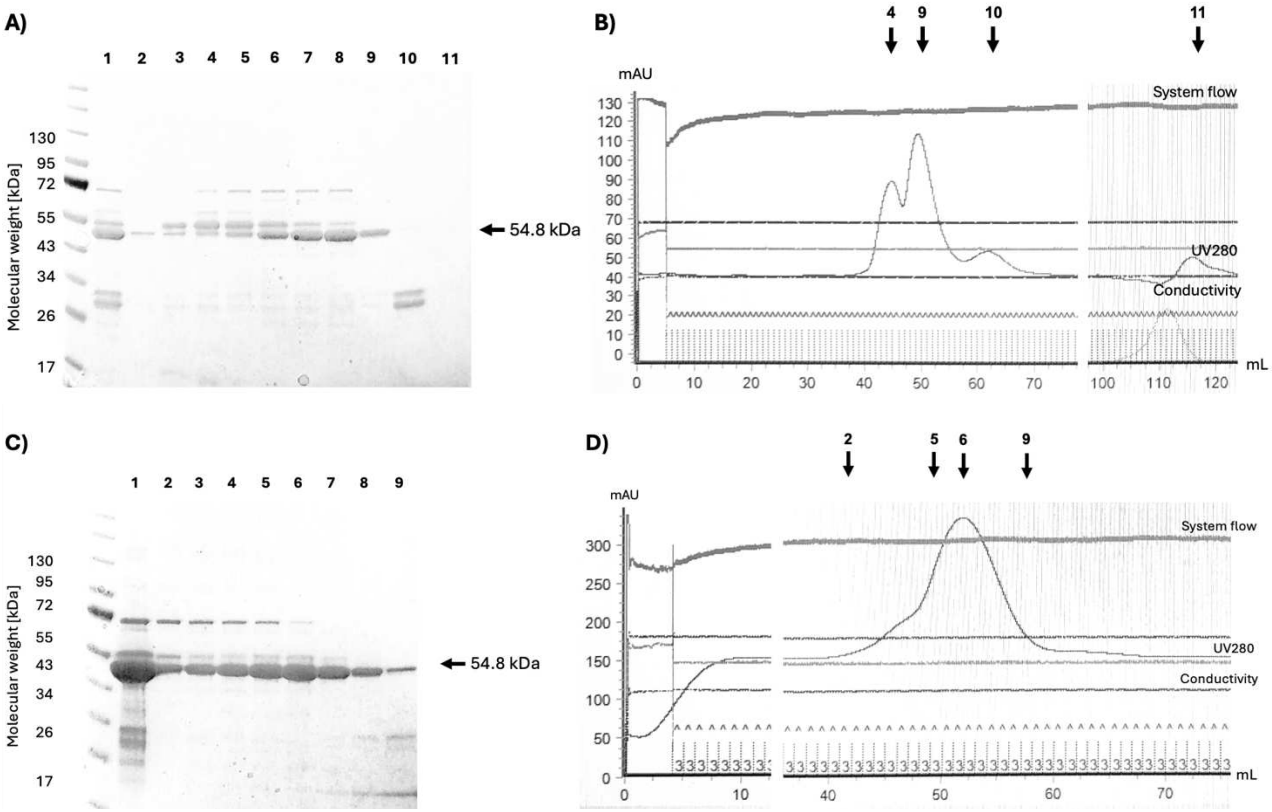

Figure 11: *Validation of sGFP-TLX-LBD purification steps by SDS-PAGE and depiction of the respective SEC chromatograms.* ***A****) After reverse IMAC and first SEC. Lane 1: flow through of reverse IMAC, lane 2: wash, lane 3: protein fraction of reverse IMAC eluted at 300 mM imidazole, lane 4: SEC protein fraction eluted at a retention volume of approximately 45 mL, lanes 5-9: protein eluted at the second protein peak at a retention volume of around 50 mL, lane 10: protein eluted at a retention volume of around 60 mL, lane 11: protein eluted at the last peak at a retention volume of around 115 mL.* ***B****) Chromatogram of the first SEC run. Numbers correspond to the lanes of SDS-PAGE depicted in (A).* ***C****) SDS-PAGE after the second SEC run. Lane 1: Sample loaded after first SEC run, lanes 2-9: eluted samples collected at the protein peak between approximately 45 mL and 60 mL of retention volume.* ***D****) Chromatogram of the second SEC run. Numbers above the arrows correspond to the lanes depicted on the SDS-PAGE on the left (****C****).*

7.1.3. Functional validation of the sGFP fluorophore

Due to the additional bands observed above the expected protein size in the SDS-PAGE during sGFP and sGFP-TLX-LBD purification, the sGFP sample was subjected to boiling at maximum temperature of 105°C for 15 min (***Figure 12A***, lane 2) and compared to an unboiled sample (lane 1). In case of impurities, we would have expected bands clearly distinguishable from those of the native state sGFP. If the sGFP construct encoded for a second, slightly larger sGFP variation we would have expected to see higher order dimers or tetramers according to the size of sGFP.

The native sample in lane 1 showed a band at the expected protein size of 27.2 kDa as well as a lighter additional band just above. Additional bands were visible between the band 43 and 55 kDa. Lane 2 showed a thick band at 27.2 kDa and one additional band slightly above that as seen in the previous

SDS-PAGE assessments. Seemingly, most of the present protein was sGFP at the correct size. The additional bands visible in the native state might be due to dimerization of the differently sized sGFP proteins. The SDS-PAGE analysis remained inconclusive about the additional band and whether it might derive from different folding or a different construct size. To investigate whether this additional construct might impact the functionality the sGFP fluorophore, a fluorescence intensity scan was performed. If the sGFP fluorophore was intact we would see no difference regarding their fluorescence, as the proteins were all tested at the same concentration.

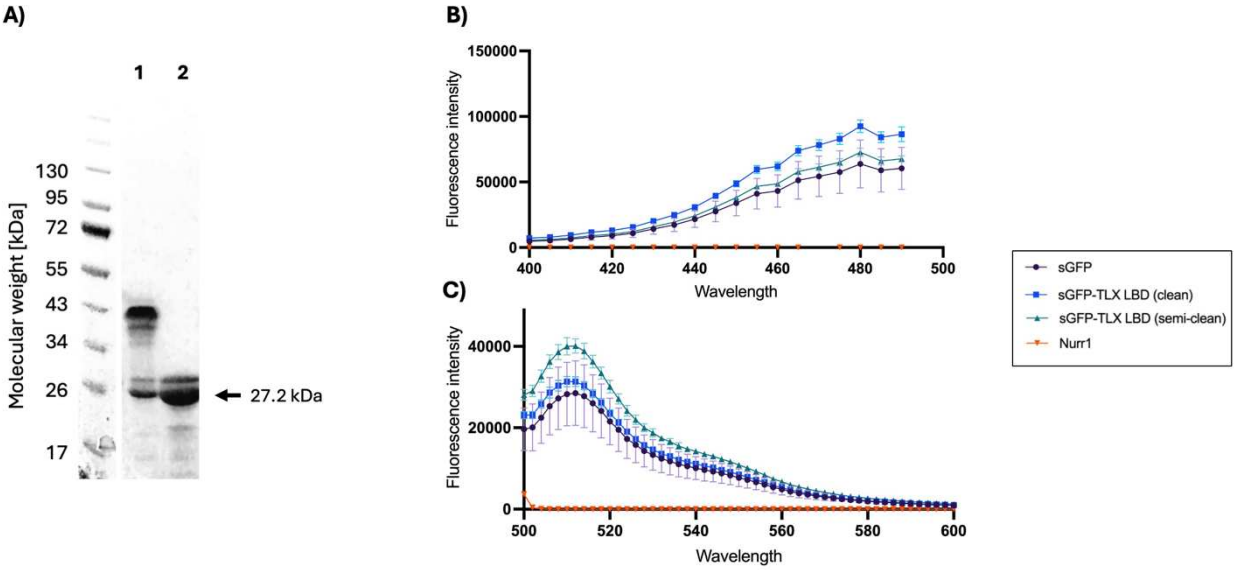

Figure 12: *SDS-PAGE of sGFP denaturation and fluorescence intensity scan of sGFP and sGFP-TLX-LBD.* ***A****) SDS-PAGE of sGFP. Lane 1: unboiled sGFP sample, lane 2: boiled sGFP sample.* ***B****) Excitation spectrum of sGFP (black), clean sGFP-TLX-LBD (blue), semi-clean sGFP-TLX-LBD (green) and negative control Nurr1-LBD (orange) between 400 and 490 nm measured at* λ_{Em}*=510.* ***C****) Emission spectrum between 500 and 600 nm of the same samples mentioned above after excitation at* λ_{Ex}*=485 nm. Data is indicated as mean ± standard deviation (SD).*

The semi-clean sGFP-TLX-LBD and the sGFP sample aligned quite nicely in their excitation (***Figure 12B***). However, the semi-clean sGFP fusion protein showed a slightly higher intensity in the emission spectrum when compared to the clean sample. This might be due to errors made during sample preparation affecting the concentrations. As this experiment was only conducted once to check fluorescent properties it was not repeated as the peaks were in line with the expected excitation and emission wavelengths of sGFP: λ_{Ex}= 485 nm and λ_{Em}= 510 nm. As a negative control Nurr1-LBD protein was used which lacks a fluorophore and wasn't expected to exhibit any fluorescent signal. Taken together, the expression and purification of the FRET-donor (biotinylated avitag-TLX-LBD), the FRET-acceptor molecule sGFP-TLX-LBD as well as sGFP yielded high amounts of clean protein sample. In addition, a fluorescence intensity scan as well as the STV pull-down assay validated the quality of the protein samples before further utilized in the HTRF assays.

7.1.4. Stabilization of the TLX-LBD: TLX-LBD homodimer by compound 7

As previously described TLX was suggested to act as a monomer as well as a dimer. To further investigate its binding characteristics an HTRF assay was selected to assess TLX homodimerization alone as well as in presence of TLX agonists. As agonists enhance TLX function, stabilization of TLX homodimers due to agonists binding was explored. After generating the fusion proteins necessary, HTRF assay conditions were established first to investigate baseline binding affinities of TLX-LBD homodimers incubated with a selection of compounds. Therefore, the inactive compound **3** as well as compounds **6**, **7**, **8**, **10**, **11** and **12** were selected to represent two distinct scaffolds. Compared to regular FRET assays the time delay between excitation and emission makes it a sensitive and robust assay to determine molecular interactions. Hereby, the FRET-donor, a streptavidine-terbium cryptate bound to biotinylated avitag-TLX-LBD, is excited at λ_{Ex}= 340 nm. The emitted wavelength can be detected at λ_{Em}= 620 nm. If proteins dimerize and are in proximity of at least 10 Å, the energy is transferred from donor to FRET-acceptor molecule sGFP which then emits light at λ_{Em}= 520 nm (***Figure 13A***). In total three different conditions were tested for compound effects on TLX: TLX homodimerization in comparison to 1% DMSO control. Assay conditions were established by testing different concentrations of FRET-acceptor molecule while the FRET-donor as well as the compound concentrations were kept constant. Achieving clear signals at 8 µM maximum concentration of the FRET-acceptor, we stepwise reduced its concentration to 2 µM and 1 µM to check for the minimum concentration needed to measure robust HTRF-signals. For each experiment the concentration of sGFP was kept constant at its maximum concentration to minimize variability of donor fluorescence and to facilitate quantitative interpretation.

The table in ***Figure 13B*** presents the individual K_d values as well as the mean K_d ± SD values established in two different conditions, namely condition A (2 µM maximal acceptor) or condition B (1 µM maximal acceptor). In the following, the results for compound **8** are not shown here as detected signals were very high and the calculated curve grew exponentially indicating protein aggregation which made the analysis of dimerization impossible. In both settings, compound **7** exhibited a shift of the binding curve towards greater homodimer stability compared to the apo homodimer incubated with the vehicle control. Homodimer binding affinity was determined within a low nanomolar range of K_d= 6.98 nM and K_d= 2.17 nM, both times approximately 7x higher than the DMSO control. The remaining compounds **10** to **12** (***Figure 13D***) showed no change regarding TLX homodimer formation in reference to the apo control. In contrast to condition A, in condition B, the detected HTRF signals did not provide a reliable dose-response curve, leaving the given K_d values invalid. No effects could be detected for inactive compound **3.**

As soon as the compound effects on TLX homodimerization at a single concentration (30 µM) were established, we focused on molecule **7**. Throughout all conditions compound **7** influenced dimerization by stabilizing the homodimer at a high affinity. Next, the aim was to establish a dose-response curve of the respective molecule to determine an EC_{50} value to TLX-homodimer formation (***Figure 13E).*** Therefore, at a constant concentration of FRET-donor and -acceptor, compound **7** was titrated down from the

maximal concentration of 250 µM down to 0.19 µM. Due to quenching at higher concentrations a dose-response relationship could not be established, and no EC_{50} was determined.

The results of preliminary biochemical assays indicated that at least one of the tested compounds, compound **7**, seemed to stabilize TLX homodimerization and therefore eventually also its biological function. For that reason, the compound selection was tested *in vitro* for its molecular and phenotypic consequences upon TLX modulation. In the following, the effects on target gene expression were analyzed as well as how TLX modulation influences cell proliferation as well as migration.

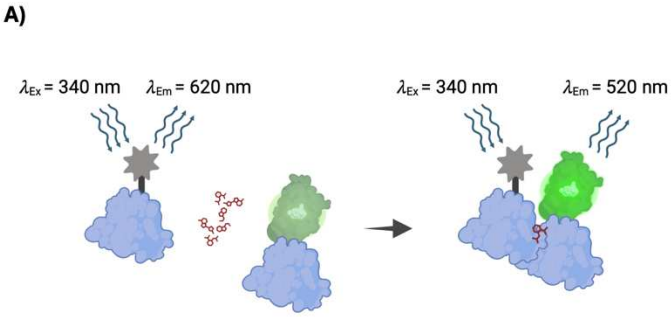

B)

Compound	K_d [nM] condition A	K_d [nM] condition B	K_d [nM±SD]
1% DMSO	47.65	15.63	31.64±22.64
3	147.50	55.93	101.72±64.75
6	58.67	0.84	5.00±5.88
7	6.98	2.17	4.57±3.40
10	5506	186.70	120.88±93,08
11	53.21	n.d.	53.21
12	66.53	100.40	83.47±23.95

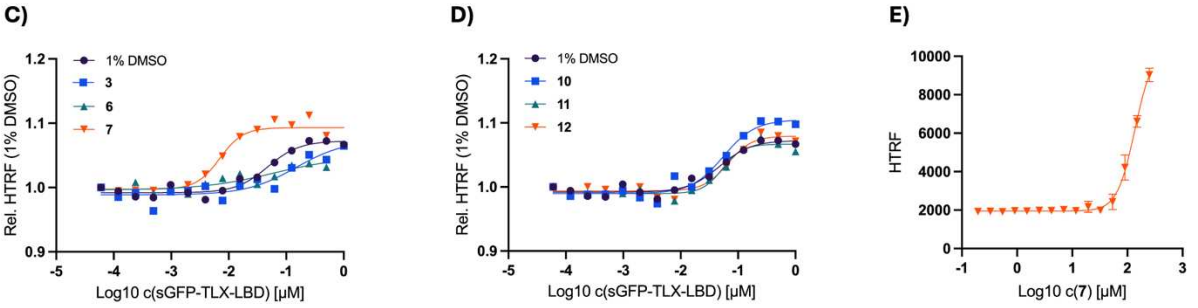

Figure 13: *Homogenous time-resolved FRET homodimerization assay (HTRF).* ***A****) Schematic depiction of HTRF homodimerization assay. TLX-LBD is highlighted in blue and sGFP in green. The Tb-SA is depicted as a grey star and compounds in red. Excitation and emission wavelengths are indicated above the arrows.* ***B****)* The table p*resents the calculated K_d values, as well as the mean ± SD. To determine effects on TLX-LBD: TLX-LBD homodimerization in solution with a selection of potential TLX modulators FRET-donor was kept constant (avitag-TLX-LBD: 0.5 nM, Tb-SA: 1 nM) as well as the respective compound concentration (30 µM). sGFP-TLX-LBD (FRET-acceptor) was added in varying concentrations: 2 µM* (condition A) *or 1 µM* (condition B) *as highest concentration. Free sGFP was added accordingly to keep the total acceptor concentration constant. HTRF signal was calculated from the fluorescence intensity measurements at λ_{Em}= 620 nm (FRET-donor) and λ_{Em}= 520 nm (FRET-acceptor).* ***C****) Shows the effects of compound set* ***10****-****12*** *in comparison to the vehicle control whereas* ***D****) represents the effects of compound set* ***3****,* ***6*** *&* ***7*** *in comparison to the vehicle control.* ***E****) Compound* ***7*** *was selected for further evaluation on its effects on TLX-LBD: TLX-LBD homodimerization. Therefore, concentrations of the FRET-donor (see above), FRET-acceptor (100 nM) were kept constant and compound* ***7*** *was titrated starting at a maximum concentration of 250 µM applying a serial dilution factor of 0.6. The experiment was performed in four independent repeats (n=4) as technical triplicates. The data is presented as mean ± SD of the independent repeats.*

7.2. TLX target gene expression analysis

Previous research by Faudone et al. identified **1** as a TLX agonist. Functional cellular assays demonstrated that in T98G glioblastoma cells **1** was able to significantly reduce cell proliferation and migration. Additionally, changes in target gene expression were quantified by measuring mRNA expression levels in glioblastoma cells upon treatment. Upregulation of SIRT1 and downregulation of PTEN and TET3 were observed. SIRT1 has been associated with protective effects against neurogenerative diseases [101]. The DNA-modifying enzyme TET3 plays a role in various cellular functions by oxidizing 5-methylcytosine (5mC) to 5-hydroxymethylcytosine (5hmC). Removal of DNA methylation is linked to self-renewal capabilities of embryonic stem cells, while diversification of DNA methylation patterns is observed during cell differentiation [102, 103]. PTEN reduces the second messenger phosphatidylinositol-3, 4, 5-phosphate (PIP3) and protein kinase B (AKT), which are directly involved in cell growth, survival, and proliferation [104].

In addition to the T98G glioblastoma cell line, TLX-expressing cell lines ARPE19 and HEK293T were included for orthogonal assessment. Testing the molecular effects of TLX modulation in multiple cell lines enhances robustness, reduces the risk of false negatives or positives, and broadens biological relevance by incorporating cells with diverse genetic backgrounds. In the following analysis of target gene expression, we investigated whether the given set of TLX agonists, including the established compounds **1** and **2**, modulated gene expression across different cell lines.

Therefore, T98G, HEK293T, and ARPE19 cells were each seeded into 12-well plates and incubated with the respective compounds at one or two concentrations (see ***Figure 14***) around their established EC_{90} value. The EC_{90} was selected to induce gene expression at levels sufficient for detection via qPCR. The incubation time was adjusted to the individual cell line's proliferation rate, lasting either 8 h (HEK293T) or 16 h (ARPE19 and T98G). After incubation, cells were harvested, and RNA was isolated and purified for cDNA synthesis. Messenger RNA (mRNA) levels were quantified by qPCR in relative to the housekeeping gene GAPDH and 0.1% DMSO-treated cells. An overview of results is provided in ***Figure 14***.

In T98G cells (***Figure 14A***), compound **1** did not exhibit any substantial effects on TLX target genes. However, a slight increase of TET3 (1.51±0.26) and SIRT1 (1.41±0.18) expression was measured, where we would have expected a decrease of TET3 mRNA levels. The same trend could be described for compounds **2**, **3** and **4**, though only compound **4** exhibited a small, but significant effect on TET3 (1.80±0.55, *, $p<0.05$) and SIRT1 (1.80±0.96, *, $p<0.05$) in an ordinary Two-way ANOVA analysis. Interestingly, at the higher concentration compound **8** seemed to show significant effects on TLX expression itself (3.63±0.74, ****, $p<0.0001$) and SIRT1 (2.08±0.34, ***, $p<0.001$). An increase, however, not significant was also observed for PTEN (1.61±0.6) and TET3 (1.56±0.38). Compounds **9** to **12** showed no significant changes in gene expression upon treatment. Only compound **11** exhibited slight inhibition on PTEN levels (0.85±0.28), a small increase of TET3 (1.49±0.46) and SIRT1 levels (1.48±0.29) as well as on TLX itself (1.34±0.71).

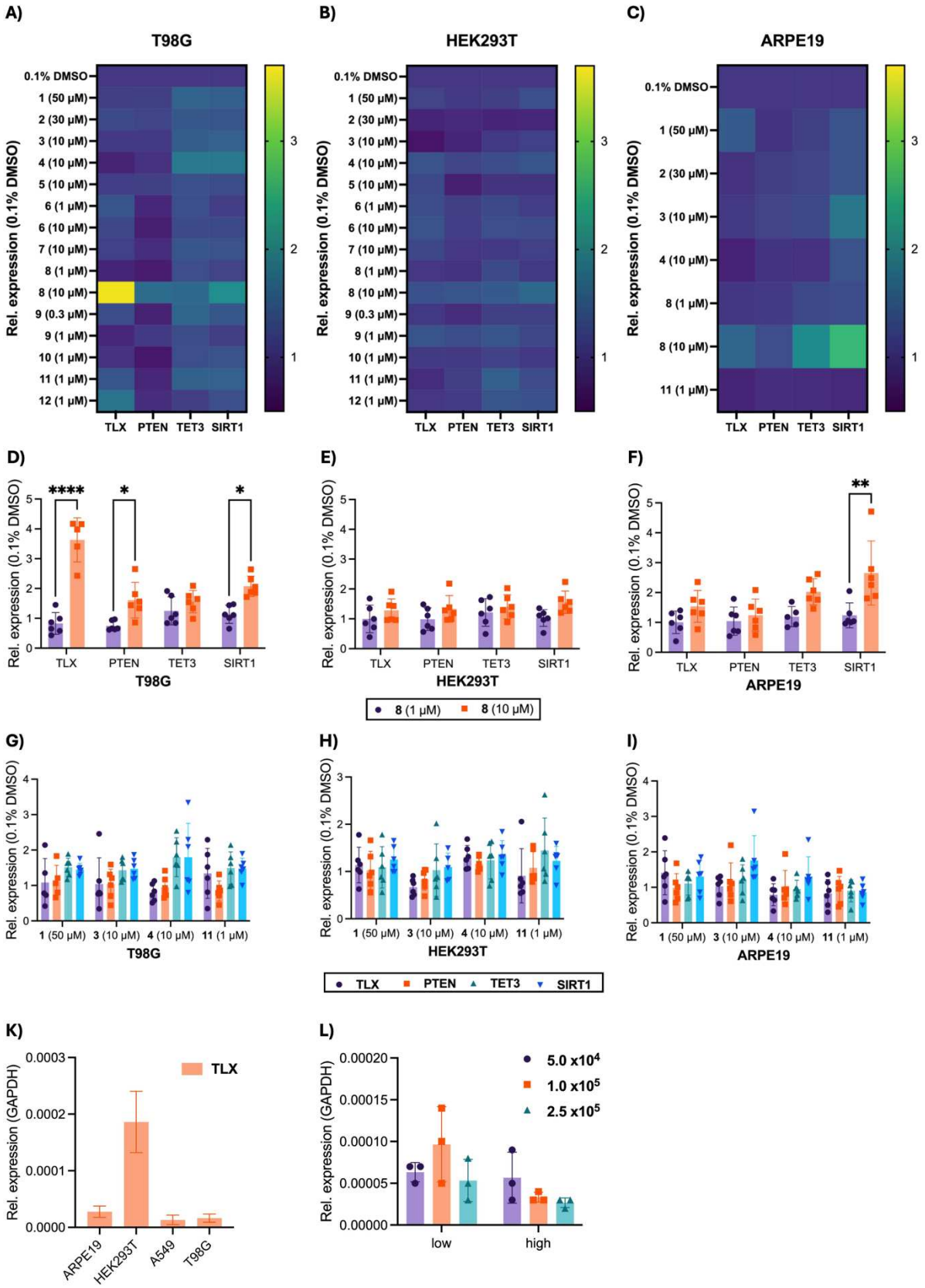

Figure 14: *Gene expression analysis.* ***A****) TLX and target gene expression relative to GAPDH and DMSO 0.1% (ΔΔct) in T98G. The mean of relative expression (ΔΔct) of human TLX and its target genes PTEN, TET3 and SIRT1 were assessed at 16 h* ***B****) HEK293T at 8 h and* ***C****) ARPE19 cells at 16 h following compound incubation (n=6). Statistically significant effects are highlighted in the text.* ***D****) to* ***F****) Effects of*

*compound **8** at 1 µM or 10 µM in all three cell lines. **G**) – **I**) presents the relative mRNA expression levels of TLX, PTEN, TET3 and SIRT1 after cells were treated with 50 µM **1**, 10 µM **3**, 10 µM **4** and 1 µM **11** in all three cell lines. Data is indicated as mean ± standard deviation (SD). For statistical analysis an ordinary Two-way ANOVA was performed (n=6), non-significant (n.s.) < 0.1, * < 0.05, ** < 0.01, *** < 0.001 and **** < 0.0001. **K**) Baseline expression of TLX in multiple cell lines. Cell pellets were collected at different timepoints during cultivation (passages from 4 to 30), (n≥ 4). **L**) Evaluation of the effects of cell density on TLX expression in ARPE19 cells. Therefore, cells were seeded from either high density (confluence of approx. 80%) or low density (confluence approx. 20%) cultures. Either 0,5 x10^5, 1 x10^5 or 2,5 x10^{5}cells per well were seeded into a 12-well plate. Data is indicated as mean ± SD.*

The observed results in T98G cells did not align with previously published findings or with the expected changes in gene expression. Specifically, the upregulation of TET3, rather than its expected downregulation, and changes in TLX expression itself were unexpected. No opposing effects were detected for the inverse agonist **2**. In parallel, results of baseline TLX expression levels in different cell lines (***Figure 14K***) showed that HEK293T cells exhibited the highest levels of TLX, followed by ARPE19 and T98G. Additionally, A549 cells, which expressed low levels of TLX, were used as a negative control in later experiments. Based on these findings, the same experiment was performed in HEK293T cells, with a reduced induction time due to their higher cell proliferation rate.

No significant changes of TLX target gene expression were detectable in HEK293T cells, regardless of the tool compound used (***Figure 14B***). Only a similar trend for compounds **4** and **8** can be observed where TLX, TET3 and SIRT1 are slightly upregulated compared to the 0.1% DMSO control. As the analysis of the baseline expression level showed considerably higher TLX levels compared to T98G, we would have expected clear changes upon treatment. Second in line, ARPE19 cells expressed TLX at higher levels than T98G. As retinal epithelial cells in which TLX is endogenously expressed, ARPE19 cells may provide a more physiological model to investigate TLX mediated changes in gene expression. Due to time reasons the compound selection was reduced to compounds **1** and **2**, the inactive compound **3** as well as compounds **4**, **8** and **11** representing the distinct chemotypes. The selection was made considering the results derived from T98G and HEK293T cells.

ARPE19 (***Figure 14C)*** cells that were treated with compound **1** showed a slight increase of TLX expression itself (1.41±0.62) and SIRT1 levels (1.31±0.46). Interestingly, treatment with compound **3** (1.76±0.7, *, p<0.05) showed a moderate, but significant increase of SIRT1 expression. Again, compound **8** (10 µM) seemed to slightly induce TLX expression (1.54±0.53) and significantly upregulated TET3 (2.04±0.44, ***, p<0.001) and SIRT1 (2.66±1.07, ***, p<0.001).

Figures 14D-F presents the same data as shown in ***Figure 14A-C*** in more detail as it highlights single data points and statistical significance derived from a Two-way ANOVA analysis. Also, the effects of compounds **1**, **3**, **4** and **11** on all three cell lines are emphasized in more detail in ***Figure 14G-I***.

Overall, at 10 µM compound **8** appeared to have the greatest impact on gene expression, as significant changes were observed in T98G as well as ARPE19 cells. Interestingly, in T98G cells TLX expression itself was significantly upregulated at a higher concentration. Also, TLX was slightly upregulated by compound **1, 6** and **12**, which either indicates that changes may not be TLX specific or that the modulators

could exhibit their effects by binding to molecules involved in TLX regulation. As results did not align with previously published findings that were generated in T98G cells, we were wondering if differing cultivation conditions could cause intrinsic variation due to subordinate changes in expression of molecules involved in cell cycling signaling.

Reportedly, in eukaryotic cells cell density can be sensed by different mechanisms including negative feedback loops or signaling by second messengers which then induce inhibition of proliferation. Some second messengers, like cyclic adenosine monophosphate (cAMP), affect a plethora of cellular signaling pathways. As TLX is considered a regulator of proliferation maintaining a steady undifferentiated, proliferative state it can be worth investigating if cell density and changes in signaling also affect TLX.

In a preliminary experiment, endogenous TLX expressing ARPE19 cells were cultured over three passages at varying densities: high density (80-90% confluence) and low density (20% confluence). After the second passage, cells were seeded into a 12-well plate at different densities by adjusting the cell number per well. TLX expression levels were quantified by qPCR. First results showed that when cells derived from low-density cultures and were seeded at medium density ($1x10^5$ cells/well), TLX expression levels were three times higher (rel. mRNA expression: 0.00009±0.00005) compared to cells seeded from highly confluent cultures (rel. mRNA expression of 0.00003±0.000006) as shown in ***Figure 14L***. However, when seeded at low densities ($1.0x10^5$ cells/well), TLX expression was nearly identical in both conditions. At high density ($5.0x10^4$ cells/well), TLX expression was twice as high in cells derived from low-density cultures (rel. mRNA expression of 0.000053±0.00003) compared cells derived from high-density cultures (rel. mRNA expression of 0.000026±0.000006). These findings indicate that at medium cell densities, TLX expression varied depending on the population density of the culture from which the cells were originally seeded. This suggested that cell density might influence cell signaling pathways, leading to an upregulation of TLX expression. This could underscore TLX's role in proliferation and differentiation and hint at a regulatory feedback mechanism suppressing differentiation in densely populated environments. However, further experiments are required to gain deeper insights and draw stastistically robust conclusions.

Taken together, the analysis of TLX target gene expression following incubation with the set of TLX modulators did not reveal any clear TLX-specific effects. Although significant changes were detected, they were not consistent with expected outcomes. For instance, TLX agonists were expected to downregulate TET3 and PTEN while upregulating SIRT1; however, in T98G, the opposite effect was observed, with TET3 and PTEN expression levels often downregulated. Across all three cell lines, HEK293T showed no considerable changes in gene expression, despite exhibiting the highest baseline levels of TLX. As previously noted, the results in T98G cells did not align with published findings. Together with the fluctuating TLX expression profiles observed in ARPE19 cells under varying cultivation conditions, these results may have influenced TLX expression and, consequently, the outcome of the experiments.

Prior investigation of TLX-LBD homodimerization upon incubation with TLX agonist revealed that compound **7** seemed to stabilize TLX homodimerization. However, analysis of TLX target gene expression did not reveal any changes upon incubation with compound **7** specifically. Here, compound **8** of the same chemotype stood out the most. The biochemical assay did not provide any insight into dimerization properties as compound **8** led to protein aggregation when tested at 30 µM, three times higher than the maximum dose that was tested in vitro.

Beyond the biochemical and molecular assessment of TLX modulation, we also investigated its phenotypic effects in multiple cell lines following treatment. Recently published migration and proliferation data demonstrated that compound **1** reduced both processes in T98G glioblastoma cells. To broaden the analysis, TLX expressing ARPE19, T98G, HEK293T cells as well as the lung cancer cell line A549 were orthogonally incubated with the compound set. The effects of TLX modulation on migration, proliferation and metabolic activity were evaluated to identify common phenotypic changes.

7.3. Phenotyping TLX agonism

7.3.1. No changes in cellular migration upon treatment of T98G cells

As TLX has been linked to several cancers, most prominently glioblastoma, T98G cells were chosen to analyze effects of TLX modulation on cell migration. Cells were seeded into 12-well plates and upon reaching high cell density, cross-shaped scratches were added to each well. After the cell debris was washed away compounds were added at a single concentration (see ***Figure 15B***) according to their EC_{50} values as cells were treated for 48 h. The concentration of compound **1** was reduced from 30 µM to 10 µM as a preliminary experiment showed toxic effects at this concentration. At time point zero (t= 0 h), right after the addition of compounds, images were taken using brightfield microscopy. In the course of time, multiple pictures were taken at different time points focusing the center of the scratch. However, only t= 48 h was analyzed in reference to t= 0 h regarding changes of the scratched surface area representing cellular wound healing capacities. The baseline was set by the 0.1% DMSO control and as depicted in ***Figure 15***, no substantial cell migration into the scratched area has taken place. Only compound **2** showed a slight reduction in surface area and, consequently migration (0.94±0.03), compared to the control.

Interestingly, compound **3** resulted in an increase of the unpopulated area, which after 48 h extended beyond the initial scratch (1.26±0.07), likely due to cell death. As compound **3** is the inactive control within the tested TLX modulator set, these effects are most likely due to toxicity at the tested concentration (20 µM) rather than TLX-specific effects. After 48 h of treatment, none of the tested compounds substantially influenced cellular migration in the scratch wound assay.

This suggests that either TLX modulation did not affect cellular migration, or that T98G cells might not be the appropriate cell model for studying these effects. The latter is further supported by the target

gene expression analysis described in the previous chapter, where experiments in T98G cells yielded results that contradicted previously published data. Consequently, T98G cells were removed from the collection of cell lines that were used for further phenotypisation.

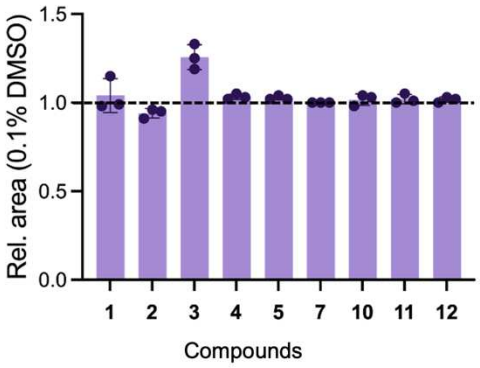

***Figure 15**: Scratch wound assay in T98G cells. 1.8x10^5 cells per well were seeded in a 12-well format in three biological independent replicates (n=3) and a single technical repeat. Cells were seeded in 10% FCS, 24 h prior to adding the scratch and compounds to each well the serum concentration was reduced to 0.1% FCS. Migration was tracked by brightfield microscopy and analyzed using ImageJ version 2.41.0/1.54f. Data is indicated as mean ± standard deviation (SD).*

7.3.2. Compounds 4 to 8 are tolerated up to 10 µM in multiple cell lines

To evaluate the impact of TLX modulators on cell growth, confluence was monitored over a set period of 48 h in presence or absence of the tool compounds. After excluding T98G, the remaining cell lines ARPE19 and HEK293T as well as A549 were selected for the following experiments. As shown by Faudone et al. (2021), treatment with TLX agonists was expected to reduce cell growth, whereas inverse agonism was considered to have the opposite effect. Therefore, cells were seeded into 96-well plates and cultivated in standard growth medium. Compounds were added to the cells covering seven concentrations between 0.01 and 100 µM depending on individual EC_{50} values. Upon treatment, confluence was measured immediately at time point zero (t= 0 h) and repeatedly at t= 24 h and t= 48 h. Results presented in ***Figure 16*** show the relative growth rate of one representative concentration per compound which was selected in accordance with previous experiments for better comparability of the in vitro experiments. At t= 0 h confluence was set at 1 and later time points changes in confluence were expressed as fold change relative to t= 0h.

Throughout all tested cell lines, compound **1** exhibited low to no significant changes at 50 µM (HEK293T: 4.29±0.95, *, $p < 0.05$) compared to the 0.1% DMSO control. In ARPE19 cells (3.28±0.81) almost no difference in cell growth was detectable relative to DMSO (3.68±0.44) at 50 µM or above. At a concentration of 100 µM compound **1** seemed to be toxic in both A549 (1.66±0.14, **, $p < 0.01$) as well as HEK293T (1.42±1.91, ****, $p < 0.0001$) cells as confluence was reduced by more than half after 48 h indicating cell death. Cells treated with **2** showed no significant alterations relative to the vehicle control at any of the tested concentrations. The same applied to the inactive compound **3** which did not reveal

any significant effects at the given concentration in all three cell lines. Only when **3** was incubated at 50 µM, cell growth was reduced by approximately half in HEK293T (2.13±0.93, ***, $p < 0.001$) and in ARPE19 (1.38±0.22, *, $p < 0.05$) cells most likely due to cell death. Interestingly, compound **6** seemed to induce cell growth at a low level in HEK293T cell but in no other cell lines that were tested. At 3 µM confluence slightly increased (7.20±1.15, *, $p < 0.05$), however decreased when treated with 10 µM (6.31±1.09) and 30 µM (6.60±0.77). Incubation with compounds **9** to **12** led to cell death in all three cell lines at much lower concentrations. Compounds **9**, **11** and **12** showed significant reduction of cell confluence when treated with 0.3 µM or 1 µM and above. Noteworthy, at 1 µM compound **10** seemed less toxic in A549 cells (3.48±0.39) and HEK293T cells (4.19±1.65) than in ARPE19 cells (1.45±0.21). However, at a higher concentration of 3 µM confluence was already reduced in A549 (1.99±0.19), in ARPE19 cells (1.12±0.10, *, $p < 0.05$) as well as HEK293T cells (3.11±2.59, *, $p < 0.05$).

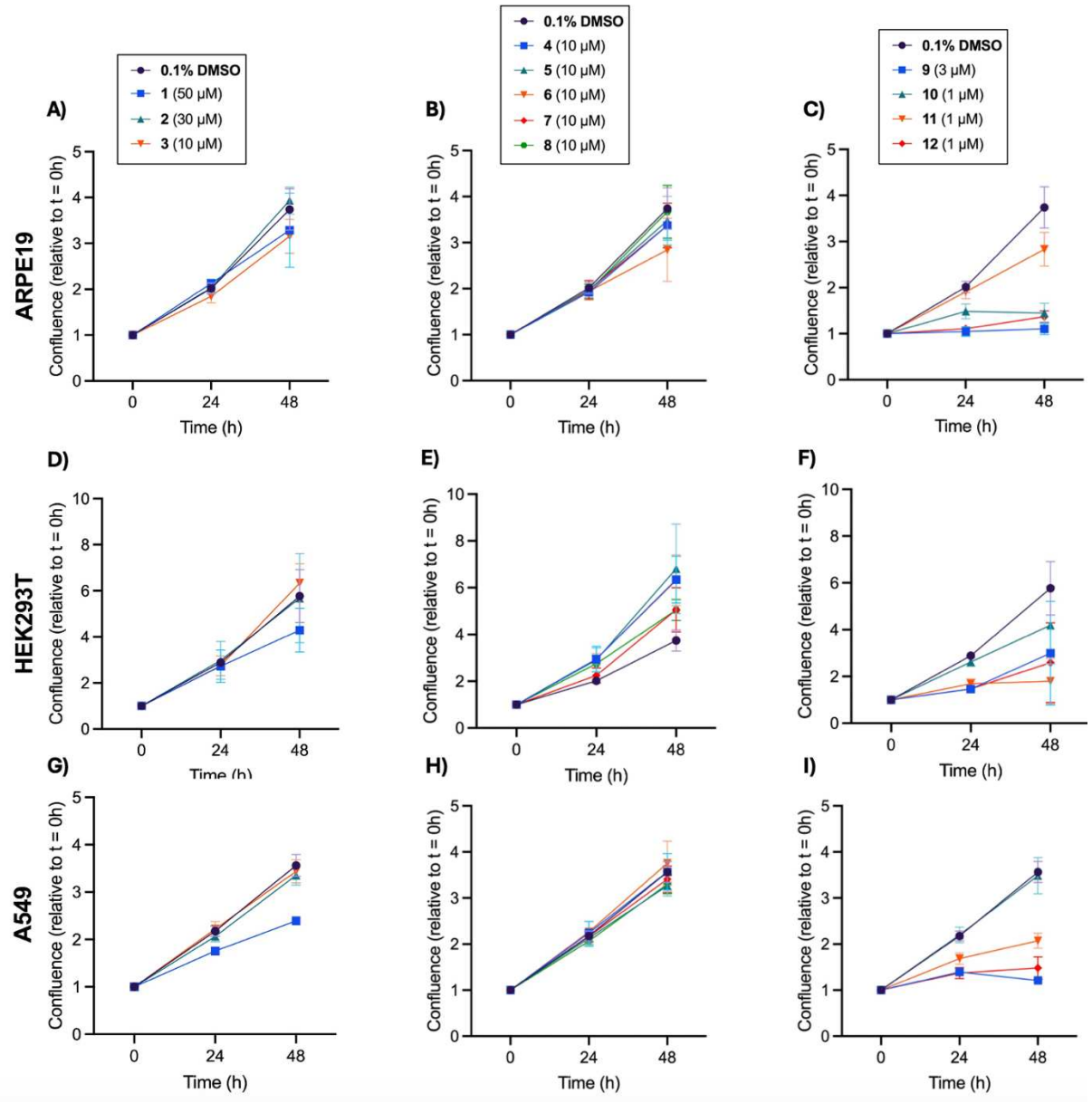

Figure 16: *Cell proliferation monitored by confluence measurements for 48 h in three different cell lines (ARPE19, HEK293T and A549). Cells were cultivated in 10% FCS supplemented medium and after*

approximately 24 h medium was changed and the respective compounds were added to the cells in seven different concentrations. Only one concentration is represented here. First measurement occurred at t= 0 h (TECAN Spark, Männedorf, Switzerland). Confluence data was normalized to t=0 h as fold of change relative to t= 0h. ***A)*** *to* ***C)*** *present relative cellular growth of ARPE19 cells during treatment.* ***D)*** *to* ***F)*** *show changes in confluence in HEK293T cells.* ***G)*** *to* ***I)*** *show cellular growth in A549 cells. Data is indicated as mean ± standard deviation (SD) (n=4).*

In the first set of compounds (**4** – **8**), no significant changes were observed as shown in ***Figure 16***. Significant effects were only detected at higher concentrations, likely due to cell death at the given concentrations. However, in all three cell lines concentrations up to 10 µM were well tolerated. In contrast, compounds **9** to **12**, with cell death occurring at much lower concentrations. This observation was further validated by brightfield microscopy, which showed a substantial number of detached cells.

Regardless of the differences when compared to the DMSO vehicle control, compounds **6** and **11** stood out due to the differences detected between the cell lines ARPE19 and A549. Here, a separate Two-way ANOVA analysis was performed comparing the effects of each compound throughout all tested concentrations (***Figure 17***). Treatment with compound **6** at 10 and 30 µM significantly reduced confluence in ARPE19 by approximately half compared to A549. Interestingly, compound **11** incubated at 1 µM, showed a significantly less reduced confluence in ARPE19 than A549 cells. However, concentrations above 1 µM seemed toxic in both cell lines equally. This could indicate a threshold where cell confluence was reduced in ARPE19 cells before reaching toxic concentrations.

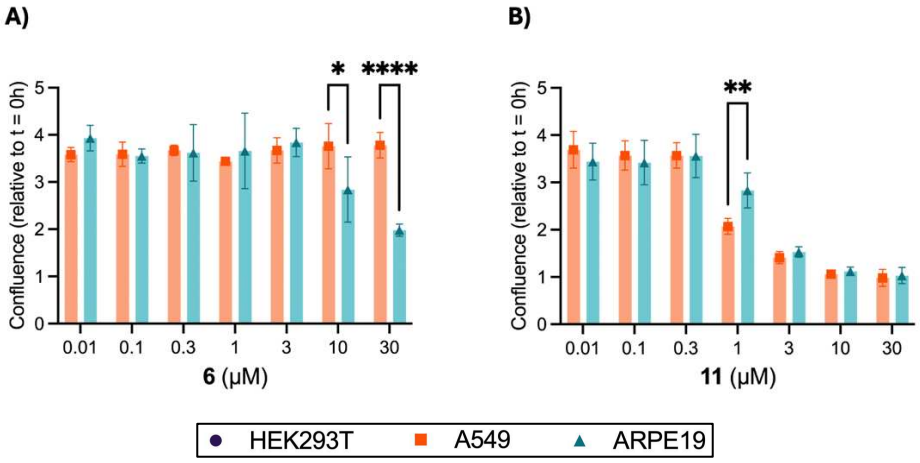

Figure 17: *Cell proliferation of compound* ***6*** *and* ***11*** *treated ARPE19 and A549 cells. Confluence data was normalized to t=0h.* ***A****) Represents compound* ***6*** *treated cells at different concentrations ranging from 0.01 to 30 µM. B) Represents compound* ***11*** *treated cells at different concentrations ranging from 0.01 to 30 µM Data is indicated as mean ± standard deviation (SD). For statistical analysis ordinary Two-way ANOVA was performed (n=4), non-significant (n.s.) < 0.1, * < 0.05, ** < 0.01, *** < 0.001 and **** < 0.0001.*

In summary, the analysis of cellular confluence revealed differences regarding two distinct chemotypes within the compound set, whereas compounds **4** to **8** were tolerated up to 10 µM and compounds **9** to **12** at 0.3 to 1 µM maximum. This could indicate off-target effects leading to cytotoxic effects. Differences between the two chemotypes might also derive from different binding properties which could only be evaluated by structural analysis. Compound **6** was the only molecule to significantly reduce cell growth

when compared to A549 cells. No opposite effects were identified for compound **2**, the inverse agonist. However, in the context of chemogenomics we would expect the same effects throughout the whole compound selection to assume a TLX mediated effect. As this is not the case, the measured effects cannot be attributed to TLX-specific modulation.

7.3.3. Assessment of cell viability in across ARPE19, HEK293T and A549

Beyond monitoring cell growth over time, cell viability was assessed orthogonally. Within the same experimental set up, a WST-8 assay was performed following the last confluence measurement at 48 h. Thereby, cellular dehydrogenases reduce WST-8 tetrazolium salts to formazan. The absorbance of formazan was measured at 460 nm and is proportional to the cell viability. The data was normalized to the respective DMSO null control (100%) and is represented in percentage. An ordinary Two-way ANOVA was performed to compare results in reference to A549. In the following we expected to see TLX mediated effects throughout ARPE19 and HEK293T cells, but not A549 cells. In ***Figure 18*** the complete compound set is presented in all tested concentrations across the three cell lines. Significant differences were only detected between HEK293T cells (90.86±7.78%) and ARPE19 cells (107.86±36.26%) when treated with 30 µM **1.** As both cell lines express TLX, these contradicting findings did not correspond with the expected outcome. For inverse agonist **2** significant variations between A549 and ARPE19 cells were mainly detected at higher concentrations (30 - 100 µM), however we would have expected opposite effects than observed for the 11 agonists. Compound **3**, which is inactive on TLX, showed significant differences in cell viability at lower concentrations (0.1-1 µM) as well as at the maximum tested concentration (50 µM). A decrease in viability across all three cell lines with increasing compound concentrations suggested toxic effects.

Precursor compound **4** showed significant differences when cells were treated at higher concentrations (1 - 30 µM). Most significantly were the distinction between A549 (112.34±8.99%) and ARPE19 cells (64.22±9.88%, ****, $p < 0.0001$) at 1 µM as well as at the highest concentration of 30 µM (A549: 103.3±4.84%, ARPE19: 39.38±6.39%, ****, $p < 0.0001$). However, no significant changes were detected in HEK293T cells. When cells were treated with 30 µM of compound **6** ARPE19 cell viability was significantly reduced (56.19±7.49%, ****, $p < 0.0001$) compared to A549 cells (103.31±3.24%). The only difference detected for compound **7** was a slight reduction of viability in ARPE19 cells (96.18±12.33%, **, $p < 0.01$) compared to A549 (109.77±7.31%). Compounds sharing the same molecule scaffold of a trifluoro benzene (**4** to **8**) seemed to have little significant influence on viability compared to A549 cells, except for compound **4**.

The other chemotype comprising compounds **9** to **12**, which interestingly showed almost no significant differences of ARPE19 and HEK293T cells when compared to the A459 cell line. Cell viability decreased throughout all three cell lines by approximately half when treated at higher concentrations. Here, compound **11** revealed no significant differences at 1 µM when compared to A549. Only precursor compound

9 revealed significant differences between A549 (58.38±3.80%) and ARPE19 cells (91.73±16.71%, ****, $p < 0.0001$) at 0.3 µM as well as at 3 µM (A549: 43.34±2.39%, HEK293T: 64.76±2.33%, **, $p < 0.01$).

According to the previous studies we would have expected to see a decrease in viability due to treatment with TLX agonists. However, in most cases the observed decrease in viability across all cell lines at higher concentrations likely reflects dose-dependent cytotoxic effects rather than TLX-specific activity, particularly for compound **9** - **12**. In contrast, within the other chemotype, compound **4** stood out, showing a significant decrease in viability at 1 µM and above.

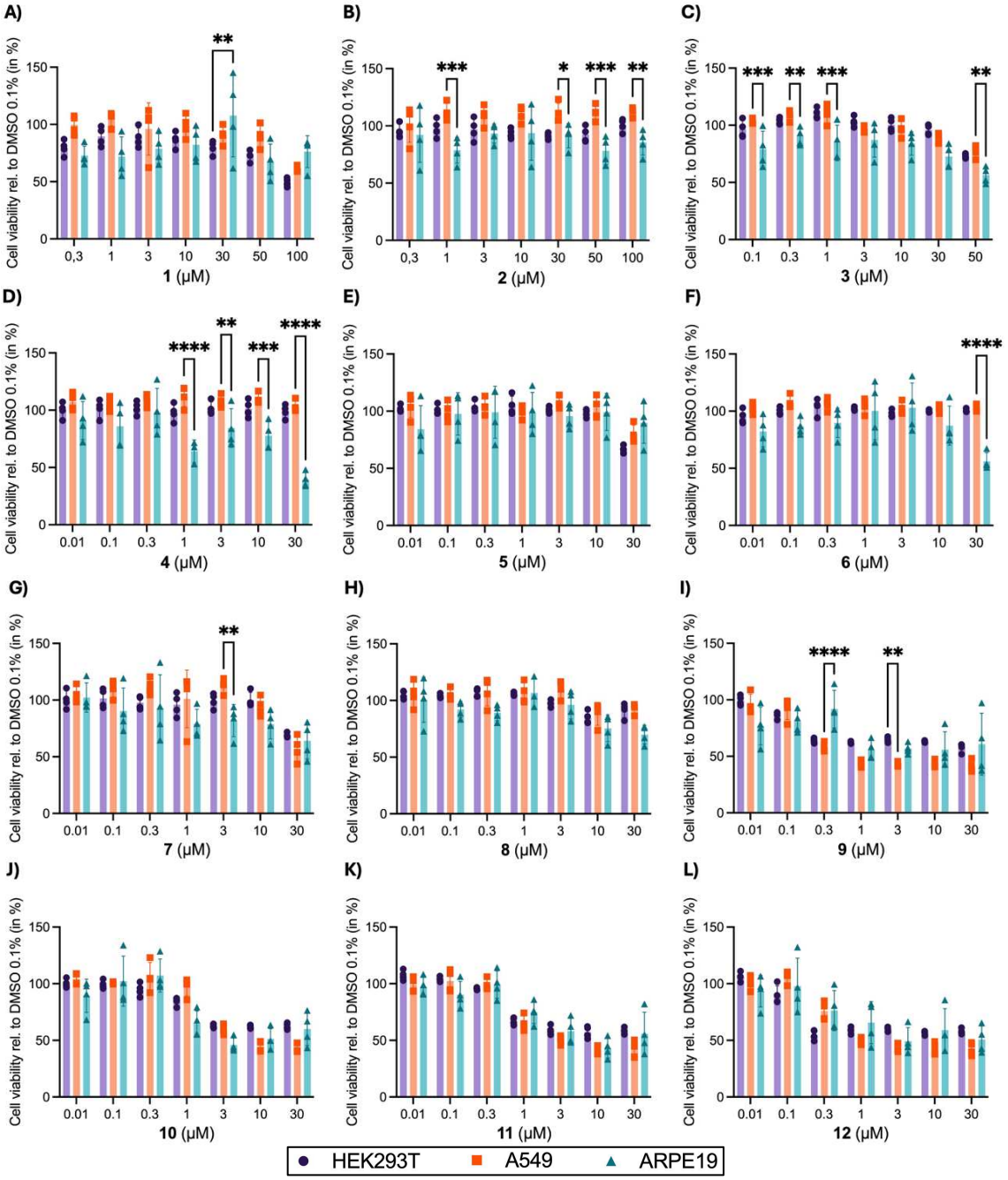

Figure 18: *Effects of TLX on cell viability in three different cell lines. Cells were cultivated in 10% FCS supplemented medium and after approximately 24 h medium was changed and the respective compounds were added to the cells in seven different concentrations. After 48 h the medium was removed*

*and 1:10 diluted WST-8 tetrazolium salt in 100 µL of 10% FCS supplemented medium was added per well. Plates were incubated for 2 h and absorbance at λ=450 nm was measured (TECAN Spark, Männedorf, Switzerland). The measured data was normalized to the DMSO 0.1% control, multiplied by 100. Data is indicated as mean ± standard deviation (SD). For statistical analysis ordinary Two-way ANOVA was performed (n=4), non-significant (n.s.) < 0.1, * < 0.05, ** < 0.01, *** < 0.001 and **** < 0.0001.*

After monitoring cell growth and viability, again the medium was replaced by fresh medium containing a HOECHST33342 nucleic acid stain allowing to count nuclei of living cells by detecting fluorescence at λ_{Em}= 414-450 nm after excitation (λ_{Ex}= 381-400 nm). Subsequently, the metabolic activity was calculated by dividing the normalized cell viability data (in %) by the normalized data derived from the nuclei staining (in %). The data was normalized to the respective 0.1% DMSO control within each biological replicate. This allowed the assessment of the metabolic activity of the remaining cells within each well. Values around 1 indicate that live cells remain at a steady metabolic activity. Values above 1 indicate that few remaining cells exhibit a higher metabolic turnover as less cells exhibit a higher viability, whereas values below 1 represent a lower metabolic rate as more cells exhibit a lower viability. The data is presented in ***Table 12*** and includes additional statistical evaluation by a Two-way ANOVA comparing the results from HEK293T and ARPE19 cells with the control cell line A549.

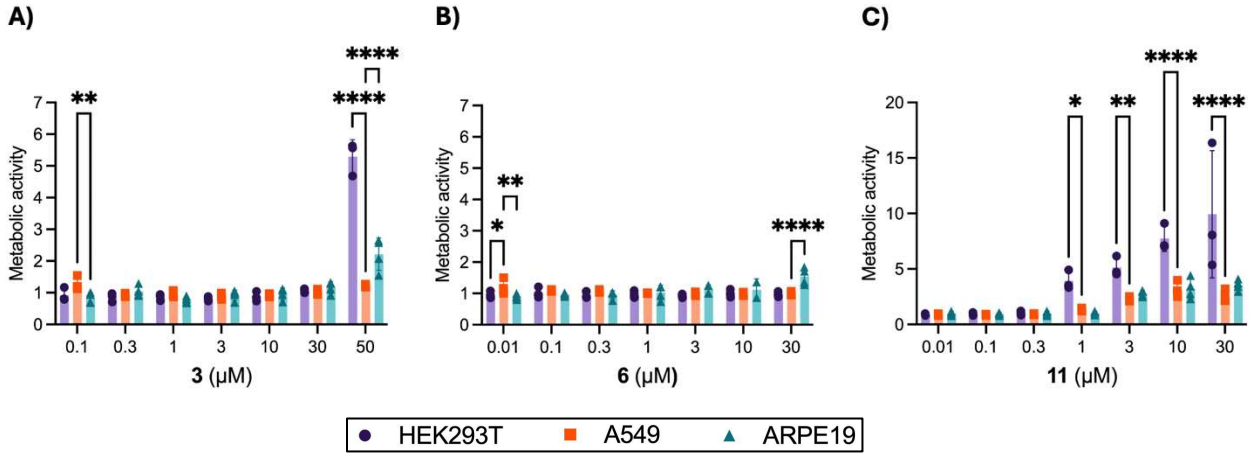

Figure 19: *Metabolic activity of compounds **3**, **6** and **11** in HEK293T, A549 and ARPE19 cells. Cells were cultivated in 10% FCS supplemented medium and after approximately 24 h medium was changed and the respective compounds were added to the cells in seven different concentrations. After 48 h the medium was removed, and a cell viability assay was performed. Subsequently, medium was removed and 4 µM hoechst33342 dye was added in 50 µL medium per well. The plates were incubated for 30 min before fluorescent imaging at λ_{Ex}= 381 – 400 nm and λ_{Em} = 414 – 450 nm (TECAN Spark, Männedorf, Switzerland). Data is indicated as mean ± standard deviation (SD). For statistical analysis ordinary Two-way ANOVA was performed (n=4), non-significant (n.s.) < 0.1, * < 0.05, ** < 0.01, *** < 0.001 and **** < 0.0001.*

Significant changes compared to A549 were detected primarily at higher concentrations. The high metabolic rate of HEK293T cells (94.32±27.05, ****, p < 0.0001) treated with **1** (100 µM) stood out immediately. Interestingly, compounds **9** to **12** showed a significant increase of metabolic rate along increasing concentration in both cell lines, but especially in HEK293T cells. Compared to A549 no significant differences were identified upon treatment of ARPE19 cells with compound **11** (***Figure 19C***). Treatment of

HEK293T cells with the same compound resulted as mentioned in an increase in metabolic activity. Compound **3** however, exhibited significant differences at lower concentrations already **(*Figure 19A*)**. In ARPE19 cells treated with **3** (0.1 µM), the metabolic rate decreased slightly, since the quotient was below 1 (0.84±0.16, **, $p < 0.01$). The same applied to compound **6** in HEK293T (0.94±0.10, *, $p < 0.05$) as well as ARPE19 cells (0.90±0.08, **, $p < 0.001$) when treated with 0.01 µM as shown in ***Figure 19C***.

An increase in metabolic activity at higher concentrations as seen for compounds **3**, **6** and **11** might indicate changes in metabolism upon TLX modulation. However, it is important to note, that changes of metabolic activity need to be interpreted with caution, as a medium change between the cell viability assay and the nuclei staining occurred. Especially HEK293T cells can detach easily, even when handled with care. As most significant changes occurred either in HEK293T cells or when cells were treated with higher compound concentrations, these differences could be attributed to cell detachment occurring between two read-outs.

8. Discussion

TLX is an important regulator of NSC proliferation and differentiation. Its dysregulation is linked to multiple diseases including neuronal disorders and cancers such as glioblastoma. In cancer, TLX overexpression, in combination with dysregulated expression of cancer associated genes like p21 or TLX target gene PTEN plays an important role [75, 67, 80]. Knock out experiments in mice underline potential clinical benefits of TLX inverse agonists as possible anti-cancer treatment. Additionally, in neuronal and cognitive disorders TLX agonists could help to enhance TLX repressive functions, leading to behavioral regulation and increased cognitive abilities as seen in mice [75, 76, 77].

In the past decade few molecules were proposed to modulate TLX. However, its LBP, potential ligand binding sites, and biological functions remain elusive. Therefore, we employed a set of diverse TLX agonists as well as one TLX inverse agonist to investigate TLX homodimerization as well as molecular and phenotypic consequences upon treatment with TLX agonists in a chemogenomic context.

After successfully expressing and purifying the necessary proteins, biochemical evaluation of TLX-LBD homodimerization revealed that apo TLX-LBD indeed homodimerizes in solution as has recently been described [45]. Preliminary HTRF assay results showed that compound **7** stabilized the TLX-LBD homodimer by a factor 7 compared to the DMSO control, suggesting that the heterocycle moiety at position 3 might play an important role during TLX-LBD homodimerization. However, repetition of the experiment is necessary and further optimization as higher compound concentrations caused quenching of the HTRF signaling impeding with the interpretation of the results. It can be assumed that stabilization of a TLX-LBD homodimer would also affect its biological activity.

Therefore, gene expression analysis of a selection of TLX target genes was performed in T98G glioblastoma cells, ARPE19 retinal cells and HEK293T cells. Previous experiments in T98G glioblastoma cells validated **1** as an TLX agonist able to induce SIRT1 as well as reduce PTEN and TET3 mRNA levels [85]. Here, we observed contradicting effects as TET3 and SIRT1 mRNA levels are slightly increased. Most interestingly compound **8** showed similar dose-dependent effects in T98G and ARPE19 cell lines. When cells are treated with 10 µM, TLX expression itself as well as SIRT1 was upregulated. Unexpectedly, TET3 and PTEN expressions were upregulated instead of downregulated [75, 85]. Even though HEK293T cells exhibited the highest baseline levels of TLX expression, no significant conclusions be drawn.

Due to the discrepancies to previous reported results, we checked for TLX baseline expression levels in the cell lines that were used and started to assess weather cultivating conditions such as cell confluence might impact the gene expression profile in ARPE19 cells. First results indicated that at low to medium confluence ARPE19 cells expressed higher levels of TLX than when cultivated at high density.

Fluctuating conditions could explain variations between experiments. Therefore, we cannot conclude with certainty that the presented effects are due to TLX modulation.

In parallel to quantification of mRNA expression levels of TLX and the selected target genes, phenotypic changes were observed orthogonally in multiple cell lines. First, glioblastoma T98G cells were treated with a subset of compounds which did not affect cellular migration. Only TLX inactive compound **3** (20 µM) was able to reduce the populated area of cells, most likely due to toxicity at the tested concentration. All other tested compounds showed no effects on migration. As the compounds were tested at one only concentration around the EC_{50} for a period of 48 h it is unlikely that we missed the effective dosage, it is however possible. Future experiments could include multiple concentrations as well as additional cell lines. Taken together with the results derived from the quantification of gene expression levels of TLX, PTEN, TET3 and SIRT1 in T98G, different cell lines were chosen for proceeding experiments. TLX expressing cell lines ARPE19, HEK293T and low-expressing A549 cells were seeded in 96-well plates and incubated with compounds **1**-**12** for 48 h. Orthogonally confluence, proliferation and metabolic activity were assessed. This showed that both chemotypes represented in the compound set were tolerated differently. Compounds **4**-**8** were tolerated well up to 10 µM whereas compounds **9** to **12** showed cytotoxic effects at 1 µM or lower. At 1 µM compound **11** however, showed significantly higher confluence in ARPE19 when compared to A549, suggesting a narrow window where effects on TLX might be detectable before concentrations reach toxic levels in both cell lines equally. The opposite effect was shown for compound **6** where confluence was reduced in ARPE19 at higher concentrations compared to A549. However, in a chemogenomic context, all agonists should exhibit the same changes to conclude a TLX-specific effect.

This in accordance with cell viability assessed in a WST-8 assay which supports the previous findings of differences between the two chemotypes. Here, however for compound **11** no differences in proliferation were visible. In addition, compounds **2** and **3** showed significantly reduced viability in ARPE19 cells at lower concentrations. As compound **2** acts as an inverse agonist, one would expect opposite effects in case of TLX modulation. Lastly, the metabolic activity was calculated from the quotient of normalized cell viability and nucleic staining data. Calculated metabolic rates of treated cells derived most likely from the handling of the cells throughout the experiment rather than the compounds themselves, and consequently do not represent the actual metabolic state of the cells. For compounds that exhibited a higher toxicity at lower concentrations already (**9**-**12**), cell detachment was observed in between medium changes and should therefore be considered as false positives regarding their effects on cellular metabolism. However, within the same chemotype compound **11** seemed to be the best tolerated compound within its chemotype regarding cell toxicity at lower concentrations.

All together, these results do not validate TLX-specific effects upon treatment. As the compounds were tested in a chemogenomic context, as a curated set of TLX agonists and one inverse agonist, the detected changes cannot be attributed to TLX-specific modulations as they were only identified for single molecules. No overall phenotypic changes were identified throughout the different cell lines that were tested.

Comparing the different chemotypes, the cytotoxic effects presented here could indicate some off target effects or even different target binding modes and therefore effectiveness. However, differing binding properties can only be evaluated by structural analysis. As a next step, TLX overexpressing cell lines can be generated to achieve higher levels of TLX. Additionally, using TLX knock out cells as a control would allow phenotypic changes to be attributed to TLX modulation. To better understand TLX downstream effects in qPCR experiments it may be beneficial to include additional target genes. Although multiple genes have been identified as TLX targets, but none of them are exclusively regulated by TLX. For instance, PTEN expression is influenced by numerous molecules and pathways, including factor kappa B (NF-κB), a negative regulator, or PPARγ, a positive regulator [105]. Incorporating TLX-specific target genes into the analysis would enhance the robustness of the results. Multiple methods allow the identification of transcription factor binding sites. This includes for example screening a large library of oligonucleotides by Systematic Evolution of Ligands by EXponential enrichment (SELEX) or the separation of TF bound DNA from unbound DNA in an Electro-Mobility Shift Assay (EMSA) followed by sequencing [106]. Furthermore, chromatin immunoprecipitation (ChIP-) combined with high throughput sequencing allows to uncover TF binding sites [107]. Overexpressing TLX cell lines in combination with more specific TLX target genes will provide a more sensitive setting to detect gene expression as well as phenotypic changes upon TLX modulation. The successful expression of TLX-LBD provides a base for further biochemical experiments including structural analysis to uncover ligand-target binding interactions. The identification of compound **7**, being able to shift TLX-LBD homodimer stabilization is promising and as a next step co-regulator recruitment assays can be performed to analyze weather TLX modulation interferes or promotes the binding of selected proteins, including atrophin 1, LSD1 or HDACs [75].

9. Literature

(1) Moore, J. T.; Collins, J. L.; Pearce, K. H. The Nuclear Receptor Superfamily and Drug Discovery. *ChemMedChem* **2006**, *1* (5), 504–523. https://doi.org/10.1002/cmdc.200600006.

(2) Robinson-Rechavi, M.; Carpentier, A.-S.; Duffraisse, M.; Laudet, V. How Many Nuclear Hormone Receptors Are There in the Human Genome? *Trends Genet.* **2001**, *17* (10), 554–556. https://doi.org/10.1016/S0168-9525(01)02417-9.

(3) Baker, M. E. Steroid Receptors and Vertebrate Evolution. *Mol. Cell. Endocrinol.* **2019**, *496*, 110526. https://doi.org/10.1016/j.mce.2019.110526.

(4) Schulman, I. G. Nuclear Receptors as Drug Targets for Metabolic Disease. *Adv. Drug Deliv. Rev.* **2010**, *62* (13), 1307–1315. https://doi.org/10.1016/j.addr.2010.07.002.

(5) Wurtman, R. J. Estrogen Receptor: Ambiguities in the Use of This Term. *Science* **1968**, *159* (3820), 1261. https://doi.org/DOI: 10.1126/science.159.3820.1261.a.

(6) Greene, G. L.; Gilna, P.; Waterfield, M.; Baker, A.; Hort, Y.; Shine, J. Sequence and Expression of Human Estrogen Receptor Complementary DNA. *Science* **1986**, *231* (4742), 1150–1154. https://doi.org/10.1126/science.3753802.

(7) Lehmann, J. M.; Moore, L. B.; Smith-Oliver, T. A.; Wilkison, W. O.; Willson, T. M.; Kliewer, S. A. An Antidiabetic Thiazolidinedione Is a High Affinity Ligand for Peroxisome Proliferator-Activated Receptor γ (PPARγ). *J. Biol. Chem.* **1995**, *270* (22), 12953–12956. https://doi.org/10.1074/jbc.270.22.12953.

(8) Santos, R.; Ursu, O.; Gaulton, A.; Bento, A. P.; Donadi, R. S.; Bologa, C. G.; Karlsson, A.; Al-Lazikani, B.; Hersey, A.; Oprea, T. I.; Overington, J. P. A Comprehensive Map of Molecular Drug Targets. *Nat. Rev. Drug Discov.* **2017**, *16* (1), 19–34. https://doi.org/10.1038/nrd.2016.230.

(9) Iaterion. *Nuclear Receptors*. https://www.iaterion.com/nuclearreceptors#:~:text=and%20xenobiotic%20transformation.-,Approximately%2010–20%25%20of%20current%20FDA%E2%80%90approved%20drugs%20target,30%20billion%20dollars%20per%20year. (accessed 2024-10-01).

(10) Henley, M. J.; Koehler, A. N. Advances in Targeting 'Undruggable' Transcription Factors with Small Molecules. *Nat. Rev. Drug Discov.* **2021**, *20* (9), 669–688. https://doi.org/10.1038/s41573-021-00199-0.

(11) Germain, P.; Staels, B.; Dacquet, C.; Spedding, M.; Laudet, V. Overview of Nomenclature of Nuclear Receptors. *Pharmacol. Rev.* **2006**, *58* (4), 685–704. https://doi.org/10.1124/pr.58.4.2.

(12) Tyagi, S.; Gupta, P.; Saini, A.; Kaushal, C.; Sharma, S. The Peroxisome Proliferator-Activated Receptor: A Family of Nuclear Receptors Role in Various Diseases. *J. Adv. Pharm. Technol. Res.* **2011**, *2* (4), 236. https://doi.org/10.4103/2231-4040.90879.

(13) Weikum, E. R.; Liu, X.; Ortlund, E. A. The Nuclear Receptor Superfamily: A Structural Perspective. *Protein Sci.* **2018**, *27* (11), 1876–1892. https://doi.org/10.1002/pro.3496.

(14) Lee, Y.-K.; Moore, D. D. Dual Mechanisms for Repression of the Monomeric Orphan Receptor Liver Receptor Homologous Protein-1 by the Orphan Small Heterodimer Partner. *J. Biol. Chem.* **2002**, *277* (4), 2463–2467. https://doi.org/10.1074/jbc.M105161200.

(15) Timsit, Y. E.; Negishi, M. CAR and PXR: The Xenobiotic-Sensing Receptors☆. *Steroids* **2007**,

72 (3), 231–246. https://doi.org/10.1016/j.steroids.2006.12.006.

(16) Mukherjee, S.; Mani, S. Orphan Nuclear Receptors as Targets for Drug Development. *Pharm. Res.* **2010**, *27* (8), 1439–1468. https://doi.org/10.1007/s11095-010-0117-7.

(17) De Vera, I. M. S. Advances in Orphan Nuclear Receptor Pharmacology: A New Era in Drug Discovery. *ACS Pharmacol. Transl. Sci.* **2018**, *1* (2), 134–137. https://doi.org/10.1021/acsptsci.8b00029.

(18) Choi, W. J.; Haratipour, Z.; Blind, R. D. Full-Length Nuclear Receptor Allosteric Regulation. *J. Lipid Res.* **2023**, *64* (8), 100406. https://doi.org/10.1016/j.jlr.2023.100406.

(19) Zhang, Y.; Luo, X.; Wu, D.; Xu, Y. ROR Nuclear Receptors: Structures, Related Diseases, and Drug Discovery. *Acta Pharmacol. Sin.* **2015**, *36* (1), 71–87. https://doi.org/10.1038/aps.2014.120.

(20) Solt, L. A.; Burris, T. P. Action of RORs and Their Ligands in (Patho)Physiology. *Trends Endocrinol. Metab.* **2012**, *23* (12), 619–627. https://doi.org/10.1016/j.tem.2012.05.012.

(21) Gronemeyer, H.; Gustafsson, J.-Å.; Laudet, V. Principles for Modulation of the Nuclear Receptor Superfamily. *Nat. Rev. Drug Discov.* **2004**, *3* (11), 950–964. https://doi.org/10.1038/nrd1551.

(22) Aranda, A.; Pascual, A. Nuclear Hormone Receptors and Gene Expression. *Physiol. Rev.* **2001**, *81* (3), 1269–1304. https://doi.org/10.1152/physrev.2001.81.3.1269.

(23) Su, T.; Hollas, M. A. R.; Fellers, R. T.; Kelleher, N. L. Identification of Splice Variants and Isoforms in Transcriptomics and Proteomics. *Annu. Rev. Biomed. Data Sci.* **2023**, *6* (1), 357–376. https://doi.org/10.1146/annurev-biodatasci-020722-044021.

(24) Porter, B. A.; Ortiz, M. A.; Bratslavsky, G.; Kotula, L. Structure and Function of the Nuclear Receptor Superfamily and Current Targeted Therapies of Prostate Cancer. *Cancers* **2019**, *11* (12), 1852. https://doi.org/10.3390/cancers11121852.

(25) Helsen, C.; Claessens, F. Looking at Nuclear Receptors from a New Angle. *Mol. Cell. Endocrinol.* **2014**, *382* (1), 97–106. https://doi.org/10.1016/j.mce.2013.09.009.

(26) Anbalagan, M.; Huderson, B.; Murphy, L.; Rowan, B. G. Post-Translational Modifications of Nuclear Receptors and Human Disease. *Nucl. Recept. Signal.* **2012**, *10* (1), nrs.10001. https://doi.org/10.1621/nrs.10001.

(27) Buzón, V.; Carbó, L. R.; Estruch, S. B.; Fletterick, R. J.; Estébanez-Perpiñá, E. A Conserved Surface on the Ligand Binding Domain of Nuclear Receptors for Allosteric Control. *Mol. Cell. Endocrinol.* **2012**, *348* (2), 394–402. https://doi.org/10.1016/j.mce.2011.08.012.

(28) Khorasanizadeh, S.; Rastinejad, F. Nuclear-Receptor Interactions on DNA-Response Elements. *Trends Biochem. Sci.* **2001**, *26* (6), 384–390. https://doi.org/10.1016/S0968-0004(01)01800-X.

(29) Svetec Miklenić, M.; Svetec, I. K. Palindromes in DNA—A Risk for Genome Stability and Implications in Cancer. *Int. J. Mol. Sci.* **2021**, *22* (6), 2840. https://doi.org/10.3390/ijms22062840.

(30) Germain, P.; Bourguet, W. Dimerization of Nuclear Receptors. In *Methods in Cell Biology*; Elsevier, 2013; Vol. 117, pp 21–41. https://doi.org/10.1016/B978-0-12-408143-7.00002-5.

(31) He, J.; Huang, Z.; Han, L.; Gong, Y.; Xie, C. Mechanisms and Management of 3rd-generation EGFR-TKI Resistance in Advanced Non-small Cell Lung Cancer (Review). *Int. J. Oncol.* **2021**, *59* (5), 90. https://doi.org/10.3892/ijo.2021.5270.

(32) Brzozowski, A. M.; Pike, A. C. W.; Dauter, Z.; Hubbard, R. E.; Bonn, T.; Engström, O.; Öhman,

L.; Greene, G. L.; Gustafsson, J.-Å.; Carlquist, M. Molecular Basis of Agonism and Antagonism in the Oestrogen Receptor. *Nature* **1997**, *389* (6652), 753–758. https://doi.org/10.1038/39645.

(33) McLachlan, J. A. Environmental Signaling: What Embryos and Evolution Teach Us About Endocrine Disrupting Chemicals. **2001**, *22* (3).

(34) Reyes, A. A.; Marcum, R. D.; He, Y. Structure and Function of Chromatin Remodelers. *J. Mol. Biol.* **2021**, *433* (14), 166929. https://doi.org/10.1016/j.jmb.2021.166929.

(35) *Regulation of Transcription and Gene Expression in Eukaryotes*. Scitable by Nature Education. https://www.nature.com/scitable/topicpage/regulation-of-transcription-and-gene-expression-in-1086/#:~:text=In%20eukaryotes%2C%20regulation%20of%20gene,usually%20all%20that%20is%20required). (accessed 2024-09-06).

(36) Oñate, S. A.; Tsai, S. Y.; Tsai, M.-J.; O'Malley, B. W. Sequence and Characterization of a Coactivator for the Steroid Hormone Receptor Superfamily. *Science* **1995**, *270* (5240), 1354–1357. https://doi.org/10.1126/science.270.5240.1354.

(37) Chen, Q.; Guo, P.; Hong, Y.; Mo, P.; Yu, C. The Multifaceted Therapeutic Value of Targeting Steroid Receptor Coactivator-1 in Tumorigenesis. *Cell Biosci.* **2024**, *14* (1), 41. https://doi.org/10.1186/s13578-024-01222-8.

(38) Xu, E. H.; Lambert, M. H. Structural Insights into Regulation of Nuclear Receptors by Ligands. *Nucl. Recept. Signal.* **2003**, *1* (1), nrs.01004. https://doi.org/10.1621/nrs.01004.

(39) Glass, C. K.; Rosenfeld, M. G. The Coregulator Exchange in Transcriptional Functions of Nuclear Receptors. *Genes Dev.* **2000**, *14* (2), 121–141. https://doi.org/10.1101/gad.14.2.121.

(40) Hsia, E. Y.; Goodson, M. L.; Zou, J. X.; Privalsky, M. L.; Chen, H.-W. Nuclear Receptor Coregulators as a New Paradigm for Therapeutic Targeting. *Adv. Drug Deliv. Rev.* **2010**, *62* (13), 1227–1237. https://doi.org/10.1016/j.addr.2010.09.016.

(41) Nagy, L.; Kao, H.-Y.; Love, J. D.; Li, C.; Banayo, E.; Gooch, J. T.; Krishna, V.; Chatterjee, K.; Evans, R. M.; Schwabe, J. W. R. Mechanism of Corepressor Binding and Release from Nuclear Hormone Receptors. *Genes Dev.* **1999**, *13* (24), 3209–3216. https://doi.org/10.1101/gad.13.24.3209.

(42) Benod, C.; Villagomez, R.; Filgueira, C. S.; Hwang, P. K.; Leonard, P. G.; Poncet-Montange, G.; Rajagopalan, S.; Fletterick, R. J.; Gustafsson, J.-Å.; Webb, P. The Human Orphan Nuclear Receptor Tailless (TLX, NR2E1) Is Druggable. *PLoS ONE* **2014**, *9* (6), e99440. https://doi.org/10.1371/journal.pone.0099440.

(43) Yu, R. T.; McKeown, M.; Evans, R. M.; Umesono, K. Relationship between Drosophila Gap Gene Tailless and a Vertebrate Nuclear Receptor Tlx. *Nature* **1994**, *370* (6488), 375–379. https://doi.org/10.1038/370375a0.

(44) Jackson, A.; Panayiotidis, P.; Foroni, L. The Human Homologue of theDrosophila taillessGene (TLX): Characterization and Mapping to a Region of Common Deletion in Human Lymphoid Leukemia on Chromosome 6q21. *Genomics* **1998**, *50* (1), 34–43. https://doi.org/10.1006/geno.1998.5270.

(45) Zhi, X.; Zhou, X. E.; He, Y.; Searose-Xu, K.; Zhang, C.-L.; Tsai, C.-C.; Melcher, K.; Xu, H. E. Structural Basis for Corepressor Assembly by the Orphan Nuclear Receptor TLX. *Genes Dev.* **2015**, *29* (4), 440–450. https://doi.org/10.1101/gad.254904.114.

(46) NIH. *NP_003260.1*. National Centre for Biotechnology and Information. https://www.ncbi.nlm.nih.gov/protein/NP_003260.1.

(47) NIH. *NP_001273031.1*. National Centre for Biotechnology and Information.

https://www.ncbi.nlm.nih.gov/protein/NP_001273031.1/.

(48) Nelson, A. T.; Wang, Y.; Nelson, E. R. TLX, an Orphan Nuclear Receptor With Emerging Roles in Physiology and Disease. *Endocrinology* **2021**, *162* (11), bqab184. https://doi.org/10.1210/endocr/bqab184.

(49) Yu, R. T.; Chiang, M.-Y.; Tanabe, T.; Kobayashi, M.; Yasuda, K.; Evans, R. M.; Umesono, K. The Orphan Nuclear Receptor Tlx Regulates Pax2 and Is Essential for Vision. *Proc. Natl. Acad. Sci.* **2000**, *97* (6), 2621–2625. https://doi.org/10.1073/pnas.050566897.

(50) Monaghan, A. P.; Bock, D.; Gass, P.; Schwger, A.; Wolfer, D. P.; Lipp, H.-P.; Schütz, G. Defective Limbic System in Mice Lacking the Tailless Gene. *Nature* **1997**, *390* (6659), 515–517. https://doi.org/10.1038/37364.

(51) Martínez-Cerdeño, V.; Noctor, S. C. Neural Progenitor Cell Terminology. *Front. Neuroanat.* **2018**, *12*, 104. https://doi.org/10.3389/fnana.2018.00104.

(52) Zhao, X.; Moore, D. L. Neural Stem Cells: Developmental Mechanisms and Disease Modeling. *Cell Tissue Res.* **2018**, *371* (1), 1–6. https://doi.org/10.1007/s00441-017-2738-1.

(53) *Overview of Neural Stem Cells & Lineage-specific Markers*. Overview of Neural Stem Cells & Lineage-specific Markers. https://www.rndsystems.com/pathways/neural-stem-cell-differentiation-pathways-lineage-specific-markers (accessed 2024-09-03).

(54) Qu, Q.; Sun, G.; Li, W.; Yang, S.; Ye, P.; Zhao, C.; Yu, R. T.; Gage, F. H.; Evans, R. M.; Shi, Y. Orphan Nuclear Receptor TLX Activates Wnt/β-Catenin Signalling to Stimulate Neural Stem Cell Proliferation and Self-Renewal. *Nat. Cell Biol.* **2010**, *12* (1), 31–40. https://doi.org/10.1038/ncb2001.

(55) Roy, K.; Thiels, E.; Monaghan, A. Loss of the Tailless Gene Affects Forebrain Development and Emotional Behavior. *Physiol. Behav.* **2002**, *77* (4–5), 595–600. https://doi.org/10.1016/S0031-9384(02)00902-2.

(56) Catani, M.; Dell'Acqua, F.; Thiebaut De Schotten, M. A Revised Limbic System Model for Memory, Emotion and Behaviour. *Neurosci. Biobehav. Rev.* **2013**, *37* (8), 1724–1737. https://doi.org/10.1016/j.neubiorev.2013.07.001.

(57) Zhang, C.-L.; Zou, Y.; Yu, R. T.; Gage, F. H.; Evans, R. M. Nuclear Receptor TLX Prevents Retinal Dystrophy and Recruits the Corepressor Atrophin1. *Genes Dev.* **2006**, *20* (10), 1308–1320. https://doi.org/10.1101/gad.1413606.

(58) Morán, É.; Jiménez, G. The Tailless Nuclear Receptor Acts as a Dedicated Repressor in the Early *Drosophila* Embryo. *Mol. Cell. Biol.* **2006**, *26* (9), 3446–3454. https://doi.org/10.1128/MCB.26.9.3446-3454.2006.

(59) Mangelsdorf, D. J.; Evans, R. M. The RXR Heterodimers and Orphan Receptors. *Cell* **1995**, *83* (6), 841–850. https://doi.org/10.1016/0092-8674(95)90200-7.

(60) Grimley, E.; Dressler, G. R. Are Pax Proteins Potential Therapeutic Targets in Kidney Disease and Cancer? *Kidney Int.* **2018**, *94* (2), 259–267. https://doi.org/10.1016/j.kint.2018.01.025.

(61) Zechner, D.; Fujita, Y.; Hülsken, J.; Müller, T.; Walther, I.; Taketo, M. M.; Bryan Crenshaw, E.; Birchmeier, W.; Birchmeier, C. β-Catenin Signals Regulate Cell Growth and the Balance between Progenitor Cell Expansion and Differentiation in the Nervous System. *Dev. Biol.* **2003**, *258* (2), 406–418. https://doi.org/10.1016/S0012-1606(03)00123-4.

(62) Cui, Q.; Yang, S.; Ye, P.; Tian, E.; Sun, G.; Zhou, J.; Sun, G.; Liu, X.; Chen, C.; Murai, K.; Zhao, C.; Azizian, K. T.; Yang, L.; Warden, C.; Wu, X.; D'Apuzzo, M.; Brown, C.; Badie, B.; Peng, L.; Riggs,

A. D.; Rossi, J. J.; Shi, Y. Downregulation of TLX Induces TET3 Expression and Inhibits Glioblastoma Stem Cell Self-Renewal and Tumorigenesis. *Nat. Commun.* **2016**, *7* (1), 10637. https://doi.org/10.1038/ncomms10637.

(63) Martinez-Gamero, C.; Malla, S.; Aguilo, F. LSD1: Expanding Functions in Stem Cells and Differentiation. *Cells* **2021**, *10* (11), 3252. https://doi.org/10.3390/cells10113252.

(64) Peixoto, P.; Castronovo, V.; Matheus, N.; Polese, C.; Peulen, O.; Gonzalez, A.; Boxus, M.; Verdin, E.; Thiry, M.; Dequiedt, F.; Mottet, D. HDAC5 Is Required for Maintenance of Pericentric Heterochromatin, and Controls Cell-Cycle Progression and Survival of Human Cancer Cells. *Cell Death Differ.* **2012**, *19* (7), 1239–1252. https://doi.org/10.1038/cdd.2012.3.

(65) Sun, G.; Alzayady, K.; Stewart, R.; Ye, P.; Yang, S.; Li, W.; Shi, Y. Histone Demethylase LSD1 Regulates Neural Stem Cell Proliferation. *Mol. Cell. Biol.* **2010**, *30* (8), 1997–2005. https://doi.org/10.1128/MCB.01116-09.

(66) Sun, G.; Yu, R. T.; Evans, R. M.; Shi, Y. Orphan Nuclear Receptor TLX Recruits Histone Deacetylases to Repress Transcription and Regulate Neural Stem Cell Proliferation. *Proc. Natl. Acad. Sci.* **2007**, *104* (39), 15282–15287. https://doi.org/10.1073/pnas.0704089104.

(67) Liu, H.-K.; Wang, Y.; Belz, T.; Bock, D.; Takacs, A.; Radlwimmer, B.; Barbus, S.; Reifenberger, G.; Lichter, P.; Schütz, G. The Nuclear Receptor Tailless Induces Long-Term Neural Stem Cell Expansion and Brain Tumor Initiation. *Genes Dev.* **2010**, *24* (7), 683–695. https://doi.org/10.1101/gad.560310.

(68) Zhang, J.; Grindley, J. C.; Yin, T.; Jayasinghe, S.; He, X. C.; Ross, J. T.; Haug, J. S.; Rupp, D.; Porter-Westpfahl, K. S.; Wiedemann, L. M.; Wu, H.; Li, L. PTEN Maintains Haematopoietic Stem Cells and Acts in Lineage Choice and Leukaemia Prevention. *Nature* **2006**, *441* (7092), 518–522. https://doi.org/10.1038/nature04747.

(69) Iwahara, N.; Hisahara, S.; Hayashi, T.; Horio, Y. Transcriptional Activation of NAD+-Dependent Protein Deacetylase SIRT1 by Nuclear Receptor TLX. *Biochem. Biophys. Res. Commun.* **2009**, *386* (4), 671–675. https://doi.org/10.1016/j.bbrc.2009.06.103.

(70) Chavali, P. L.; Saini, R. K. R.; Matsumoto, Y.; Ågren, H.; Funa, K. Nuclear Orphan Receptor TLX Induces Oct-3/4 for the Survival and Maintenance of Adult Hippocampal Progenitors upon Hypoxia. *J. Biol. Chem.* **2011**, *286* (11), 9393–9404. https://doi.org/10.1074/jbc.M110.167445.

(71) Park, S.-Y.; Kim, J.-S. A Short Guide to Histone Deacetylases Including Recent Progress on Class II Enzymes. *Exp. Mol. Med.* **2020**, *52* (2), 204–212. https://doi.org/10.1038/s12276-020-0382-4.

(72) Nowak, B.; Kozlowska, E.; Pawlik, W.; Fiszer, A. Atrophin-1 Function and Dysfunction in Dentatorubral–Pallidoluysian Atrophy. *Mov. Disord.* **2023**, *38* (4), 526–536. https://doi.org/10.1002/mds.29355.

(73) Murai, K.; Qu, Q.; Sun, G.; Ye, P.; Li, W.; Asuelime, G.; Sun, E.; Tsai, G. E.; Shi, Y. Nuclear Receptor TLX Stimulates Hippocampal Neurogenesis and Enhances Learning and Memory in a Transgenic Mouse Model. *Proc. Natl. Acad. Sci.* **2014**, *111* (25), 9115–9120. https://doi.org/10.1073/pnas.1406779111.

(74) Rolls, E. T. The Cingulate Cortex and Limbic Systems for Emotion, Action, and Memory. *Brain Struct. Funct.* **2019**, *224* (9), 3001–3018. https://doi.org/10.1007/s00429-019-01945-2.

(75) Sobhan, P. K.; Funa, K. TLX—Its Emerging Role for Neurogenesis in Health and Disease. *Mol. Neurobiol.* **2017**, *54* (1), 272–280. https://doi.org/10.1007/s12035-015-9608-1.

(76) Dick, D. M.; Foroud, T.; Flury, L.; Bowman, E. S.; Miller, M. J.; Rau, N. L.; Moe, P. R.; Samavedy, N.; El-Mallakh, R.; Manji, H.; Glitz, D. A.; Meyer, E. T.; Smiley, C.; Hahn, R.; Widmark, C.; McKinney,

R.; Sutton, L.; Ballas, C.; Grice, D.; Berrettini, W.; Byerley, W.; Coryell, W.; DePaulo, R.; MacKinnon, D. F.; Gershon, E. S.; Kelsoe, J. R.; McMahon, F. J.; McInnis, M.; Murphy, D. L.; Reich, T.; Scheftner, W.; Nurnberger, J. I. Genomewide Linkage Analyses of Bipolar Disorder: A New Sample of 250 Pedigrees from the National Institute of Mental Health Genetics Initiative. *Am. J. Hum. Genet.* **2003**, *73* (1), 107–114. https://doi.org/10.1086/376562.

(77) *Bipolar Disorder*. National Institute of Mental Health. https://www.nimh.nih.gov/health/topics/bipolar-disorder#:~:text=Bipolar%20disorder%20(formerly%20called%20manic,three%20types%20of%20bipolar%20disorder.

(78) Park, H.-J.; Kim, J.-K.; Jeon, H.-M.; Oh, S.-Y.; Kim, S.-H.; Park, M.-J.; Soeda, A.; Nam, D.-H.; Kim, H. The Neural Stem Cell Fate Determinant TLX Promotes Tumorigenesis and Genesis of Cells Resembling Glioma Stem Cells. *Mol. Cells* **2010**, *30* (5), 403–408. https://doi.org/10.1007/s10059-010-0122-z.

(79) Jaroudi, W.; Garami, J.; Garrido, S.; Hornberger, M.; Keri, S.; Moustafa, A. A. Factors Underlying Cognitive Decline in Old Age and Alzheimer's Disease: The Role of the Hippocampus. *Rev. Neurosci.* **2017**, *28* (7), 705–714. https://doi.org/10.1515/revneuro-2016-0086.

(80) Zou, Y.; Niu, W.; Qin, S.; Downes, M.; Burns, D. K.; Zhang, C.-L. The Nuclear Receptor TLX Is Required for Gliomagenesis within the Adult Neurogenic Niche. *Mol. Cell. Biol.* **2012**, *32* (23), 4811–4820. https://doi.org/10.1128/MCB.01122-12.

(81) Griffett, K.; Bedia-Diaz, G.; Hegazy, L.; De Vera, I. M. S.; Wanninayake, U. S.; Billon, C.; Koelblen, T.; Wilhelm, M. L.; Burris, T. P. The Orphan Nuclear Receptor TLX Is a Receptor for Synthetic and Natural Retinoids. *Cell Chem. Biol.* **2020**, *27* (10), 1272-1284.e4. https://doi.org/10.1016/j.chembiol.2020.07.013.

(82) *Famprofazone*. DrugBank. https://go.drugbank.com/drugs/DB16702 (accessed 2024-11-17).

(83) *Dydrogesterone*. DrugBank. https://go.drugbank.com/drugs/DB00378 (accessed 2024-11-17).

(84) Kandel, P.; Semerci, F.; Mishra, R.; Choi, W.; Bajic, A.; Baluya, D.; Ma, L.; Chen, K.; Cao, A. C.; Phongmekhin, T.; Matinyan, N.; Jiménez-Panizo, A.; Chamakuri, S.; Raji, I. O.; Chang, L.; Fuentes-Prior, P.; MacKenzie, K. R.; Benn, C. L.; Estébanez-Perpiñá, E.; Venken, K.; Moore, D. D.; Young, D. W.; Maletic-Savatic, M. Oleic Acid Is an Endogenous Ligand of TLX/NR2E1 That Triggers Hippocampal Neurogenesis. *Proc. Natl. Acad. Sci.* **2022**, *119* (13), e2023784119. https://doi.org/10.1073/pnas.2023784119.

(85) Faudone, G.; Bischoff-Kont, I.; Rachor, L.; Willems, S.; Zhubi, R.; Kaiser, A.; Chaikuad, A.; Knapp, S.; Fürst, R.; Heering, J.; Merk, D. Propranolol Activates the Orphan Nuclear Receptor TLX to Counteract Proliferation and Migration of Glioblastoma Cells. *J. Med. Chem.* **2021**, *64* (12), 8727–8738. https://doi.org/10.1021/acs.jmedchem.1c00733.

(86) Heering, J.; Merk, D. Hybrid Reporter Gene Assays: Versatile In Vitro Tools to Characterize Nuclear Receptor Modulators. In *Nuclear Receptors*; Badr, M. Z., Ed.; Methods in Molecular Biology; Springer New York: New York, NY, 2019; Vol. 1966, pp 175–192. https://doi.org/10.1007/978-1-4939-9195-2_14.

(87) Faudone, G.; Zhubi, R.; Celik, F.; Knapp, S.; Chaikuad, A.; Heering, J.; Merk, D. Design of a Potent TLX Agonist by Rational Fragment Fusion. *J. Med. Chem.* **2022**, *65* (3), 2288–2296. https://doi.org/10.1021/acs.jmedchem.1c01757.

(88) Faudone, G.; Kilu, W.; Ni, X.; Chaikuad, A.; Sreeramulu, S.; Heitel, P.; Schwalbe, H.; Knapp, S.; Schubert-Zsilavecz, M.; Heering, J.; Merk, D. The Transcriptional Repressor Orphan Nuclear Receptor TLX Is Responsive to Xanthines. *ACS Pharmacol. Transl. Sci.* **2021**, *4* (6), 1794–1807. https://doi.org/10.1021/acsptsci.1c00195.

(89) Singh, N.; Shreshtha, A. K.; Thakur, M. S.; Patra, S. Xanthine Scaffold: Scope and Potential in Drug Development. *Heliyon* **2018**, *4* (10), e00829. https://doi.org/10.1016/j.heliyon.2018.e00829.

(90) International Human Genome Sequencing Consortium; Whitehead Institute for Biomedical Research, Center for Genome Research:; Lander, E. S.; Linton, L. M.; Birren, B.; Nusbaum, C.; Zody, M. C.; Baldwin, J.; Devon, K.; Dewar, K.; Doyle, M.; FitzHugh, W.; Funke, R.; Gage, D.; Harris, K.; Heaford, A.; Howland, J.; Kann, L.; Lehoczky, J.; LeVine, R.; McEwan, P.; McKernan, K.; Meldrim, J.; Mesirov, J. P.; Miranda, C.; Morris, W.; Naylor, J.; Raymond, C.; Rosetti, M.; Santos, R.; Sheridan, A.; Sougnez, C.; Stange-Thomann, N.; Stojanovic, N.; Subramanian, A.; Wyman, D.; The Sanger Centre:; Rogers, J.; Sulston, J.; Ainscough, R.; Beck, S.; Bentley, D.; Burton, J.; Clee, C.; Carter, N.; Coulson, A.; Deadman, R.; Deloukas, P.; Dunham, A.; Dunham, I.; Durbin, R.; French, L.; Grafham, D.; Gregory, S.; Hubbard, T.; Humphray, S.; Hunt, A.; Jones, M.; Lloyd, C.; McMurray, A.; Matthews, L.; Mercer, S.; Milne, S.; Mullikin, J. C.; Mungall, A.; Plumb, R.; Ross, M.; Shownkeen, R.; Sims, S.; Washington University Genome Sequencing Center; Waterston, R. H.; Wilson, R. K.; Hillier, L. W.; McPherson, J. D.; Marra, M. A.; Mardis, E. R.; Fulton, L. A.; Chinwalla, A. T.; Pepin, K. H.; Gish, W. R.; Chissoe, S. L.; Wendl, M. C.; Delehaunty, K. D.; Miner, T. L.; Delehaunty, A.; Kramer, J. B.; Cook, L. L.; Fulton, R. S.; Johnson, D. L.; Minx, P. J.; Clifton, S. W.; US DOE Joint Genome Institute:; Hawkins, T.; Branscomb, E.; Predki, P.; Richardson, P.; Wenning, S.; Slezak, T.; Doggett, N.; Cheng, J.-F.; Olsen, A.; Lucas, S.; Elkin, C.; Uberbacher, E.; Frazier, M.; Baylor College of Medicine Human Genome Sequencing Center:; Gibbs, R. A.; Muzny, D. M.; Scherer, S. E.; Bouck, J. B.; Sodergren, E. J.; Worley, K. C.; Rives, C. M.; Gorrell, J. H.; Metzker, M. L.; Naylor, S. L.; Kucherlapati, R. S.; Nelson, D. L.; Weinstock, G. M.; RIKEN Genomic Sciences Center:; Sakaki, Y.; Fujiyama, A.; Hattori, M.; Yada, T.; Toyoda, A.; Itoh, T.; Kawagoe, C.; Watanabe, H.; Totoki, Y.; Taylor, T.; Genoscope and CNRS UMR-8030:; Weissenbach, J.; Heilig, R.; Saurin, W.; Artiguenave, F.; Brottier, P.; Bruls, T.; Pelletier, E.; Robert, C.; Wincker, P.; Department of Genome Analysis, Institute of Molecular Biotechnology:; Rosenthal, A.; Platzer, M.; Nyakatura, G.; Taudien, S.; Rump, A.; GTC Sequencing Center:; Smith, D. R.; Doucette-Stamm, L.; Rubenfield, M.; Weinstock, K.; Lee, H. M.; Dubois, J.; Beijing Genomics Institute/Human Genome Center:; Yang, H.; Yu, J.; Wang, J.; Huang, G.; Gu, J.; Multimegabase Sequencing Center, The Institute for Systems Biology:; Hood, L.; Rowen, L.; Madan, A.; Qin, S.; Stanford Genome Technology Center:; Davis, R. W.; Federspiel, N. A.; Abola, A. P.; Proctor, M. J.; University of Oklahoma's Advanced Center for Genome Technology:; Roe, B. A.; Chen, F.; Pan, H.; Max Planck Institute for Molecular Genetics:; Ramser, J.; Lehrach, H.; Reinhardt, R.; Cold Spring Harbor Laboratory, Lita Annenberg Hazen Genome Center:; McCombie, W. R.; De La Bastide, M.; Dedhia, N.; GBF—German Research Centre for Biotechnology:; Blöcker, H.; Hornischer, K.; Nordsiek, G.; *Genome Analysis Group (listed in alphabetical order, also includes individuals listed under other headings):; Agarwala, R.; Aravind, L.; Bailey, J. A.; Bateman, A.; Batzoglou, S.; Birney, E.; Bork, P.; Brown, D. G.; Burge, C. B.; Cerutti, L.; Chen, H.-C.; Church, D.; Clamp, M.; Copley, R. R.; Doerks, T.; Eddy, S. R.; Eichler, E. E.; Furey, T. S.; Galagan, J.; Gilbert, J. G. R.; Harmon, C.; Hayashizaki, Y.; Haussler, D.; Hermjakob, H.; Hokamp, K.; Jang, W.; Johnson, L. S.; Jones, T. A.; Kasif, S.; Kaspryzk, A.; Kennedy, S.; Kent, W. J.; Kitts, P.; Koonin, E. V.; Korf, I.; Kulp, D.; Lancet, D.; Lowe, T. M.; McLysaght, A.; Mikkelsen, T.; Moran, J. V.; Mulder, N.; Pollara, V. J.; Ponting, C. P.; Schuler, G.; Schultz, J.; Slater, G.; Smit, A. F. A.; Stupka, E.; Szustakowki, J.; Thierry-Mieg, D.; Thierry-Mieg, J.; Wagner, L.; Wallis, J.; Wheeler, R.; Williams, A.; Wolf, Y. I.; Wolfe, K. H.; Yang, S.-P.; Yeh, R.-F.; Scientific management: National Human Genome Research Institute, US National Institutes of Health:; Collins, F.; Guyer, M. S.; Peterson, J.; Felsenfeld, A.; Wetterstrand, K. A.; Stanford Human Genome Center:; Myers, R. M.; Schmutz, J.; Dickson, M.; Grimwood, J.; Cox, D. R.; University of Washington Genome Center:; Olson, M. V.; Kaul, R.; Raymond, C.; Department of Molecular Biology, Keio University School of Medicine:; Shimizu, N.; Kawasaki, K.; Minoshima, S.; University of Texas Southwestern Medical Center at Dallas:; Evans, G. A.; Athanasiou, M.; Schultz, R.; Office of Science, US Department of Energy:; Patrinos, A.; The Wellcome Trust:; Morgan, M. J. Initial Sequencing and Analysis of the Human Genome. *Nature* **2001**, *409* (6822), 860–921. https://doi.org/10.1038/35057062.

(91) Piovesan, A.; Antonaros, F.; Vitale, L.; Strippoli, P.; Pelleri, M. C.; Caracausi, M. Human Protein-Coding Genes and Gene Feature Statistics in 2019. *BMC Res. Notes* **2019**, *12* (1), 315. https://doi.org/10.1186/s13104-019-4343-8.

(92) Finan, C.; Gaulton, A.; Kruger, F. A.; Lumbers, R. T.; Shah, T.; Engmann, J.; Galver, L.; Kelley, R.; Karlsson, A.; Santos, R.; Overington, J. P.; Hingorani, A. D.; Casas, J. P. The Druggable Genome and Support for Target Identification and Validation in Drug Development. *Sci. Transl. Med.* **2017**.

(93) Kubinyi, H. Chemogenomics in Drug Discovery. *Ernst Schering Research Foundation*

workshop. 2006, (58), 1-19. https://doi.org/10.1007/978-3-540-37635-4_1

(94) Jones, L. H.; Bunnage, M. E. Applications of Chemogenomic Library Screening in Drug Discovery. *Nat. Rev. Drug Discov.* **2017**, *16* (4), 285–296. https://doi.org/10.1038/nrd.2016.244.

(95) *Chemogenomics: Methods and Protocols*; Merk, D., Chaikuad, A., Eds.; Methods in Molecular Biology; Springer US: New York, NY, 2023; Vol. 2706. https://doi.org/10.1007/978-1-0716-3397-7.

(96) Arrowsmith, C. H.; Audia, J. E.; Austin, C.; Baell, J.; Bennett, J.; Blagg, J.; Bountra, C.; Brennan, P. E.; Brown, P. J.; Bunnage, M. E.; Buser-Doepner, C.; Campbell, R. M.; Carter, A. J.; Cohen, P.; Copeland, R. A.; Cravatt, B.; Dahlin, J. L.; Dhanak, D.; Edwards, A. M.; Frederiksen, M.; Frye, S. V.; Gray, N.; Grimshaw, C. E.; Hepworth, D.; Howe, T.; Huber, K. V. M.; Jin, J.; Knapp, S.; Kotz, J. D.; Kruger, R. G.; Lowe, D.; Mader, M. M.; Marsden, B.; Mueller-Fahrnow, A.; Müller, S.; O'Hagan, R. C.; Overington, J. P.; Owen, D. R.; Rosenberg, S. H.; Ross, R.; Roth, B.; Schapira, M.; Schreiber, S. L.; Shoichet, B.; Sundström, M.; Superti-Furga, G.; Taunton, J.; Toledo-Sherman, L.; Walpole, C.; Walters, M. A.; Willson, T. M.; Workman, P.; Young, R. N.; Zuercher, W. J. The Promise and Peril of Chemical Probes. *Nat. Chem. Biol.* **2015**, *11* (8), 536–541. https://doi.org/10.1038/nchembio.1867.

(97) Kutchukian, P. S.; Chang, C.; Fox, S. J.; Cook, E.; Barnard, R.; Tellers, D.; Wang, H.; Pertusi, D.; Glick, M.; Sheridan, R. P.; Wallace, I. M.; Wassermann, A. M. CHEMGENIE: Integration of Chemogenomics Data for Applications in Chemical Biology. *Drug Discov. Today* **2018**, *23* (1), 151–160. https://doi.org/10.1016/j.drudis.2017.09.004.

(98) Joon, S.; Singla, R. K.; Tjoa, E.; Parmar, K. C.; Shen, B. Alternative Biological Screening Methods. In *Computational Approaches in Drug Discovery, Development and Systems Pharmacology*; Elsevier, 2023; pp 95–137. https://doi.org/10.1016/B978-0-323-99137-7.00011-3.

(99) Hank, E. C.; Sai, M.; Kasch, T.; Meijer, I.; Marschner, J. A.; Merk, D. Development of Tailless Homologue Receptor (TLX) Agonist Chemical Tools. *J. Med. Chem.* **2024**, acs.jmedchem.4c01443. https://doi.org/10.1021/acs.jmedchem.4c01443.

(100) *Propranolol*. DrugBank. https://go.drugbank.com/drugs/DB00571 (accessed 2024-09-08).

(101) Chen, C.; Zhou, M.; Ge, Y.; Wang, X. SIRT1 and Aging Related Signaling Pathways. *Mech. Ageing Dev.* **2020**, *187*, 111215. https://doi.org/10.1016/j.mad.2020.111215.

(102) Zhang, X.; Zhang, Y.; Wang, C.; Wang, X. TET (Ten-Eleven Translocation) Family Proteins: Structure, Biological Functions and Applications. *Signal Transduct. Target. Ther.* **2023**, *8* (1), 297. https://doi.org/10.1038/s41392-023-01537-x.

(103) Ross, S. E.; Bogdanovic, O. TET Enzymes, DNA Demethylation and Pluripotency. *Biochem. Soc. Trans.* **2019**, *47* (3), 875–885. https://doi.org/10.1042/BST20180606.

(104) Chen, C.-Y.; Chen, J.; He, L.; Stiles, B. L. PTEN: Tumor Suppressor and Metabolic Regulator. *Front. Endocrinol.* **2018**, *9*, 338. https://doi.org/10.3389/fendo.2018.00338.

(105) Bermúdez Brito, M. Focus on PTEN Regulation. *Front. Oncol.* **2015**, *5*. https://doi.org/10.3389/fonc.2015.00166.

(106) Jayaram, N.; Usvyat, D.; R. Martin, A. C. Evaluating Tools for Transcription Factor Binding Site Prediction. *BMC Bioinformatics* **2016**, *17* (1), 547. https://doi.org/10.1186/s12859-016-1298-9.

(107) Adli, M.; Bernstein, B. E. Whole-Genome Chromatin Profiling from Limited Numbers of Cells Using Nano-ChIP-Seq. *Nat. Protoc.* **2011**, *6* (10), 1656–1668. https://doi.org/10.1038/nprot.2011.402.

10. Abbreviations

Abbreviation	Definition
AF-1	Activation function-1
AF-2	Activation function-2
ATP	Adenosine triphosphate
ATRAL	All-trans retinalaldehyde
Avi	Avitag
cDNA	Complementary DNA
CNS	Central nervous system
CoA	Co-Activator
CoR	Co-Repressor
CV	Column volume
DBD	DNA binding domain
DMSO	Dimethyl sulfoxide
DNA	Deoxyribonucleic acid
EC_{50}	Half maximal effective concentration
EC_{90}	90% maximal effective concentration
FI	Fluorescence intensity
FRET	Förster resonance energy transfer
GAPDH	Glyceraldehyde-3-phos- phate dehydrogenase
GFP	Green fluorescent protein
HAT	Histone acetyltransferase
HDAC	Histone deacetylases
HDM	Histone demethylases
HMT	Histone methyl transferases
HRE	Hormone response element
HTRF	Homogenous time-resolved fluorescence
HTS	High-throughput screenings
IMAC	Immobilized metal affinity chromatography
IPTG	Isopropyl-b-D-1-thiogalactopyranosid
ITC	Isothermal titration calorimetry
IZ	Intermediate zone
KO	Knock out
LB	Luria broth
LBD	Ligand binding domain
LBP	Ligand binding pocket
LSD-1	Lysin specific demethylase1
MBP	Maltose binding protein
mi-RNA	Micro ribonucleic acid
MoA	Mode of action
mRNA	Messenger ribonucleic acid
NPC	Neural progenitor cells
NR	Nuclear receptor
NSC	Neural stem cells
OD	Optical density
PDB	Protein data bank
pDNA	Plasmid deoxyribonucleic acid
PTEN	Phosphatase and tensin homolog

qPCR	Quantitative polymerase chain reaction
RPC	Retinal progenitor cell
SAR	Structure-activity relationship
SD	Standard deviation
SDS-PAGE	Sodium sulfate - polyacrylamide gel electrophoresis
SEC	Size exclusion chromatography
sGFP	Superfolder green fluorescent protein
SIRT1	Sirtuin 1
SRC-1	Steroid receptor coactivator-1
STV	Streptavidine
SVZ	Subventricular zone
TB	Terrific broth
TCEP	Tris(2-carboxyethyl)phosphine
TET3	Ten eleven translocation 3
TEV	Tabacco etch virus
TF	Transcription factor
TLX	Tailless homologue receptor
VZ	Ventricular zone
ZF	Zink finger

11. List of figures

12. List of tables